MSc Thesis
Department of Geosciences
Utrecht University

28 January 2022

Universiteit Utrecht

Petrological and mineralogical analysis of the metamorphic zones in Cap de Creus, NE Spain

T.P.G. Kok

1st supervisor: Prof. Dr. Martyn Drury
2nd supervisor: Dr. Richard Wessels

Petrological and mineralogical analysis of the metamorphic zones in Cap de Creus, NE Spain

Abstract

The Cap de Creus massif in the northeastern Pyrenees consist of LP–HT greenschist to upper amphibolite facies metasediments and granitoid bodies. The region is subdivided into five metamorphic zones. These zones have been studied extensively but P–T estimates are limited. Earlier studies used general P–T relations to determine pressure and temperature conditions of the metamorphic zones. In this study, P–T conditions were determined based on specific bulk rock compositions from each metamorphic zone in order to give new insights on the relations between the different zones. Optical microscopy, scanning electron microscopy (SEM), energy dispersive X-ray spectroscopy (EDS) and major and trace element analyses were performed to determine mineral assemblages and bulk rock compositions for samples from each of the metamorphic zones. The whole-rock chemistry of the samples was determined by X-ray fluorescence (XRF) and Laser Ablation Inducted Coupled Plasma Mass Spectrometry (LA-ICP-MS). Thermodynamic Perple_X modelling was applied to estimate metamorphic conditions from each zone. This resulted in P–T conditions of 1.0–2.5 kbar and 400–500°C in the lowest grade (chlorite) zone and up to 3.8–4.3 kbar and 650–680°C in the highest grade (sillimanite–K-felspar) zone. In the pelitic rocks of this zone, unstable muscovite reacted with cordierite to form new biotite and prismatic sillimanite, possibly at temperatures close to the solidus. Trace element data indicate that no partial melting took place in the highest-grade samples. Actual contact metamorphism did not take place in the samples, but temperature could have increased locally thanks to the heat of intruding granitoid bodies. Retrograde metamorphism created a new muscovite phase when temperatures dropped below at least 655°C again. As retrograde conditions reached greenschist facies conditions, temperature probably dropped below at least 500°C. Over a distance of 2.75 km, a metamorphic field gradient was determined at 62°C/km.

Acknowledgements

I want to thank my first and second supervisor Martyn Drury and Richard Wessels for allowing me to conduct this research and for their guidance and support throughout the project. I also thank Richard Wessels for performing the SEM analysis.

Furthermore, I thank Cees-Jan de Hoog for performing the XRF analyses and Helen de Waard for the LA-ICP-MS analyses. This research was financially supported by the Olaf Schuilingfonds of Utrecht University Fund.

Table of content

1. Introduction

The Cap de Creus area in Northeast Spain underwent deformation, magmatism and metamorphism and hosts world-class ductile deformation structures. The Cap de Creus peninsula forms the easternmost part of the Pyrenees and the Pyrenean Axial Zone. It consists of Variscan greenschist to upper amphibolite facies metasediments and granitoid bodies (Zwart, 1979). The metamorphic rocks at Cap de Creus expose a series of metamorphic zones and isograds, with a very high metamorphic field gradient. This gradient increases from a chlorite zone in the southwest to a sillimanite zone in the northeast, with a metamorphic field gradient of approximately 80°C/km (Druguet, 2001). The isograds are oriented subparallel to the pegmatite dykes and migmatites that are located in the high-grade metamorphic zones. Low-grade metamorphism (greenschist facies) is found in narrow bands that overprint the high-grade structures. These low-grade metamorphic zones are associated with late folding mylonitisation (Druguet et al., 1997). The metamorphic zones are thought to reflect the effects of low pressure regional metamorphism (Druguet, 2001). However, according to Druguet (2001), heat input from granitoid intrusions caused, or at least enhanced, prograde metamorphism.

Mineral assemblages and textures can provide an indication of the conditions at which a rock was situated. Pressure and temperature estimates can vary with different mineral assemblages, but they are also affected by a variation in mineral composition, such as the amount of iron and magnesium in biotite or cordierite. There are numerous methods that provide information on the pressure or temperature conditions based on the mineral assemblage, but in most cases, it does not provide information on both.

Thermodynamic modelling provides the possibility to visualise the effects of a varying mineral composition of a certain mineral assemblage on the pressure and temperature. Thermodynamic modelling relies on the principle that stable phases are those with the minimum Gibbs free energies. This can visualise how phases or phase assemblages change as a function of temperature, pressure, phase composition or a combination of those (Connolly, 1990, 2005, 2009; Connolly & Petrini, 2002; Holland & Powell, 1998; White et al., 2000). This research will apply a varying Fe^{2+}/Fe^{3+} ratio to thermodynamic modelling to find out how this affects pressure and temperature conditions of mineral assemblages.

The aim of this study is to conduct a petrological, mineralogical and microstructural study to establish the P–T conditions of the metamorphic zones. Optical microscopy, SEM automated mineralogy and major and trace elements analysis were performed on samples from these zones to determine the mineralogy and bulk rock compositions. These results were used as input in Perple_X thermodynamic modelling to establish the P–T conditions. By varying the Fe^{2+}/Fe^{3+} ratio, the effects of oxidising or reducing conditions on the mineral assemblages was further investigated. In addition, quartz microstructures were investigated to determine the temperatures from the recrystallization regimes (Stipp et al., 2002). The acquired data was used to discuss whether the P–T conditions of the different metamorphic zones are controlled by regional metamorphism, or if the highest-grade zones are related to zones of magmatic intrusion. Thermodynamic modelling resulted in P–T conditions of 3.8–4.3 kbar and 650–680°C in the highest-grade zone and a metamorphic field gradient of approximately 62°C/km. Trace element data showed that partial melting did not take place in the highest-grade zones.

2. Geological setting

2.1 Pyrenees

The Pyrenees are a mountain belt in Southwest Europe located at the border between France and Spain. This east-west trending mountain belt is of approximately 1000 km in length and 100 km in width. It divides the Aquitaine Basin in the north from the Ebro Basin in the south (Choukroune et al., 1990).

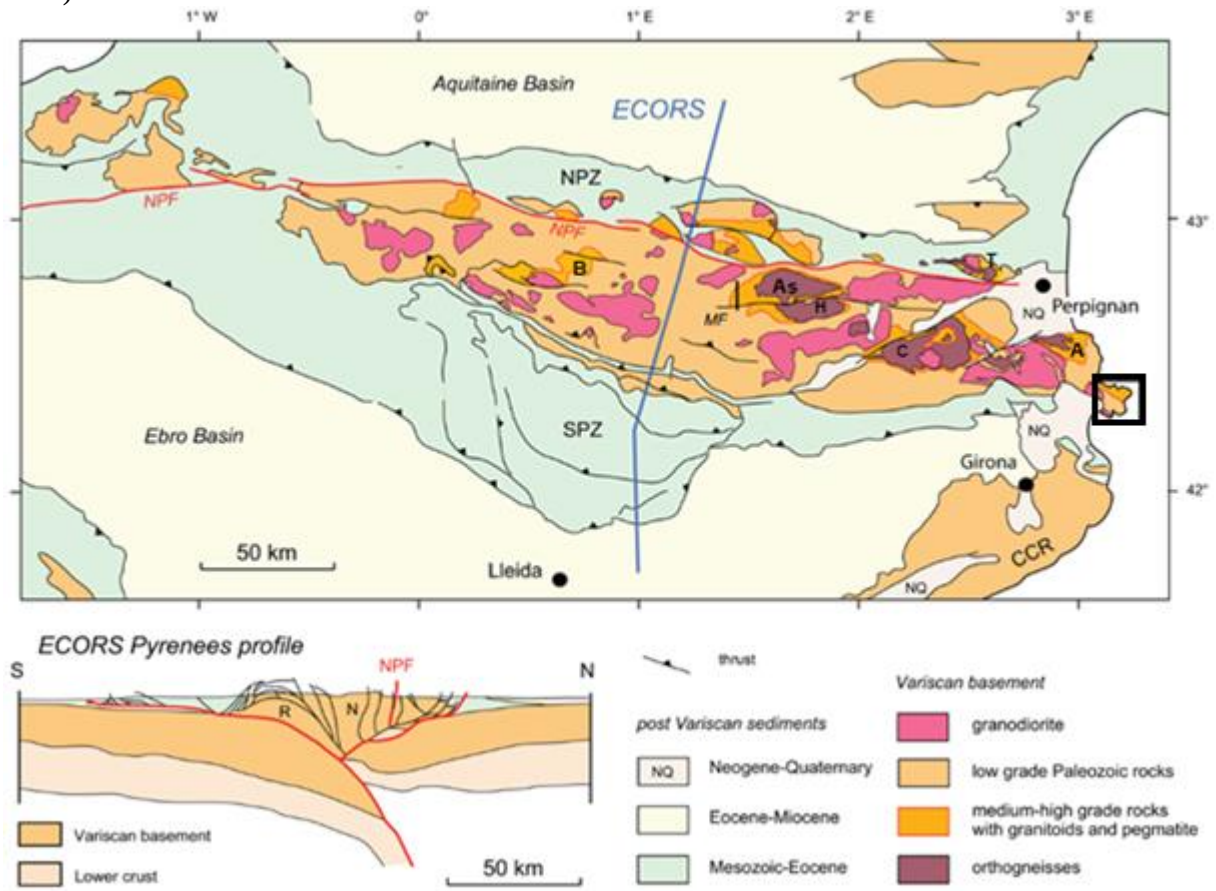

Figure 1: Geological sketch map of the Pyrenees compiled after Zwart (1979) and Vergés et al. (1995), obtained from Vissers et al. (2017). ECORS crustal-scale cross-section after Muñoz (1992). Black rectangle indicates Cap de Creus area location (see Fig. 3–5). A = Albera massif; As = Aston massif; B = Bossòst massif; C = Canigou massif; CCR = Catalan Coastal Range; H = Hospitalet massif; MF = Mérens Fault; NPF = North Pyrenean Fault; NPZ = North Pyrenean Zone; SPZ = South Pyrenean Zone; T = Trois-Seigneurs massif. ECORS Pyrenees profile: N = Nogueras unit; R = Rialp unit.

The Pyrenees were formed by the continental collision between Iberia and Europe in which the Iberian lithosphere partially subducted to the north from the early Eocene till the late Oligocene (Vergés et al., 2002). They were formed in at least two orogenic periods: the Variscan and the Alpine orogeny. Three main zones can be distinguished from north to south: The North Pyrenean zone, the Axial zone and the Nogueras zone (Fig. 1). The Axial zone, the main body of the Pyrenees, consists of Palaeozoic sediments and crystalline rocks of metamorphic and magmatic origin. They were folded and metamorphosed, or intruded during the Variscan orogeny in the Carboniferous (Zwart, 1979). The North Pyrenean Zone consists of crystalline rocks covered by Palaeozoic sediments, while the Nogueras zone only contains Palaeozoic sediments. During the Alpine orogeny in late Cretaceous and Palaeogene times, a convergent motion between Iberia an Europe resulted in 150 km of crustal shortening in the Pyrenees (Beaumont et al., 2000). During this event, ductile and brittle thrusts emplaced the Variscan rocks of the Axial Zone and North Pyrenean Zone in a wedge-shaped orogenic belt (Muñoz, 1992; Roure

et al., 1989). The North Pyrenean Zone and the Nogueras zone were also deformed during the Alpine orogeny. This created the North Pyrenean fault that separates the North Pyrenean Zone from the Axial zone. This fault is a sinistral transtensional fault and is considered to be the boundary between Iberia and Europe (Choukroune & Mattauer, 1978; Le Pichon & Sibuet, 1971).

Two major tectono-metamorphic domains can be distinguished in the Palaeozoic rocks. In the external zone (also referred to as suprastructure) low-grade metamorphism took place and steep folds and cleavages occur as Variscan structures. The internal zone (also referred to as infrastructure) was metamorphosed at a high-grade and contains gentle-dipping foliations (Zwart, 1979, 1986).

2.2 NE Pyrenees

Variscan rocks are exposed in several massifs along the Axial Zone in the northeast of Iberia, mostly south of the North Pyrenean Fault, and show a NW–SE trending zonation. In the southwest this zonation occurs as external shallow-seated rocks of low to very low-grade metasediments (Iberian Chain, Catalonian Coastal Ranges, Western and Central Pyrenees), whereas towards the northeast more internal deep-seated rocks of medium to high-grade metasediments and orthogneisses are present (eastern Axial zone and the North Pyrenean Massifs) (Carreras & Capella, 1994; Druguet, 2001).

Several massifs in this internal zone, such as the Trois-Seigneurs, Albera, Bossòst, Aston and Cap de Creus (Fig. 1), show a distribution of low pressure prograde metamorphic zones (Barnolas et al., 1996; Guitard et al., 1995). These contain large areas of low-grade metasediments bordering metamorphic or migmatitic cores of amphibolite to granulite facies (Fig. 2). In these zones pressures have been recorded up to almost 8 kbar (Vielzeuf et al., 1990). Most massifs show the following metamorphic zones at increasing metamorphic grades: chlorite–muscovite, biotite, andalusite, sillimanite and migmatite (Druguet, 2001; Guitard et al., 1995). Average metamorphic field gradients of these massifs vary between 65°C/km (Guitard et al., 1995), 70°C/km (Zwart, 1986) and approximately 75°C/km (Barnolas et al., 1996). The metamorphic gradient of the Cap de Creus area is considered to be up to 80°C/km over a horizontal distance of approximately 5 km. (Druguet, 2001).

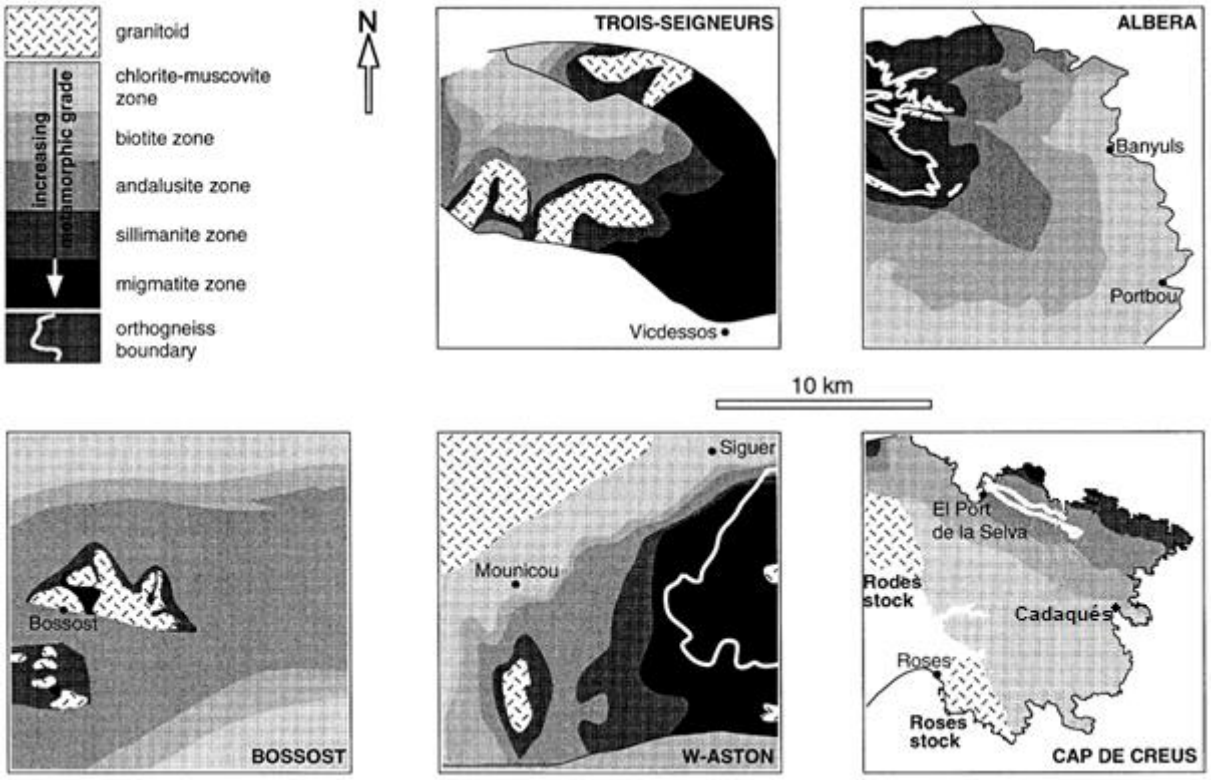

Figure 2: Metamorphic gradients in other Variscan massifs in the northeastern Pyrenees (see Fig. 1 for locations) based on original drafts in Barnolas et al. (1996), obtained from Druguet (2001)

2.3 Metamorphism in Cap de Creus

The Cap de Creus massif is the easternmost part of the Spanish Pyrenees. Variscan metamorphism affected all pre-Variscan lithologies in the area, which mainly consist of metapsammites (metagreywackes), metapelites and some quartzite beds. As in most other massifs in the internal zone, several different metamorphic zones can be found in Cap de Creus (Fig. 3, 5). In Cap de Creus, five distinct metamorphic zones and one metamorphic subzone have a metamorphic gradient increasing from the southwest to the northeast (Druguet, 2001) Table 1 shows an literature overview of each metamorphic zone with its respective mineral assemblage and estimated P–T conditions.

The chlorite zone, also referred to as the chlorite–muscovite zone (Druguet, 1997; Guitard et al., 1995), is the southwesternmost outcropping zone which covers a large area with phyllites and fine grained metagreywackes. It contains a mineral assemblage of chlorite, muscovite, quartz and plagioclase with a low or very low metamorphic grade (Druguet, 2001; Guitard et al., 1995).

The biotite zone has a width of 1.5–2 km and phyllites gradually become micaschists in which biotite is macroscopically visible (Druguet, 2001). Biotite, muscovite, chlorite, quartz and plagioclase occur in this zone. Guitard et al. (1995) measured very albite-rich plagioclase and states that both primary and secondary (retrograde) chlorite coexist, but they are difficult to distinguish in optical microscopy. Druguet (1997) yielded a temperature of 450°C for the biotite zone using a computer software developed by Reche & Martínez (1996).

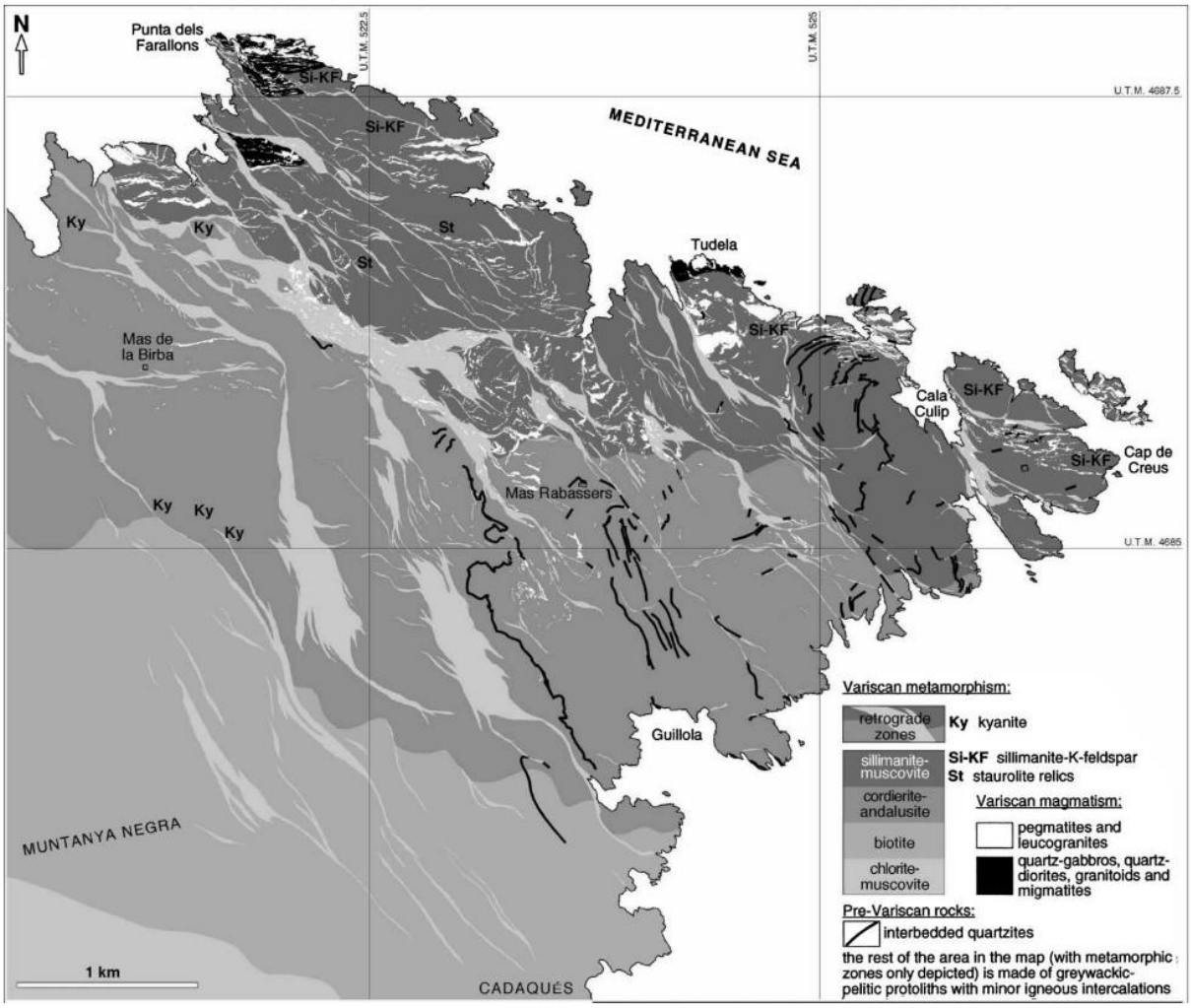

Figure 3: Location of the metamorphic zones and migmatites in the Cap de Creus peninsula. Locations of sillimanite–K-feldspar patches marked by "Si-KF", obtained from Druguet (2001)

The andalusite–cordierite zone extends over 1.5–2 km as well and can be recognised by an increase in grain size and the presence of cordierite and andalusite porphyroblasts. Beside these minerals, biotite, muscovite, quartz and plagioclase complete the mineral assemblage. Estimated P–T conditions from a petrogenetic grid for the northern part of this zone yielded 4.3–4.6 kbar and 600°C (Druguet, 1997, 2001).

Grain size keeps on increasing gradually into the sillimanite–muscovite zone, in which sillimanite mainly starts growing epitaxially as fibrolite on biotite. Andalusite coexist with sillimanite in the southern part of the zone together with cordierite. Quartz, plagioclase and muscovite complete the assemblage. Druguet (2001) used thermobarometric calculations developed by Reche & Martínez (1996) to estimate that P–T conditions in the sillimanite zone–muscovite zone range from 2.4 kbar and 560°C based on garnet rims to 4.7 kbar and 670°C based on garnet cores with retrograde zoning in the sillimanite zone (Druguet, 2001).

The sillimanite–K-feldspar subzone is characterised by the assemblage of sillimanite (as fibrolite), quartz and K-feldspar. This subzone rather occurs in the far east of the area as patches within the sillimanite–muscovite zone or at the margins of migmatitic complexes. It is difficult to construct a sillimanite–K-felspar isograd due to the common occurrence of retrograde muscovite (Druguet, 1997).

Table 1: Overview of mineral assemblages per metamorphic zone based on Druguet (2001) and Guitard et al. (1995)

Metamorphic zone	Literature mineral assemblage	P (kbar)	T (°C)
chlorite	Qz Pl Ms Chl		
biotite	Qz Bt Pl Ms Chl		450
andalusite–cordierite	Qz Bt Pl Ms And Crd	4.3	600
sillimanite–muscovite	Qz Bt Pl Ms (And)[1] Sil Crd	2.4–4.7	560–670

[1] Andalusite restricted to southern part of the zone

Garnets are found in most zones, but these are restricted to psammitic layers. Staurolite is only found as a relic in andalusite or cordierite in the andalusite–cordierite and the sillimanite–muscovite zones. The biotite found in the different zones gradually changes composition having a Fe/Fe+Mg ratio of 0.55 in the biotite zone that decreases slightly with increasing metamorphic grade (Druguet, 1997).

Retrograde metamorphism and mylonitisation took place under greenschist facies conditions and are observed throughout the area. Secondary muscovite and chloritization of biotite are commonly found in the sillimanite–muscovite zone and the sillimanite–K-feldspar subzone. Muscovite has grown as coarse, randomly oriented crystals and appear to be kinked by late deformations (Druguet, 1997). Retrograde metamorphism and mylonitisation appear to be related to the development of late structures such as folds and shear zones. However, retrograde metamorphism can also be seen in cordierite porphyroblasts altered into pinite (Druguet, 1997). In the westernmost domains that are affected by late folding, kyanite is sporadically found as pseudomorphs of sillimanite or andalusite (Druguet, 2001).

The prograde metamorphic assemblages are considered to have undergone low pressure regional metamorphism. However, Druguet (2001) states that medium pressures may have been reached because: (i) relics of staurolite inside andalusite or cordierite are sporadically present; and (ii) kyanite pseudomorphs of andalusite partially replaced by muscovite produced during a late metamorphic stage locally exist along pinched synforms. It is relatively common for staurolite relics to be found in many Variscan massifs of the Pyrenees, for example in the Bossòst massif (Mezger et al., 2004). They are considered to be related to a medium pressure metamorphic stage with an early compressional event (Barnolas et al., 1996; Guitard et al., 1995).

2.4 Magmatism in Cap de Creus

The fifth and last metamorphic zone located in the northernmost part of the Cap de Creus peninsula, is the migmatite zone. Three main migmatitic complexes are present: Cap Gros, Tudela (Druguet, 1997) and Punta dels Farallons. The latter complex consists of partially migmatised sillimanite schists and

several types of less differentiated igneous rocks such as quartz-gabbros, quartz-diorites and heterogenous granitoid bodies surrounded by migmatite pods (Druguet et al., 1995; Druguet & Hutton, 1998). According to Druguet (1997), based on major element data and the calcic composition of plagioclase, these less differentiated rocks originate from the mantle. The ascent of the granitoid bodies caused local partial melting, which is considered to be the reason why the migmatites are restricted to a couple of small areas along the northern coastline of the peninsula (Druguet, 2001). Peraluminous rocks such as leucogranites and pegmatites are also found in the migmatitic complexes. The pegmatites form an irregular dyke swarm of 2.4 km in width, stretching from the andalusite–cordierite zone through the sillimanite zones up to the migmatitic complexes. Together with the leucogranites they could derive from partial melting of pelitic metasediments. In the Tudela migmatitic complex, zircon dating from a deformed syn-tectonic quartz diorite yielded a mean age 298.8 ± 3.8 Ma (Druguet et al., 2014).

A second group of Variscan igneous rock is present in the south of the peninsula. Variscan magmatism emplaces granodiorite stocks in the low-grade metasediments. These are the Roses and Rodes granodiorites, located in the south and west of the chlorite zone respectively. Their composition varies between granodiorite and tonalite and the intrusions are sheet shaped. A narrow aureole of contact metamorphism in the low grade metasediments was formed by the emplacement of the granodiorites, which corresponds to shallow intrusions (Carreras & Losantos, 1982). A mean age of 290.8 ± 2.9 Ma was yielded from a granodiorite from the Roses pluton (Druguet et al., 2014).

2.5 Tectonic evolution of Cap de Creus

The Cap de Creus peninsula was affected by polyphase deformation with three main phases of deformation. D_1 and D_2 took place during prograde low pressure Hercynian (Variscan) regional metamorphism, before metamorphic peak conditions, while D_3 is known for retrograde shearing events succeeding peak metamorphism (Carreras, 2001; Druguet, 2001; Druguet et al., 1997).

The first phase of deformation (D_1) created a continuous schistosity (S_1) in the metasediments under prograde metamorphic conditions prior to the metamorphic peak. This schistosity is subparallel to the orientation of the sedimentary bedding (S_0) and therefore it is referred to as $S_{0/1}$. It is well defined in the metasediments due to the alignment of phyllosilicates. Several quartz veins varying in width from 1 mm to 50 cm originating from or prior to D_1 were deformed and developed boudins and a marked stretching lineation (Druguet et al., 1997). Recumbent folds and thrusts with a gently dipping foliation were produced during D_1. Intersection lineations have a N–S trend. This event is associated with crustal thickening, which occurred during the first metamorphic stage (Druguet, 2001).

The second deformation phase (D_2) is considered to be intense and inhomogeneous during which the bedding, S_1 and quartz veins were folded, resulting in steeply inclined or upright axial surfaces. In less deformed areas the axial surfaces are approximately NE–SW orientated, while an E–W trend was observed in more deformed areas. Crenulations in the metapelites in the low-grade zones are defined by biotite growth in a preferred orientation, while biotite and sillimanite growth took place in the high-grade zones. The presence of syn-kinematic sillimanite and 1 to 10 cm long partial melt veins indicate that D_2 took place at peak metamorphic conditions (Druguet et al., 1997). Pegmatite dykes intruded during D_2 after metamorphic peak conditions were reached. Their crystallisation temperatures are estimated to be over 580°C (Alfonso, 1996) and at about 600°C (Damm et al., 1992). Due to the heterogeneous distributions of the D_2 deformation, a low and high strain domain can be distinguished (Fig. 4a). A high strain domain in the north is dominated by S_2 foliation (Fig. 4b) and E–W trending folds and crenulation cleavages were formed in during D_2. In the southern low strain domain, S_1 foliation is dominant (Fig. 4b). E–W trending folds in this domain were developed during D_2, but also at retrograde conditions, meaning that E–W trending folds in this domain may be associated with either D_2 or with early stages of D_3 (Druguet, 2001). It is thought that calc-alkaline magmatic activity, and therefore the formation of the Variscan igneous rocks, was coeval and coupled with D_2 dextral transpression which involved NNW–SSE crustal shortening during Late Carboniferous and Early Permian time (~299–291 Ma). This is based on field structural relationships which indicate that migmatisation took place synchronously with the emplacement of quartz dioritic magmas at approximately 299 Ma (Druguet et al., 2014).

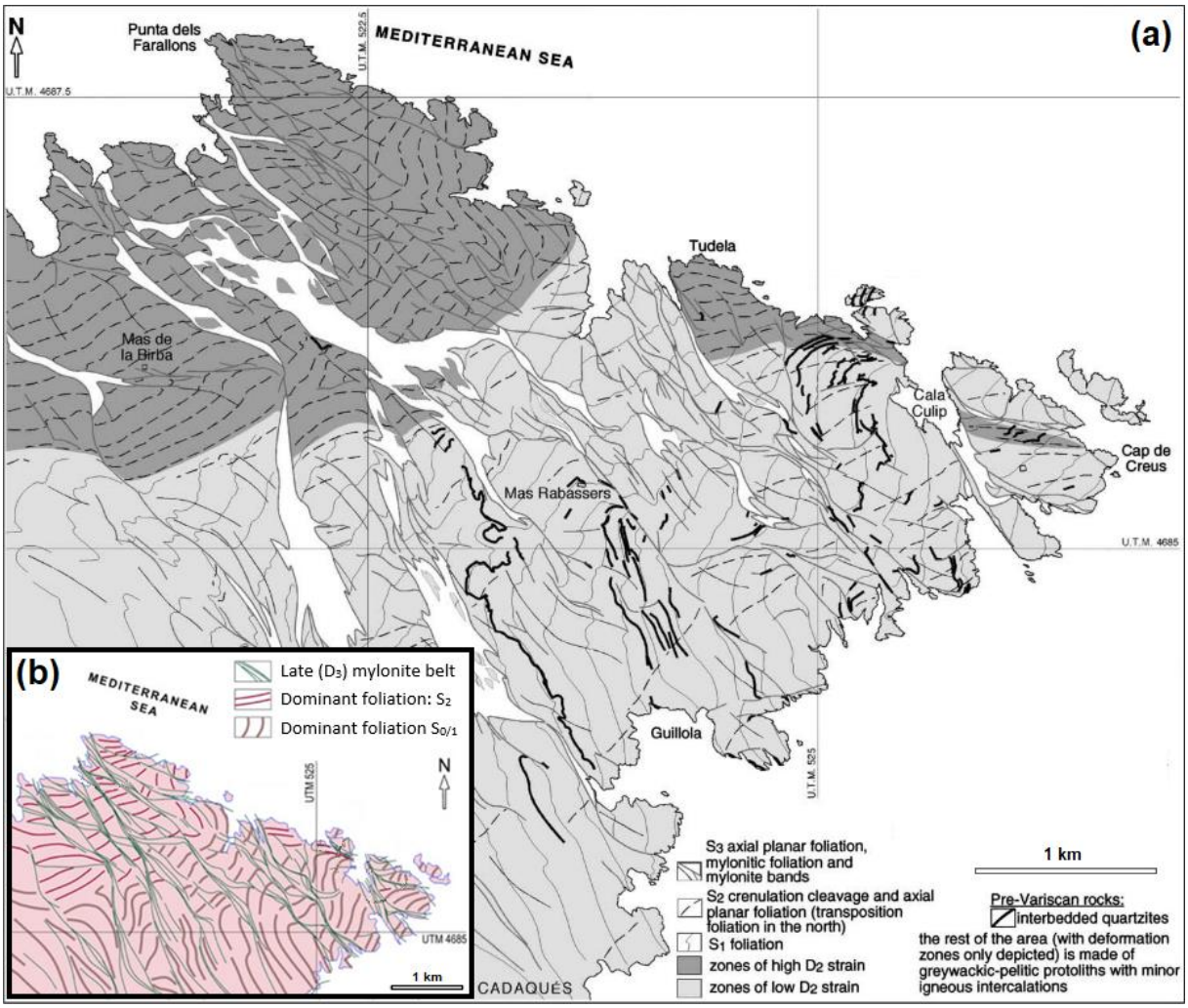

Figure 4: (a) Structural map of the Cap de Creus peninsula showing the distribution of the high- and low-strain domains from Druguet (2001). (b) Simplified map of the Cap de Creus peninsula indicating the dominant foliation directions from Carreras et al (2013).

The third and last main deformation event (D_3) developed anastomosed ductile shear zones trending E–W to NW–SE under retrograde metamorphic conditions (Carreras & Casas, 1987). These shear zones cut through medium to high grade schists and pegmatites and show a predominant dextral strike-slip or oblique-slip movement. D_1 and D_2 structures were heterogeneously sheared and folded, creating D_3 folds orientating NW–SE. With increasing strain, these folds progressively rotate clockwise to a more NNW-SSE orientation (Druguet, 2001). These shear zones mainly formed in the andalusite and sillimanite zones. Muscovite from the shear zones was dated by Vissers et al. (2017) and yielded Middle Jurassic ages between 175.18 ± 1.10 Ma and 159.33 ± 0.43 Ma. One Tertiary age of 58.07 ± 0.55 was yielded as well (Vissers et al., 2017). These proposed ages led to a debate regarding the Variscan versus Alpine timing of shear zone development (Druguet et al., 2018; Vissers et al., 2018).

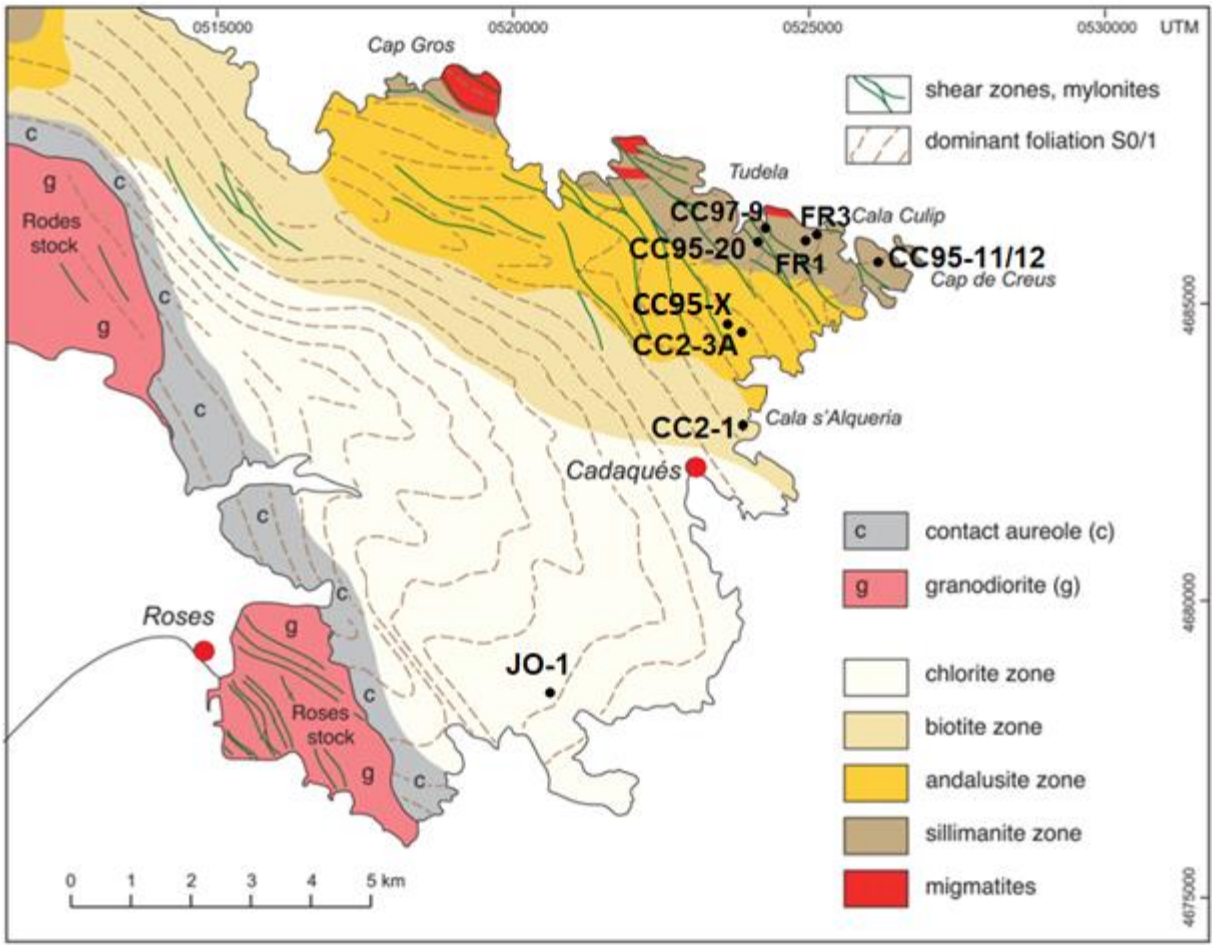

Figure 5: Sample locations illustrated with their corresponding metamorphic zone. Note that sample CC95-11 and CC95-12 originate from the sillimanite–K-feldspar subzone, whereas the other samples from the sillimanite zone originate from the sillimanite–muscovite zone (for comparison see Fig. 3). Map obtained from Vissers et al. (2017)

3. Methods

Due to the fact that this project was conducted during the COVID-19 pandemic, no initial fieldwork campaign took place for this specific study and access to university and laboratories was limited. However, thanks to several previous fieldwork campaigns to the study area, many rock samples were collected from the study area over the years. Therefore, a large collection of samples with enough variety with respect to the different metamorphic zones of the area was available for this project. Ten samples were studied in total, of which eight are schists and two are quartzites. At least one schist sample is present per metamorphic zone, except for the migmatite zone, to ensure that all metamorphic domains are covered in this study (Table 4). The locations of the samples can be found in Fig. 5. For some of the rock samples, one or more thin sections were already available. For the other samples, thin sections were cut following the method of Tikoff et al. (2019), in which the orientation of the thin sections is determined with respect to a kinematic and geographic reference frame. All samples underwent numerous methods to collect the necessary data (Table 2).

Table 2: Overview of methods performed on each sample

Sample	OM	SEM(-EDS)	XRF	LA-ICP-MS	Perple_X
CC95-11	X	X	X	X	X
CC95-12	X	X	X	X	X
CC97-9	X	X	X	X	X
CC95-20	X		X	X	X
CC95-X	X		X	X	X
CC2-3A	X		X	X	X
CC2-1	X		X	X	X
JO-1	X		X	X	X
FR1	X				
FR3	X				

3.1 Optical microscopy

The obtained thin sections were scanned and digitised with a Zeiss Axio Scan.Z1 thin section scanner. Scanning at a 10x magnification and in brightfield transmitted light, resulted in high-resolution (0.44 µm/pixel) scans. These scans contain one channel of plane polarised light (PPL) and six channels of cross polarised light (XPL), in which each channel was rotated 15° with respect to the previous channel. Subsequently, the thin sections were interpreted and annotated using the ZEN 3.2 (blue edition) virtual microscopy software from Carl Zeiss Microscopy GmbH. Minerals are annotated following the suggested mineral abbreviations from Whitney & Evans (2010).

Due to the limited access to actual microscopes under COVID-19 related restrictions, virtual microscopy was the main method to study the thin sections. Unfortunately, this method does not allow for the observation of pleochroism, while it is also difficult to observe certain features such as the difference between positive and negative relief. Therefore, if necessary and if possible, a Zeiss Axio transmitted light microscope was used as well.

3.2 Scanned electron microscopy

Two thin sections from the higher-grade metamorphic zones were analysed using scanning electron microscopy (SEM). The thin sections were polished, carbon coated and analysed using a Zeiss EVO-15 scanning electron microscope with two Bruker XFlash 6 | 60 EDS detectors and one backscattered electron (BSE) detector. The accelerating voltage was set on 15 kV, so that the X-ray excitation for all elements of interest was ensured. The probe current was set on 1 nA for all samples. The Bruker Esprit

2.1 software was used for energy dispersive X-ray spectroscopy (EDS) spot measurements on numerous grains throughout the samples. With this data, the chemical composition of those grains was determined which was necessary for the automated mineralogy (AM). The output data of the EDS detectors was saved in separate Microsoft Excel files per detector per measurement.

SEM-AM runs were conducted with an acceleration voltage of 15 kV, a beam current of 1 nA, a dwell time of 0.02 s, an aperture of 30 µm and a step size of 20 µm. With the Zeiss Mineralogic software suite, a region of interested was selected and mapped for each thin section. This resulted in a false colour phase map based on the EDS measurements and a map of stitched BSE images.

The Zeiss Mineralogic software produces a table for each analysis that stated the area percentage, weigh percentage and average chemical composition in normalised atomic mass for each phase. A Python script written by Van Melick (2021) was used to convert mineral compositions to oxide weight percentages (assuming stoichiometry) in order to calculate the bulk rock composition. The obtained bulk rock compositions could then be used in thermodynamic modelling.

3.3 X-ray fluorescence

X-ray fluorescence (XRF) analysis was performed on all schist samples in order to obtain a bulk rock composition. For the samples that already obtained a bulk rock composition, the XRF data was used as a second and independent source. In order to make the most optimal comparison, the analysed material was cut from the same plane as the thin sections. The material was powdered and dissolved in a heated borate flux before being cooled into glass beads, so that homogeneity was achieved. The analysis was conducted on a Thermo Scientific ARL Perform'X 4200W WDXRF analyser.

3.4 LA-ICP-MS

Laser Ablation Inducted Coupled Plasma Mass Spectrometry (LA-ICP-MS) was performed to obtain trace element data of the metapelites in order to study potential fluid-rock or melt-rock interactions. After performing XRF analysis, the same samples were immediately analysis by laser ablation in order to obtain the most reliable data. All samples were analysed three times so that possible strong anomalies could be detected. LA-ICP-MS was configurated according to Table 3.

The data obtained was calibrated with the standard BCR-2G, a basaltic glass standard, and was processed by using the GLITTER software (Griffin et al., 2008).

Rare earth element (REE) diagrams were constructed using the REE trace element data to identify whether or not partial melting occurred in the samples. These diagrams were constructed for the high-grade samples. The lowest-grade sample from the chlorite zone was also plotted in the diagram and used as a reference sample, as it is unlikely that melting took place in that sample.

Table 3: Overview of the LA-ICP-MS configuration

Laser type	Compex 102 excimer
GAMMA	193 nm
Energy	22-30 kV
Energy density on sample	± 12 J/cm²
Beam profile	Homogenised
Repetition rate	10 Hz
Spot size	120 µm
ICPMS type	Thermo Fisher Scientific Element2
Power	1250 W
Plasma gas	Ar - Flow rate: 0.851/min
Carrier gas	Ar/He - Flow rate: Ar: 0.71/min, He: 0.71/min
Cooling gas	Ar - Flow rate: 161/min

3.5 Thermodynamic modelling

P–T diagrams pseudosections for the mineral assemblage for every thin section were modelled with the Perple_X software (Connolly, 1990, 2005, 2009; Connolly & Petrini, 2002) version 6.9.0 using the thermodynamic data file (hp62ver.dat) from Holland & Powell (2011). Solution models from White et al. (2014 a) were used for chlorite, chloritoid, garnet, staurolite cordierite and white mica. The feldspar solution model comes from Fuhrman & Lindsley (1988). The solidus was determined in every calculation using the melt solution model from Holland & Powell (2001) and White et al. (2001). All solution models were calibrated with the thermodynamic dataset.

Thermodynamic modelling was conducted using the following chemical system: MnO–Na_2O–CaO–K_2O–FeO–MgO–Al_2O_3–SiO_2–H_2O–TiO_2–Fe_2O_3 (MnNCKFMASHTO). In general, a limited number of components gives a clearer view on the reactions taking place between different stability fields. However, omitting certain components may result in an incomplete representation of reality or in the absence of certain important phases. For instance, the presence or absence of garnet in the system is of great importance when determining P–T conditions through modelling. Research has shown that the presence of MnO strongly influences the presence of garnet, based on the observed strong partitioning of MnO in garnet in comparison with other minerals (Symmes & Ferry, 1992; White et al., 2014 b) If MnO were to be omitted, the stability field of garnet would not be properly represented in the diagrams. Therefore, garnet is included in the models. TiO_2 and Fe_2O_3 were added to include certain oxide phases and because small to moderate amounts of these components have little effect on silicate mineral equilibria. Moreover, rocks rich in Fe_2O_3 undergo a different metamorphic succession from ferrous oxide-rich compositions (White et al., 2000). All calculations were performed with H_2O being a saturated fluid. Therefore, the fluid equation X(CO2) H2O-CO2 CORK from Holland & Powell (1991, 1998) was used.

For the three highest grade samples, the SEM-AM bulk rock composition was used as primary input. The XRF data for these samples was only used if there was a significant difference in the SEM-AM bulk rock composition compared with its respective XRF bulk rock composition or compared to the other samples. For the other samples, the XRF data was used as input, as that is the only bulk rock data available for those samples.

All obtained pseudosections were edited and annotated using Inkscape. Mineral assemblages were annotated following the suggested mineral abbreviations from Whitney & Evans (2010).

A research about ferrous/ferric (Fe^{2+}/Fe^{3+}) partitioning on a large dataset of silicates in metapelites conducted by Forshaw & Pattison (2021) showed that on average metapelites contain approximately 75% ferrous (Fe^{2+}) iron. The high-grade metapelitic samples were modelled with a varying (Fe^{2+}/Fe^{3+}) ratio to determine whether the ratio of Forshaw & Pattison (2021) can be applied to the Cap de Creus metapelites as well. If necessary, the ratio was adjusted.

4. Results

4.1 Optical microscopy

Table 4: Overview of metapelitic samples, their metamorphic zone and their mineral assemblage

Sample	Metamorphic zone	Observed mineral paragenesis
CC95-11	sillimanite–K-feldspar	Qz Bt Pl Ms Sil Kfs Ilm Rt
CC95-12	sillimanite–K-feldspar	Qz Bt Pl Ms Sil Crd Ilm
CC97-9	sillimanite–K-feldspar / sillimanite–muscovite	Qz Bt Pl Ms Sil Opq
CC95-20	sillimanite–muscovite	Qz Bt Fsp Grt Opq
CC95-X-1	andalusite–cordierite	Qz Bt Pl Ms And Opq
CC2-3A	andalusite–cordierite	Qz Bt Pl Ms And Crd Opq
CC2-1	biotite	Qz Bt Fsp Ms Chl Opq
JO-1	chlorite	Qz (Bt)[1] Pl Ms Chl Opq

[1] Grain size too small to recognise biotite properly

4.1.1 Sillimanite–K-feldspar subzone

Two samples were taken from the sillimanite–K-feldspar subzone in the far east of the peninsula. Sample CC95-11 is a very quartz-rich semi-pelite with a mineral assemblage of quartz, plagioclase, biotite, K-feldspar and sillimanite (Fig. 6). Small opaque grains are observed throughout the thin section. A foliation can be observed in which quartz and plagioclase alternate with biotite. Relatively large K-feldspar grains occur as porphyroblasts and are somewhat aligned to the foliation. Sillimanite occurs as large nodules (also known as sillimanite "smarties") surrounded by rims of quartz and K-feldspar. Biotite and plagioclase do not seem to be in contact with the sillimanite nodules. Both throughout the matrix and near or even adjacent to the sillimanite nodules, small to sometimes medium sized muscovite crystals can be seen. Near the sillimanite nodules, these muscovite crystals seem to be reacting into adjacent minerals such as K-feldspar or biotite, but throughout the matrix they sometimes overgrow biotite and quartz (Fig. 7).

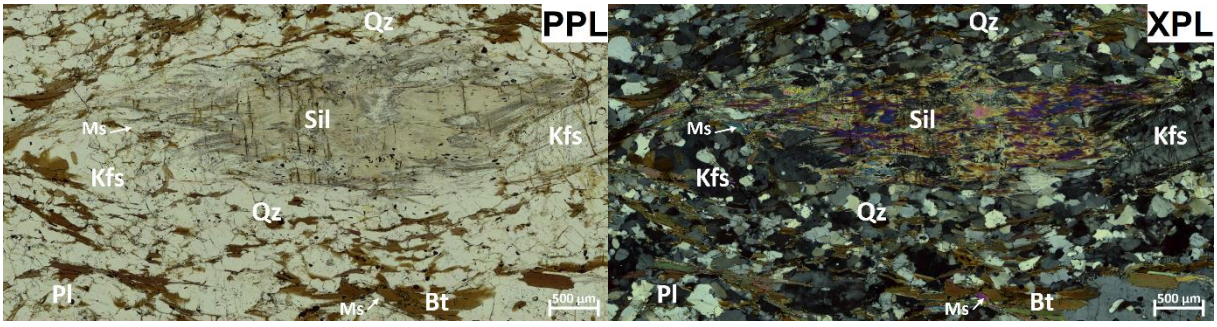

Figure 6: Petrographic images of a large sillimanite nodule surrounded by the mineral assemblage. Scale = 500 µm. Bt = biotite, Kfs = K-feldspar, Ms = muscovite, Pl = plagioclase, Qz = quartz, Sil = sillimanite

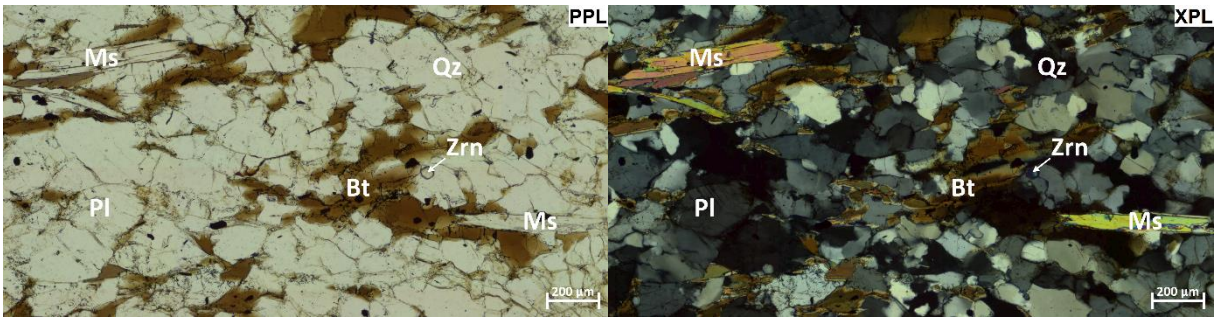

Figure 7: CC95-11. Petrographic images of secondary muscovite growing over biotite and quartz. Scale = 200 µm. Bt = biotite, Ms = muscovite, Pl = plagioclase, Qz = quartz, Zrn = zircon

Sample CC95-12 is taken from the same location but has a more pelitic composition. Its mineral assemblage contains quartz, plagioclase, biotite, muscovite, sillimanite and cordierite (Fig. 8). Apatite occurs as an accessory mineral. Small opaque grains are found throughout the sample within and among other minerals. The sample shows a banded foliation in which bands of quartz alternate with medium to thick bands of biotite. Cordierite occurs as large porphyroblasts containing many inclusions of quartz, plagioclase and biotite. Muscovite is relatively scarce and is mainly found with cordierite within the biotite bands. Larger patches of muscovite in contact with cordierite seem relatively unstable. Smaller elongated muscovite crystals are found mainly in biotite rich bands where they overgrow the pre-existing biotite (Fig. 8). In this sample, sillimanite does not occur as nodules, but rather as patches. These patches consist of thin needles known as fibrolite (Fig. 9). However, patches of prismatic sillimanite can be found as well (Fig. 10). These overgrow cordierite or biotite grains, but they are also found being broken up and bended. Several grains of myrmekite, a vermicular intergrowth of plagioclase and quartz, were also observed.

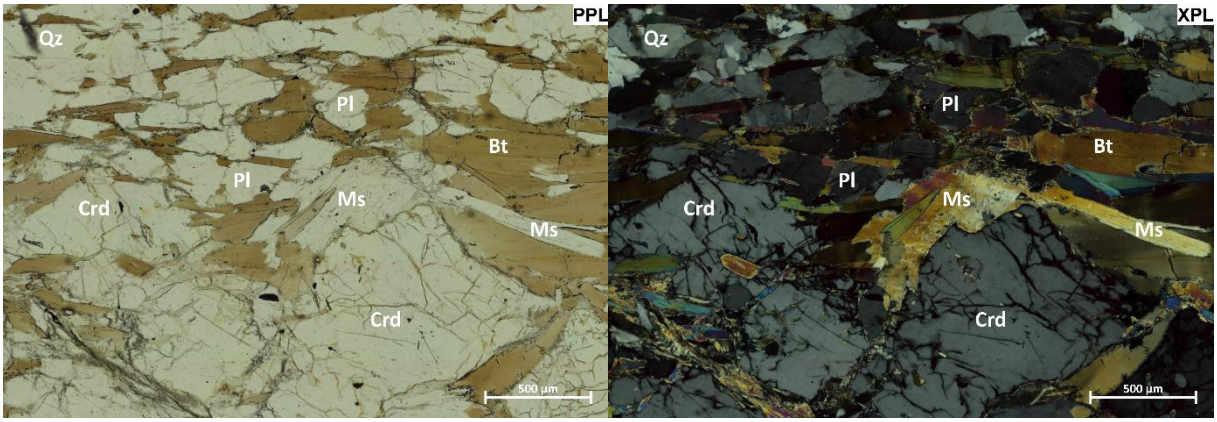

Figure 8: Petrographic overview of sample CC95-12 with muscovite overgrowing biotite. Scale = 500 µm. Bt = biotite, Crd = cordierite Ms = muscovite, Pl = plagioclase, Qz = quartz

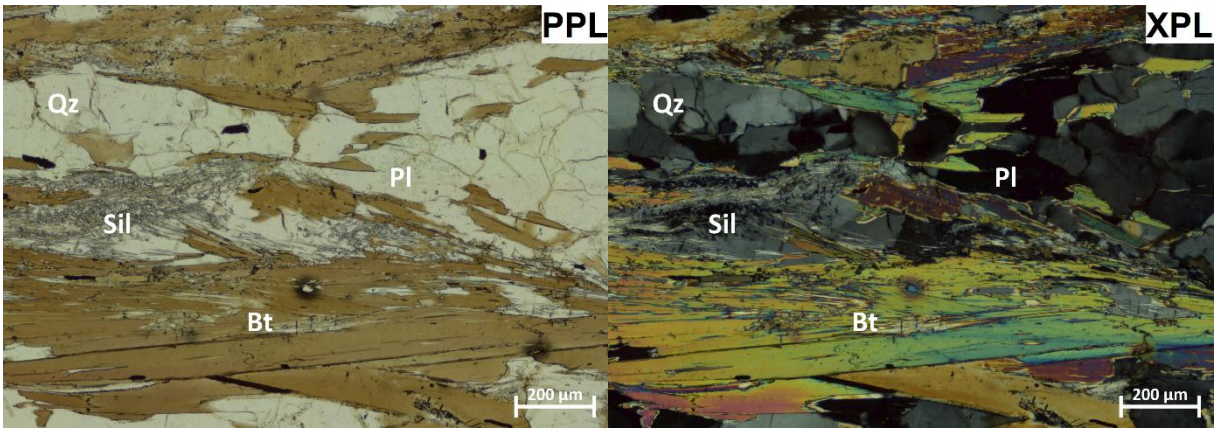

Figure 9: CC95-12. Petrographic image of fibrolite. Scale = 200 µm. Bt = biotite, Pl = plagioclase, Qz = quartz, Sil = sillimanite

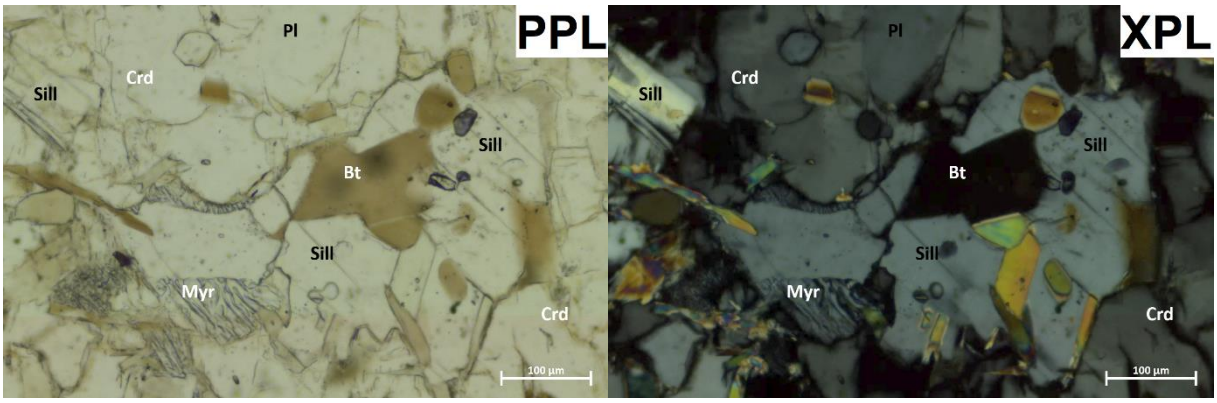

Figure 10: CC95-12. Petrographic image of prismatic sillimanite. Sillimanite on the left has grown over the pre-existing minerals. Scale = 100 µm. Bt = biotite, Crd = cordierite, Myr = myrmekite, Pl = plagioclase, Sil = sillimanite

4.1.2 Sillimanite–muscovite zone

As recently described by Van Melick (2021), sample CC97-9 originates from the boundary between the sillimanite–K-feldspar and the sillimanite–muscovite zone. It has a mineral assemblage of quartz, plagioclase, biotite, muscovite and sillimanite, with apatite and opaques being accessory minerals (Fig. 11). A remnant of andalusite can be found being entirely surrounded by muscovite (Fig. 12).

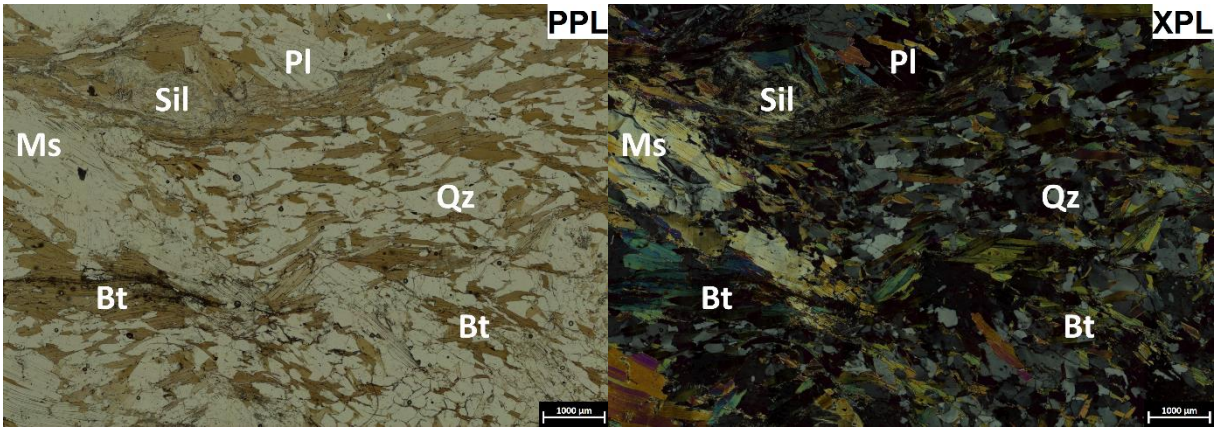

Figure 11: Petrographic overview of CC97-9. Scale = 1000 µm. Bt = biotite, Ms = muscovite, Pl = plagioclase, Qz = quartz, Sil = sillimanite

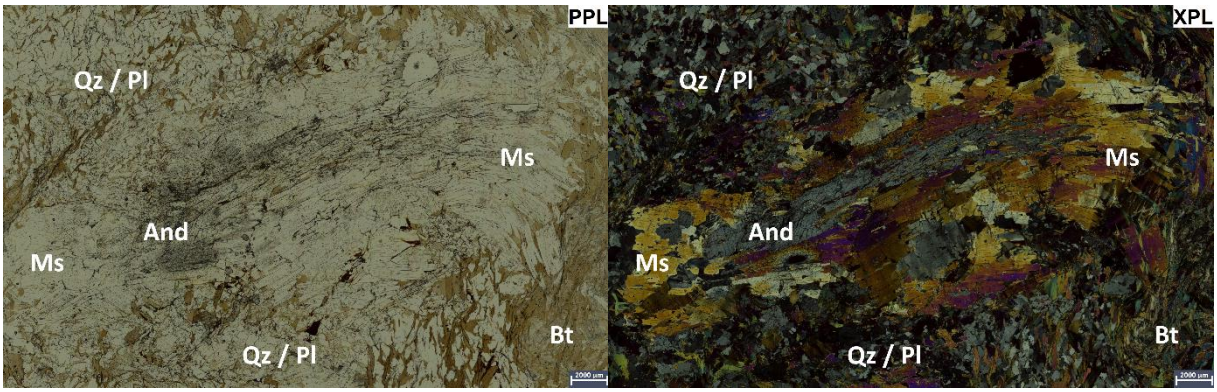

Figure 12: CC97-9. Petrographic image of an andalusite remnant enclosed by a muscovite aggregate. Scale = 2000 µm. And = andalusite, Bt = biotite, Ms = muscovite, Pl = plagioclase, Qz = quartz

Sample CC95-20 appears to be relatively undeformed with an assemblage of mainly quartz and biotite, with several plagioclase and opaque grains and some large garnet porphyroblasts. These garnets contain many inclusions of quartz and opaque minerals (Fig. 13). Although it originates from the sillimanite–muscovite zone, no sillimanite or muscovite was observed in this sample.

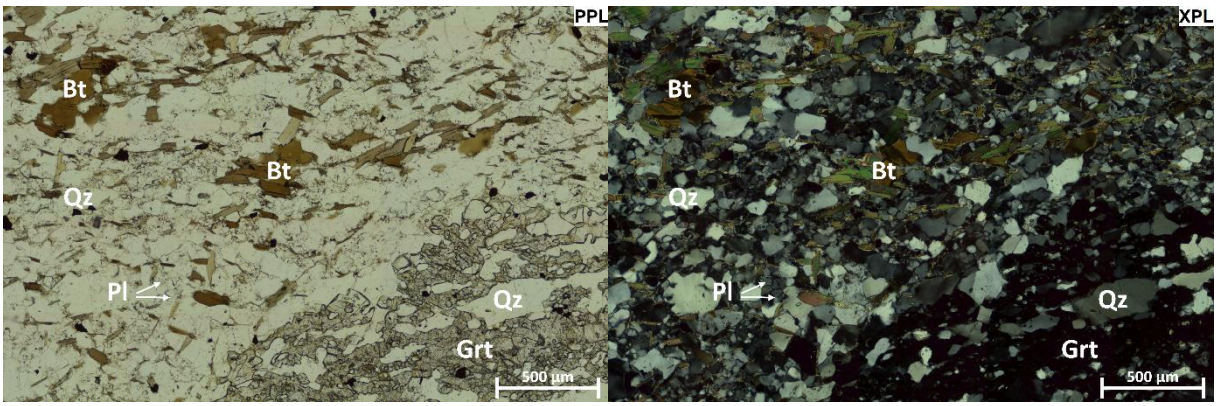

Figure 13: CC95-20. Petrographic image of the breakdown of garnet. Scale = 500 µm. Bt = biotite Grt = garnet, Pl = plagioclase, Qz = quartz

4.1.3 Andalusite–cordierite zone

Sample CC2-3A contains a matrix of quartz, biotite, plagioclase and opaques with a smaller grainsize than the higher-grade samples. Major andalusite and cordierite porphyroblasts have grown over this matrix. These porphyroblasts contain many small inclusions of the matrix minerals. Several small muscovite grains are found throughout the sample, while some larger patches of muscovite occur within the cordierite (Fig. 14). The cordierite porphyroblasts also show a significant yellow coloured rim.

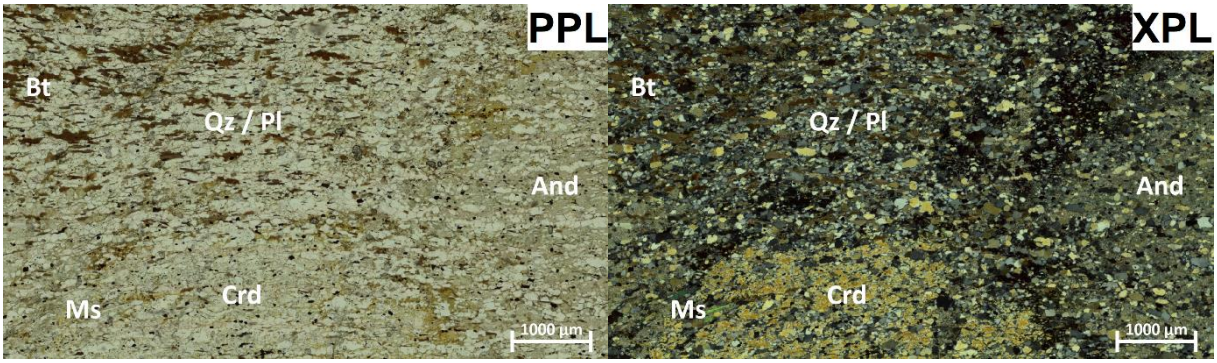

Figure 14: CC2-3A. Petrographic image of cordierite and andalusite porphyroblasts. Scale = 1000 µm. And = andalusite, Bt = biotite, Crd = cordierite, Ms = muscovite, Pl = plagioclase, Qz = quartz

Six thin sections were available from the second sample of this zone, CC95-X. This sample was found west of sample CC2-3A, but the exact location of this sample is unknown. It shows a clear foliation in which quartz and plagioclase bands alternate with biotite rich bands. Large andalusite porphyroblasts have grown pre- to syn-kinematic within the foliation (Fig. 15). They contain many small inclusions of mainly quartz and biotite. Muscovite grains of various sizes have grown both parallel to the foliation and in random directions. Few opaques are present and tourmaline is found as accessory mineral.

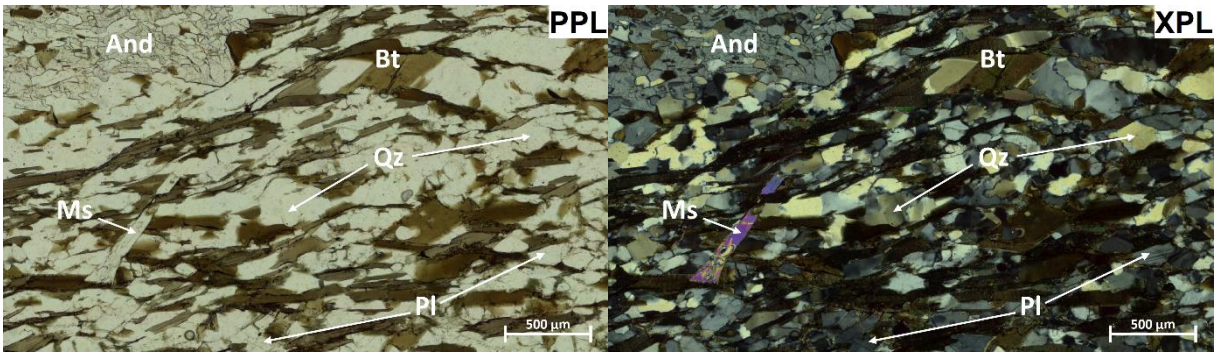

Figure 15: CC95-X-3. Petrographic image of an andalusite porphyroblast surrounded by a foliated fabric of biotite, quartz, plagioclase and muscovite. Scale = 500 µm. And = andalusite Bt = biotite, Ms = muscovite, Pl = plagioclase, Qz = quartz.

4.1.4 Biotite and chlorite zone

The biotite zone (sample CC2-1) contains a foliation with a fine-grained matrix of quartz and chlorite, in which relatively large biotite grains have grown (Fig. 16). Some folded quartz bands are crosscut by bands of biotite and chlorite that are parallel to the fold axes. Several opaques, muscovite and few feldspar grains can be found in the sample.

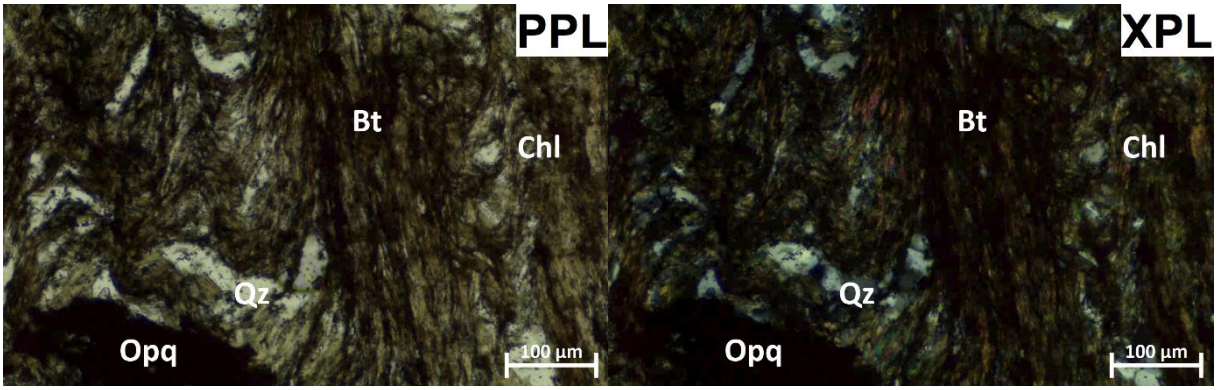

Figure 16: Petrographic overview of CC2-1. Scale = 100 µm. Bt = biotite, Chl = chlorite, Opq = opaque, Qz = quartz.

The chlorite zone is represented by sample JO-1 and contains a very fine-grained matrix of quartz and chlorite (Fig. 17). There may also be some biotite within the matrix, but the matrix is too fine grained too clearly recognise biotite crystals. Muscovite laths have grown on top of the matrix and medium sized feldspar grains have grown within the matrix.

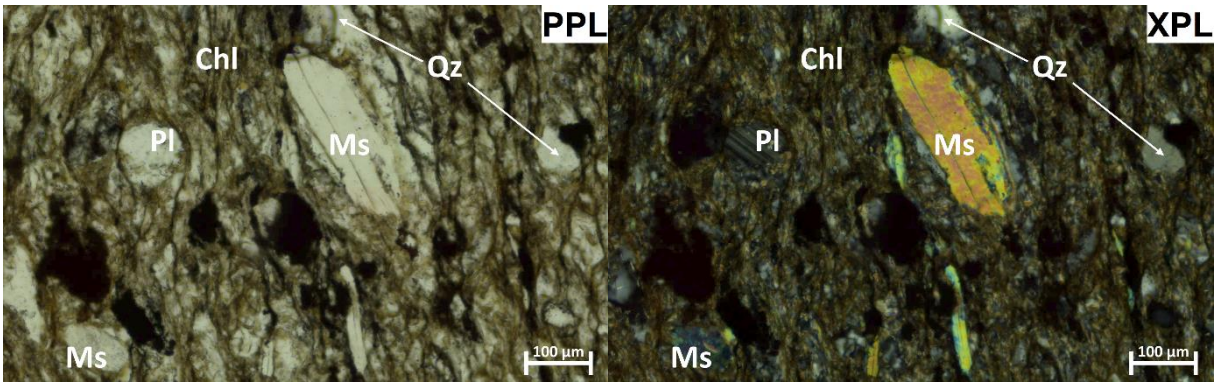

Figure 17: Petrographic overview of JO-1. Scale = 100 µm. Chl = chlorite, Ms = muscovite, Pl = plagioclase, Qz = quartz.

4.1.5 Quartzites

Samples FR1 and FR3 are two quartzites originating from the sillimanite zone. Sample FR1 shows part of a quartzite bordering a metapelite of smaller quartz, biotite, feldspar and opaque grains. The quartzite itself consist of medium to very large sized quartz crystals with very irregular shapes, that are somewhat aligned. The grains show lobate grain boundaries. Along some grain boundaries, groups of smaller grains are found (Fig. 18). An average grain size of 92 µm was measured from these smaller grains from the thin section by using the ZEN 3.2 (blue edition) software. The large grains yielded an average grain size of 752 µm along the short axes and several thousands of microns along the long axes.

Sample FR3 is similar to FR1. This sample entirely consists of quartzite, although several biotite and opaque grains are trapped inside. Large, irregular grains with lobate grain boundary are observed. However, unlike sample FR1, sample FR3 contains smaller grains along most grain boundaries (Fig. 18), which was only seen occasionally in FR1. A smaller average grainsize of approximately 45 µm and was measured for the smaller grains, while the short axes of the large grains yielded 680 µm on average. As in sample FR1, the long axes of the large grains in sample FR3 also yielded sizes of several thousands of microns.

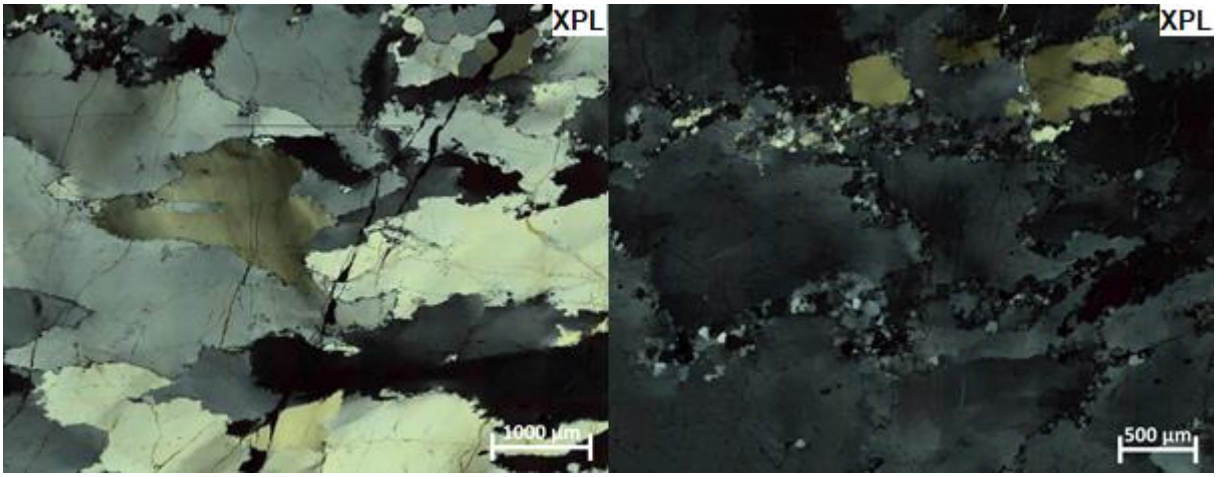

Figure 18: Petrographic images of FR1 (left) and FR3 (right). Note the difference in amount and distribution of smaller quartz grains in FR3 along the grain boundaries compared to FR1. Scale = 1000 µm (left); 500 µm (right).

4.2 Automated mineralogy SEM

Thin sections CC95-11, CC95-12 and CC97-9 have been mapped using SEM-AM. These false colour SEM-AM maps show the spatial distribution of the phases and make it easier to infer reaction and deformation processes. This created a clearer and more detailed view of the mineral assemblage present in the thin sections and reaction processes. The mineralogy of the samples in terms of weight percentage is also calculated (Table 7). The Python script created by Van Melick (2021) converted the data into oxide weight percentages in order to obtain the bulk rock composition (Table 5).

The SEM-AM map of sample CC95-11 (Fig. 19) shows the large abundance of quartz together with plagioclase. The sillimanite nodules seem to be entirely rimmed and encapsulated by muscovite and quartz, causing the sillimanite not to be in contact with biotite, plagioclase or K-feldspar. The majority of the muscovite present occurs around or within the sillimanite nodules. Some single muscovite grains also occur throughout the sample in aggregates of quartz, biotite and plagioclase, as observed with optical microscopy. A significant amount of monazite is also present around the sillimanite nodules. Another clear feature is the alignment of the rounded K-feldspar grains, which are surrounded by quartz, biotite and plagioclase.

Fig. 20 shows the SEM-AM map of sample CC95-12 containing the compositional banding caused by quartz and biotite. Cordierite and sillimanite tend to be restricted to the biotite bands and muscovite is also found in these bands but mainly near or adjacent to cordierite.

As Van Melick (2021) described, the SEM-AM map of CC97-9 (Fig. 21) does not provide any new information, but it gives a better insight on how different phases are associated with each other. Quartz and biotite form large intergrowths with each other and are separated from large patches of muscovite by plagioclase crystals. The andalusite remnant is entirely enclosed by muscovite, while sillimanite is not restricted to certain phases and occurs throughout the sample.

EDS spot measurements were used to obtain the composition of each phase in the above samples. For the different feldspars, the compositions are plotted in Fig. 22 by the use of TernPlot (Marshall, 1996). This resulted in an oligoclase composition for plagioclase for samples CC95-11, CC95-12 and CC97-9. The K-feldspar composition of CC95-11 is approximately 85% orthoclase.

At a later stage in the project, the sillimanite–K-feldspar samples were reinvestigated using EDS spot measurements to determine the oxide phases, in particular iron and titanium oxides. In sample CC95-12, the only iron or titanium oxide phase found was ilmenite, in addition to other heavy phases such as apatite, zircon, xenotime and monazite. In sample CC95-11 resulted, ilmenite and rutile were found, as well as zircon and monazite. In both samples, an iron hydroxide phase was found around holes or cracks in the sample.

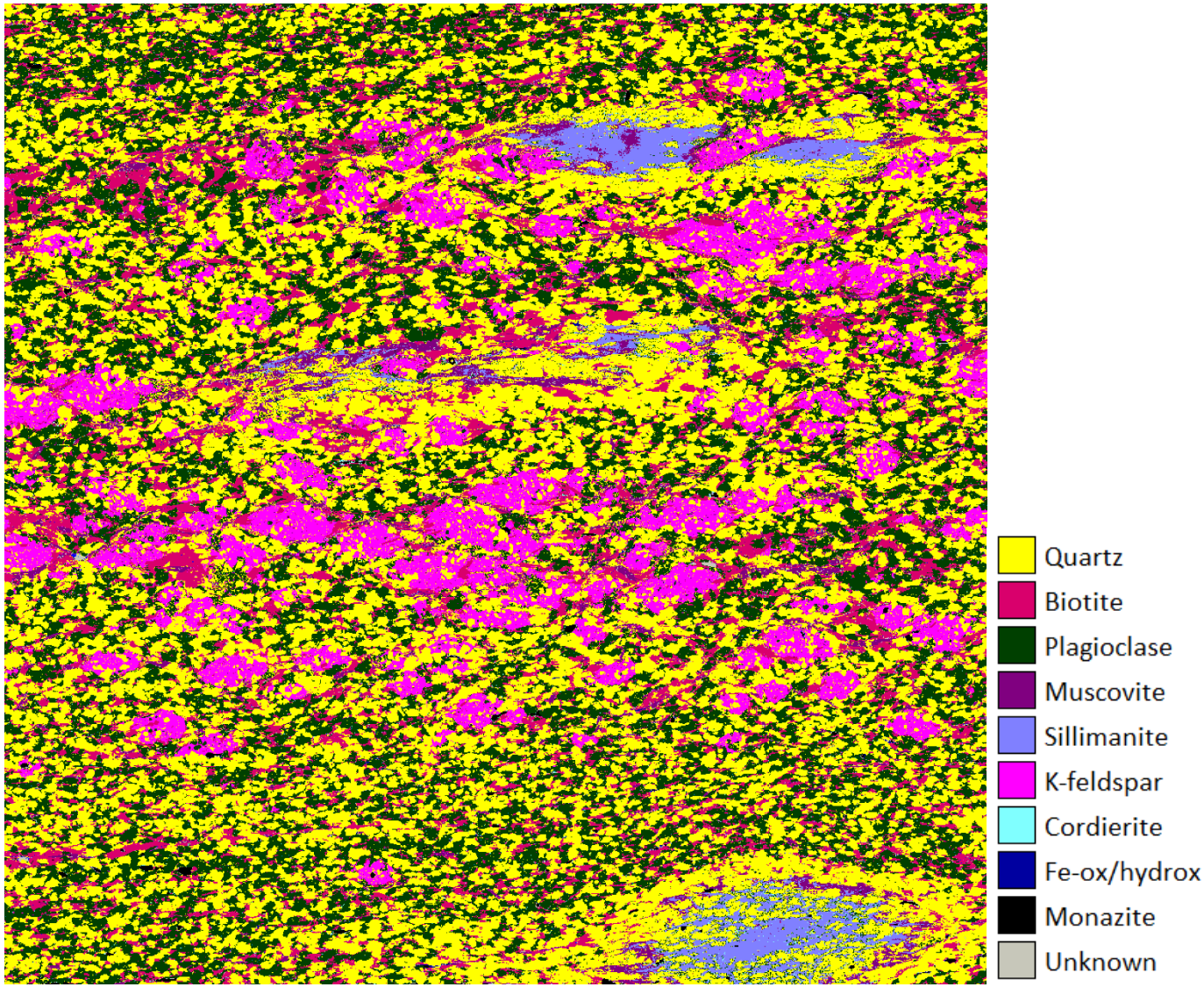

Figure 19: SEM-AM false colour map of CC95-11

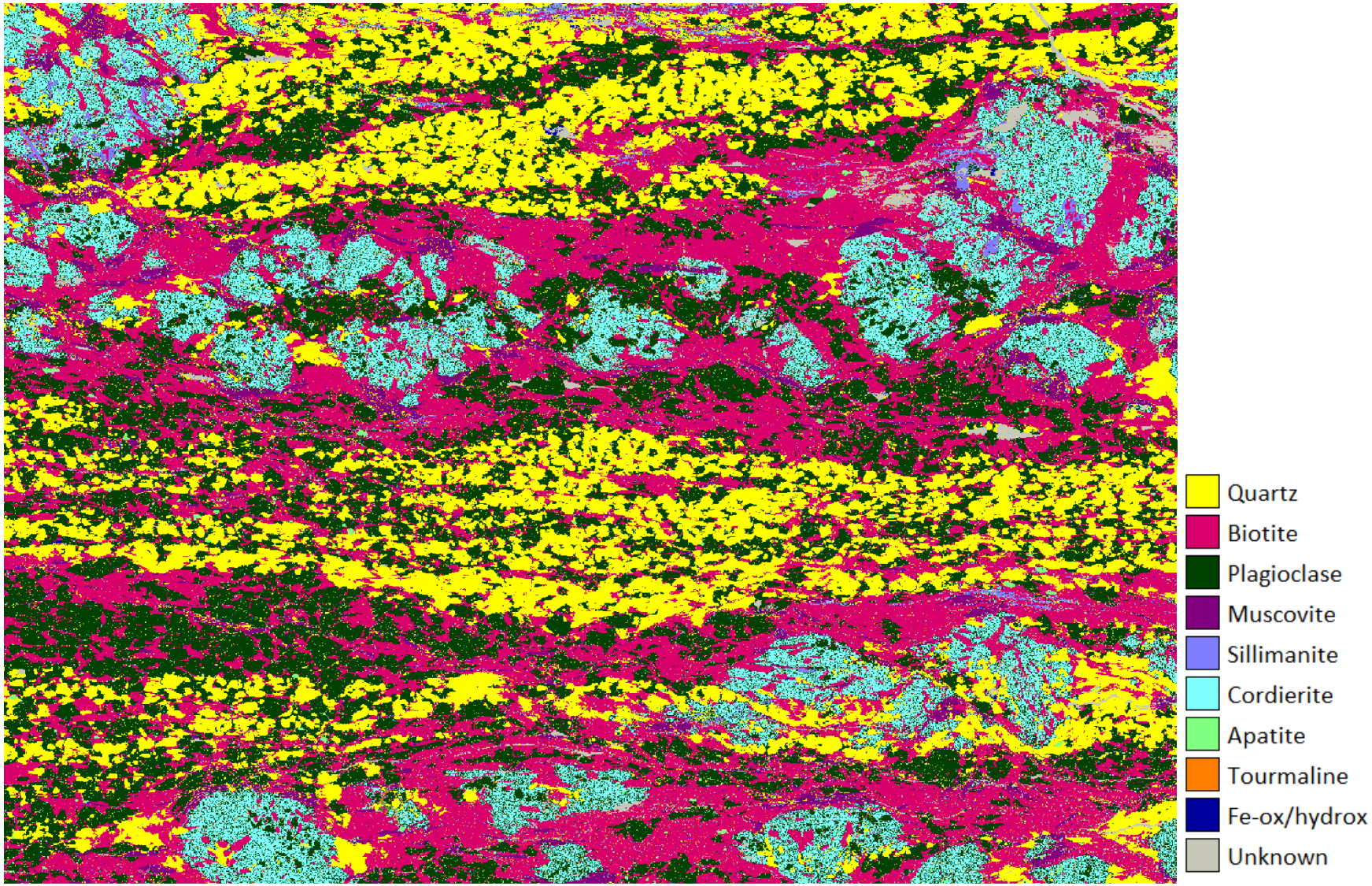

Figure 20: SEM-AM false colour map of CC95-12

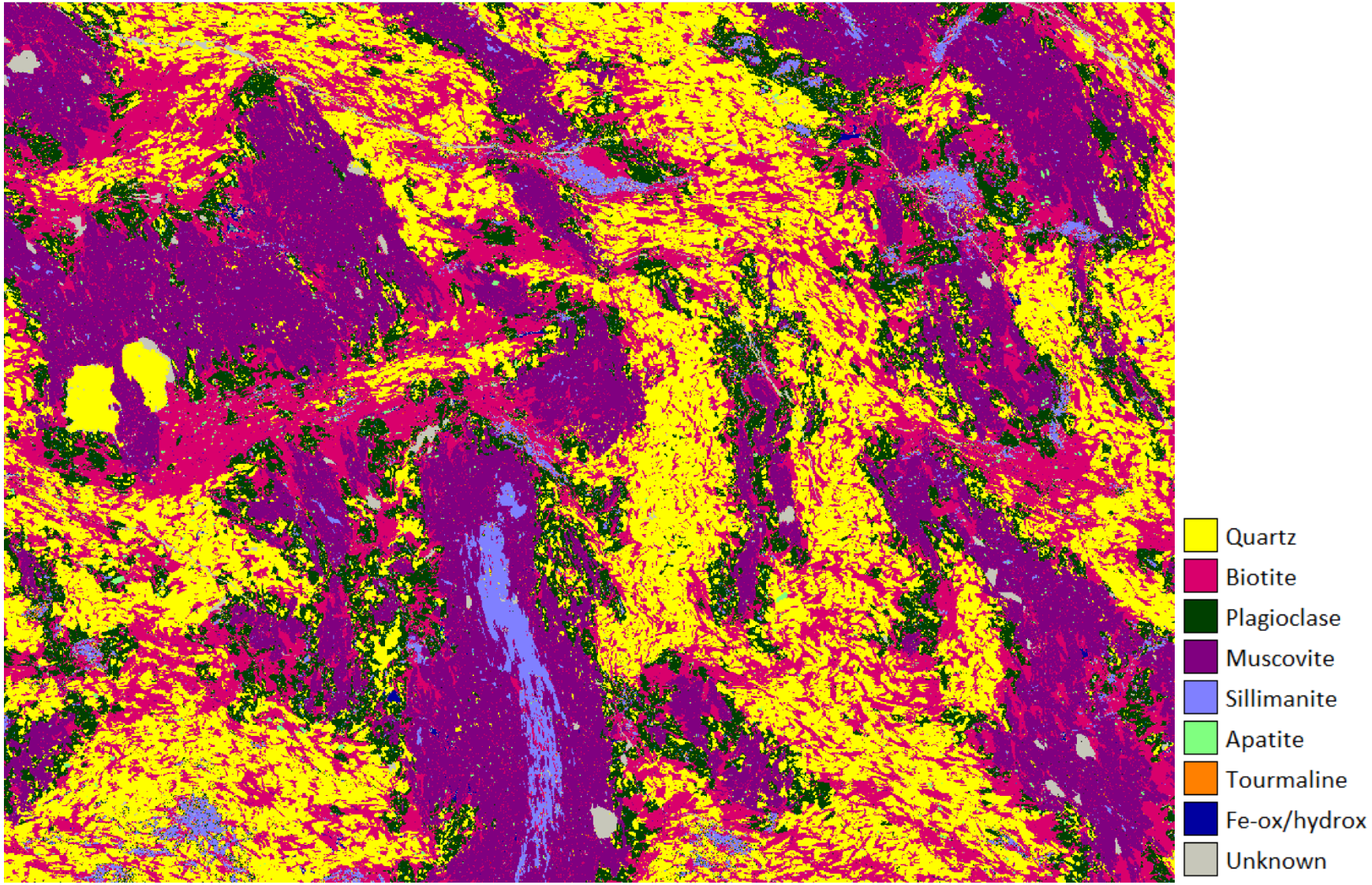

Figure 21: SEM-AM false colour map of CC97-9

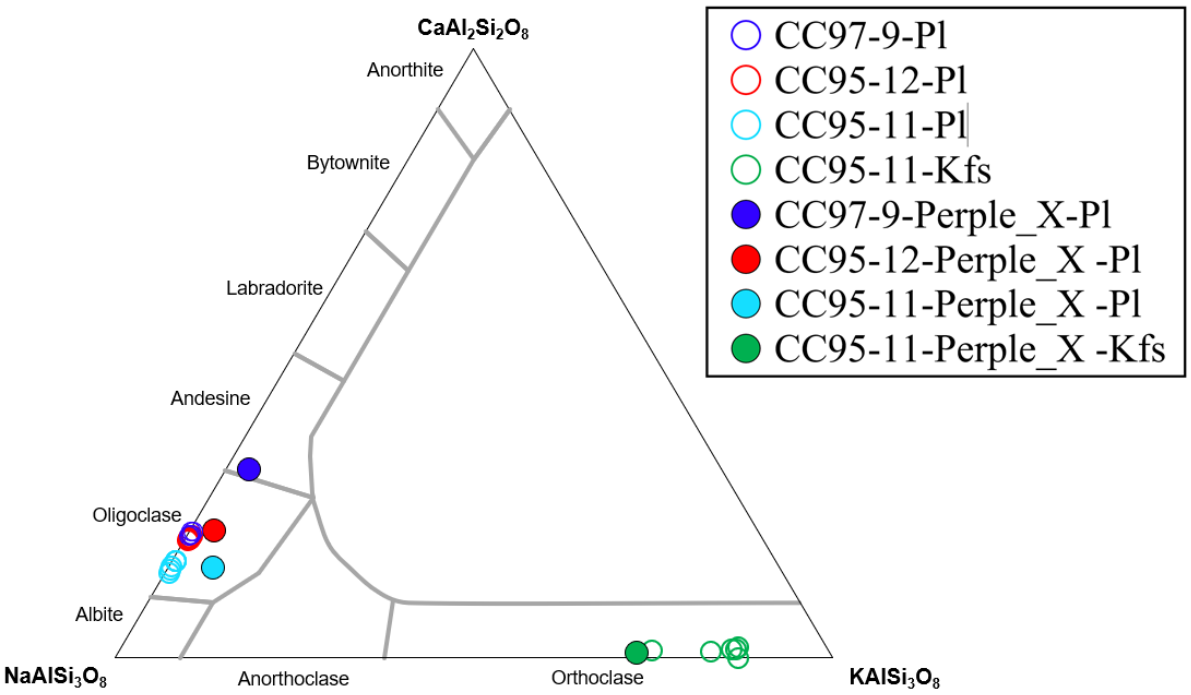

Figure 22: Feldspar composition triangle diagram. Open dots are EDS spot measurement results, coloured dots are Perple_X modelled results. Diagram modelled with TernPlot (Marshall, 1996)

4.3 XRF

XRF analysis was performed on all schist samples from the different metamorphic zones (Table 5). For the highest-grade samples, the XRF and SEM-AM compositions seem to agree with each other fairly well. The most significant difference can be seen in the MnO content in sample CC95-11, in which the SEM-AM MnO content is five times as high as the respective XRF value. This MnO value appears to be rather high compared to all other samples as well. Being a semi-pelitic rock amongst pelitic rocks, the higher SiO2 content of CC95-11 was expected.

Sample CC95-20 from the sillimanite–muscovite zone can be compared to the average sillimanite schist composition from the same zone (Druguet et al., 1995). The main difference is the relative depletion in potassium and the relative enrichment in calcium in CC95-20 compared to the average sillimanite schist. There is also a minor depletion in iron and magnesium in CC95-20. Sample JO-1 from the chlorite zone shows a relative enrichment in silica, but a depletion in aluminium, iron and magnesium compared to a phyllite from the same zone from Druguet (1992).

4.4 LA-ICP-MS

The rare earth element (REE) concentrations were obtained of all metapelites and plotted in chondrite normalised REE diagrams. As the high-grade samples are located close to migmatitic bodies, REE diagrams were plotted to study if any melting has taken place. REE diagrams of the high-grade samples CC95-11, CC95-12 and CC95-20 can be found in Fig. 23, together with a plot of JO-1. The latter sample was plotted as a non-melted reference sample, as it is not expected that partial melting took place in the chlorite zone.

The four plots show a similar trend in which elemental abundance decreases with increasing atomic weight. The samples are enriched in the LREE compared to chondrite and show a negative peak in europium.

Table 5: Major element compositions of metapelites from the different metamorphic zones

	CC95-12		CC95-11		CC97-9 [1]		CC95-20	Sill-s [2]
	sill–Kfs		*sill–Kfs*		*sill–Kfs / sill–ms*		*sill–ms*	*sill–ms*
wt%	AM	XRF	AM	XRF	AM	XRF	XRF	XRF
SiO_2	58.85	65.31	70.73	71.17	58.39	59.98	68.78	68.84
Al_2O_3	19.58	14.84	15.10	13.62	20.37	18.58	13.60	13.40
Fe_2O_3	8.01	6.55	3.79	3.21	8.63	7.11	4.82	5.82
MgO	4.48	3.08	2.02	1.50	3.33	3.05	1.77	2.51
CaO	1.40	1.53	0.94	1.26	1.16	0.80	3.73	2.14
Na_2O	2.81	2.06	2.99	2.60	1.46	1.25	2.19	2.90
K_2O	3.42	2.77	3.06	3.28	5.49	4.87	1.67	2.87
TiO_2	1.13	0.71	1.00	0.57	0.93	0.82	0.84	0.70
MnO	0.18	0.10	0.27	0.05	0.14	0.09	0.12	0.08
LOI		1.06		0.88		1.76	0.44	

	CC95-X-1	CC2-3A	CC2-1	JO-1	Phyl [3]
	and–crd	*and–crd*	*biotite*	*chlorite*	*chlorite*
wt%	XRF	XRF	XRF	XRF	XRF
SiO_2	64.03	64.54	62.64	66.95	63.00
Al_2O_3	14.95	16.10	16.06	13.41	16.40
Fe_2O_3	6.71	6.49	6.41	5.21	6.03
MgO	2.97	2.64	2.76	1.72	2.55
CaO	2.04	1.22	0.82	0.77	0.83
Na_2O	2.42	2.68	0.74	2.69	2.63
K_2O	3.09	1.93	4.05	2.95	3.67
TiO_2	0.71	0.86	0.76	0.83	0.74
MnO	0.10	0.10	0.08	0.08	0.07
LOI	1.35	1.77	4.10	3.47	

[1] Bulk rock composition from Van Melick (2021)
[2] Average sillimanite schist composition from sill–ms zone from Druguet et al. (1995)
[3] Average phyllite composition from chlorite zone from Druguet (1992)

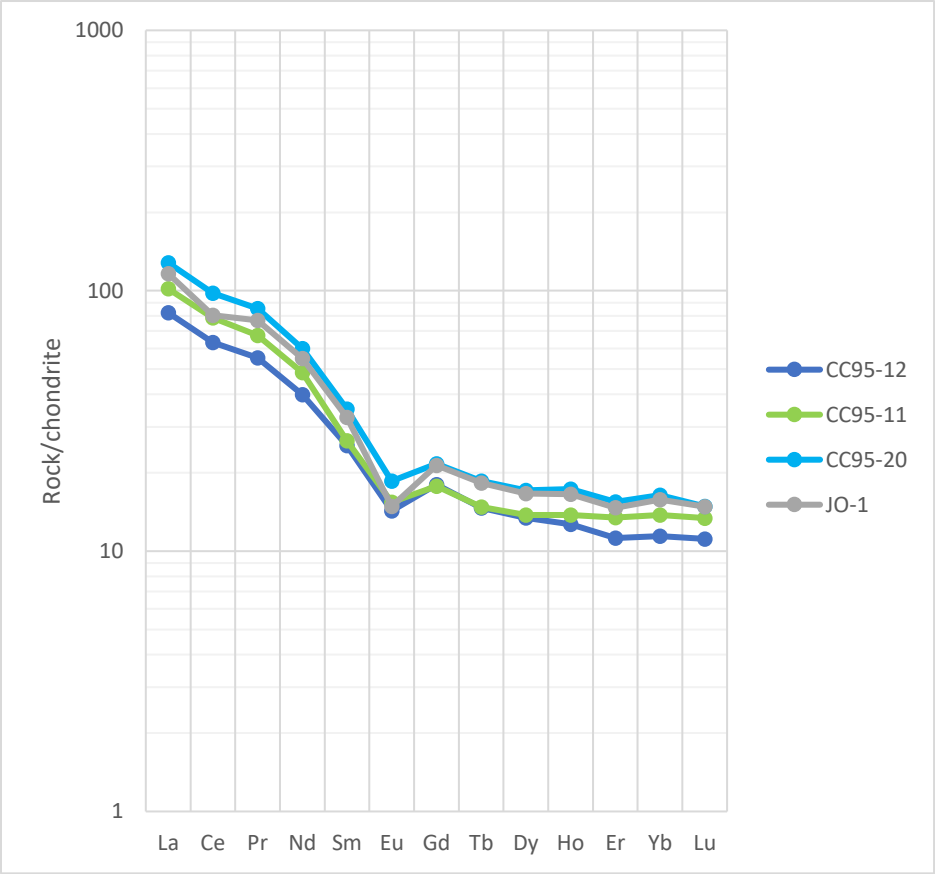

Figure 23: Chondrite normalised (Nakamura, 1974) REE diagram plots of high metamorphic grade samples and JO-1 as reference sample.

4.5 Thermodynamic modelling

4.5.1 Determining Fe^{2+}/Fe^{3+} ratio

The effect of a varying Fe^{2+}/Fe^{3+} ratio on the mineral assemblages in the samples was tested on sample CC95-12. Baseline modelling was performed with $X_{Fe^{2+}} = 0.75$ (Forshaw & Pattison, 2021), in which $X_{Fe^{2+}} = Fe^{2+} / (Fe^{2+} + Fe^{3+})$. In order to assess the impact on the mineral assemblage, $X_{Fe^{2+}}$ was subsequently varied between 0 and 1 with step sizes of 0.25, plotting temperature against pressure (Fig. 24a–e). In addition, $X_{Fe^{2+}}$ was plotted against pressure with a fixed temperature of 650°C and 675°C (Fig. 24f–g). The results show that at a very low iron ratio ($X_{Fe^{2+}} < 0.10$) a mineral assemblage of Qz + Bt + Pl + Ms + Sil + Crd, complemented with the oxides hematite and rutile is stable. This is the mineral paragenesis observed during optical microscopy and SEM-AM. At a $X_{Fe^{2+}} = 0.55 - 0.85$, a mineral assemblage of Qz + Bt + Pl + Sil + Crd (Ms is absent) is stable, complemented with magnetite and rutile as oxides. This mineral assemblage remains stable with increasing $X_{Fe^{2+}}$. At $X_{Fe^{2+}} > 0.85$, rutile is the only stable oxide, while at $X_{Fe^{2+}} > 0.95$, the oxide ilmenite is added to the assemblage. At $X_{Fe^{2+}}$ values of 0.10–0.55, no field fits with the observed mineral assemblage, as the system either contains K-feldspar, or lacks cordierite.

The same approach was applied to sample CC95-11, and the results matched with CC95-12. For this sample, however, garnet was modelled to be stable in every field throughout the modelled pseudosections, even though there is no garnet observed in the thin section. The obtained MnO content in this sample was rather high in SEM-AM (Table 5). As Symmes & Ferry (1992) show, MnO strongly partitions into garnet relative to other minerals, suggesting that the MnO content used in modelling was too high. In order to correct for this, the pseudosections were modelled with the SEM-AM bulk rock composition, but with the MnO value obtained from XRF analysis.

In other to determine the most likely conditions, the sillimanite–K-feldspar samples were studied again with EDS spot measurements (see section 4.2) in the hunt for iron oxides. This resulted in the discovery of ilmenite and rutile in the thin sections, meaning that the $X_{Fe^{2+}} = 0.95-1.00$ in the sillimanite–K-feldspar subzone. Assuming that this iron ratio is consistent throughout the different metamorphic zones, thermodynamic modelling was performed on the remaining samples with an average $X_{Fe^{2+}}$ value of 0.975.

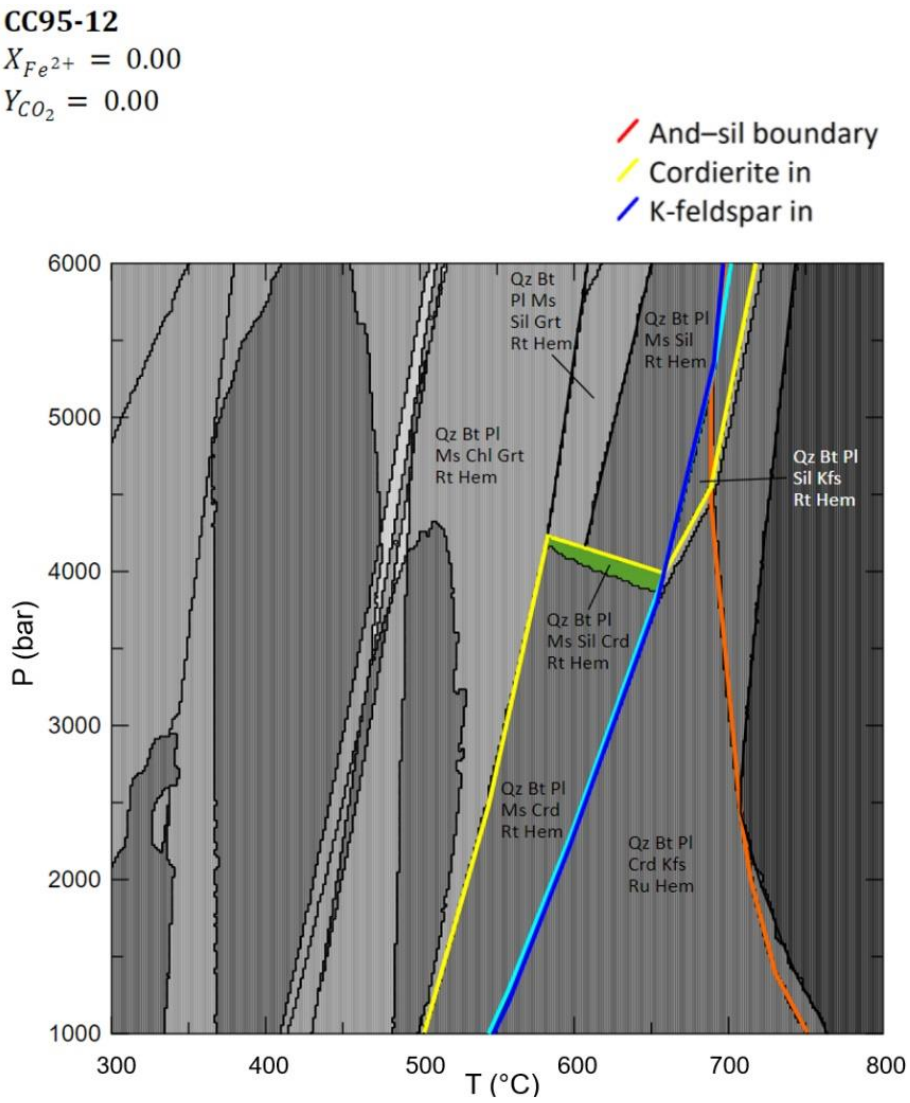

Figure 24a: Pseudosection for CC95-12 with $X_{Fe^{2+}} = 0.00$.

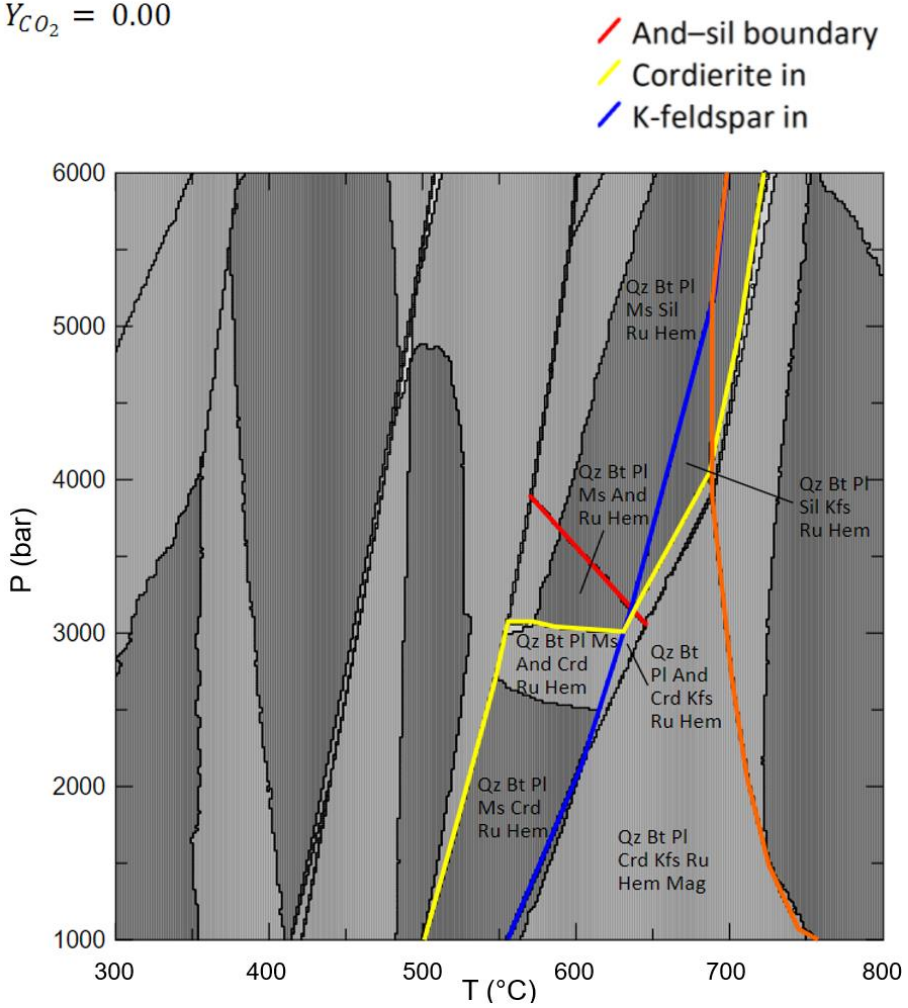

Figure 24b: Pseudosection for CC95-12 with $X_{Fe^{2+}} = 0.25$.

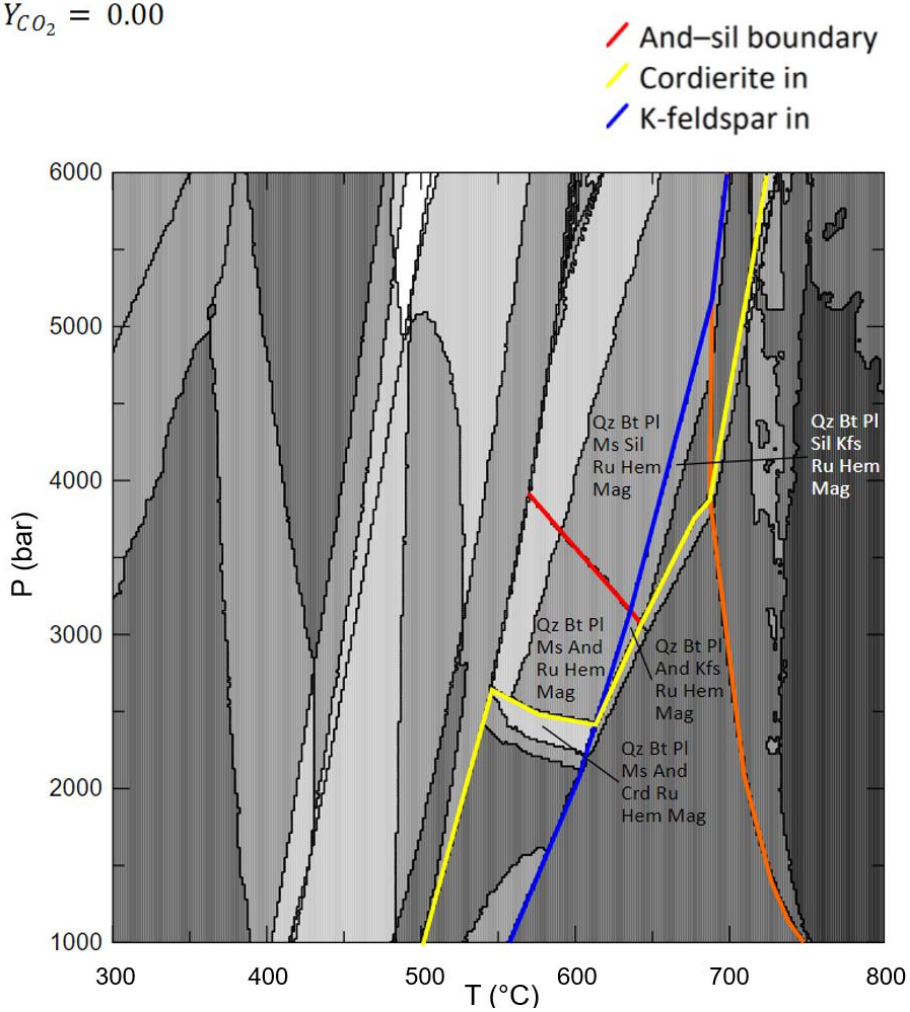

Figure 24c: Pseudosection for CC95-12 with $X_{Fe^{2+}} = 0.50$.

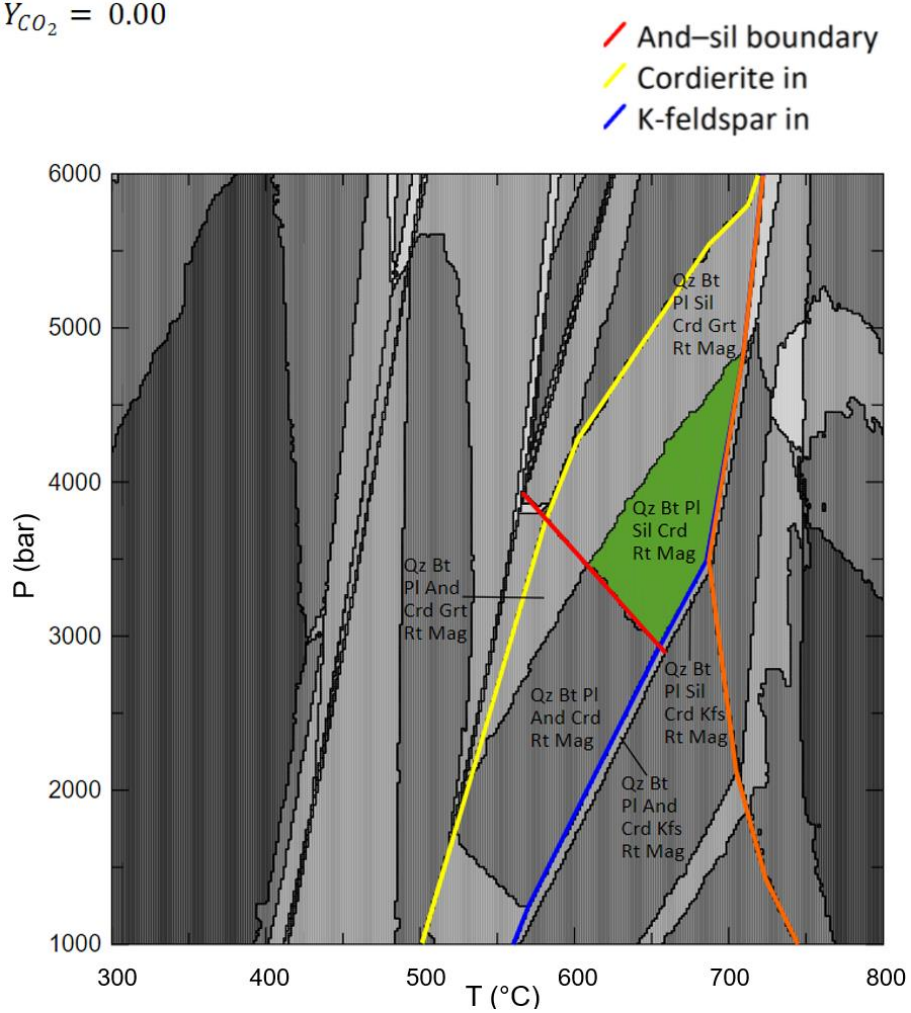

Figure 24d: Pseudosection for CC95-12 with $X_{Fe^{2+}} = 0.75$.

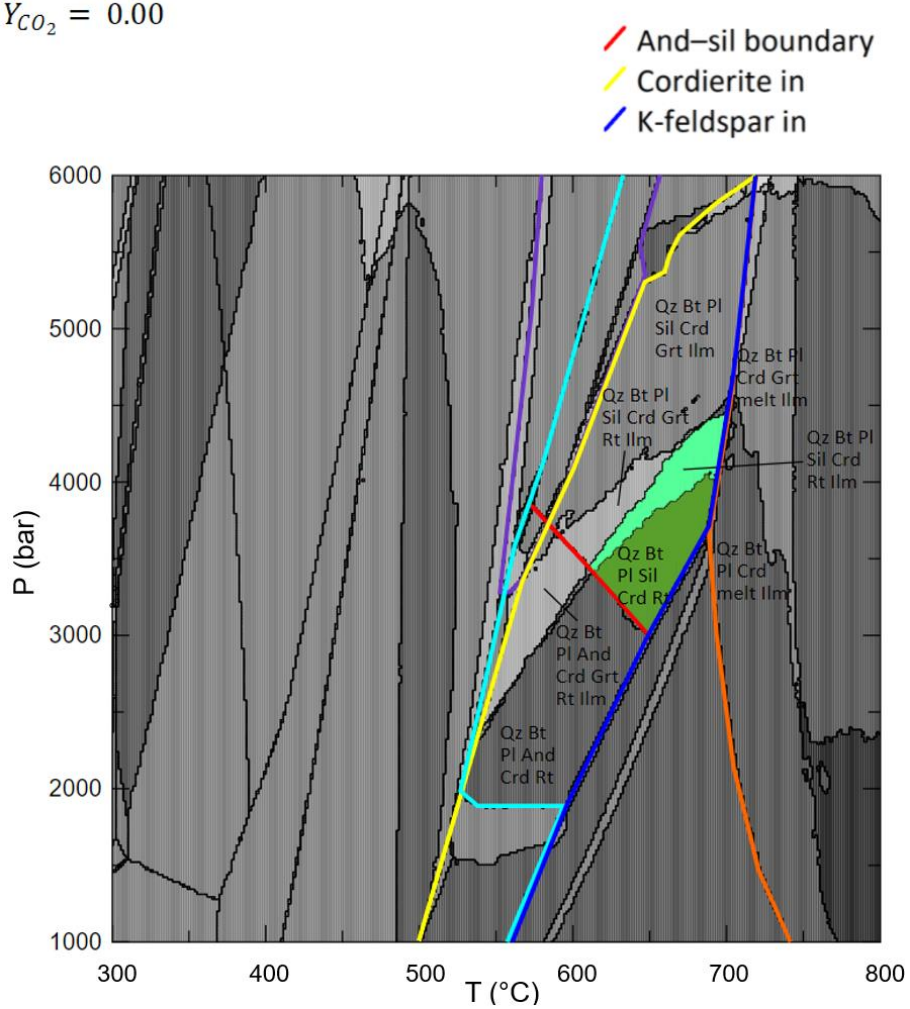

Figure 24e: Pseudosection for CC95-12 with $X_{Fe^{2+}} = 0.99$.

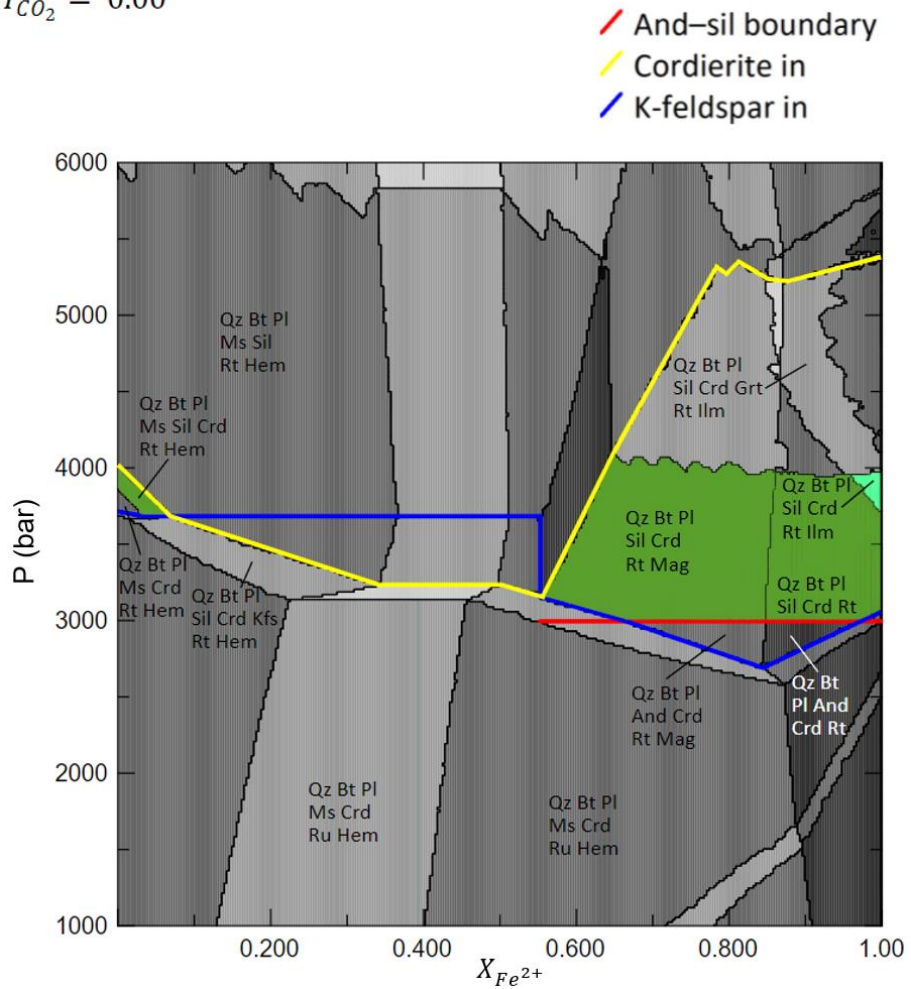

Figure 24f: Pseudosection plotting pressure against $X_{Fe^{2+}}$ with T = 650°C.

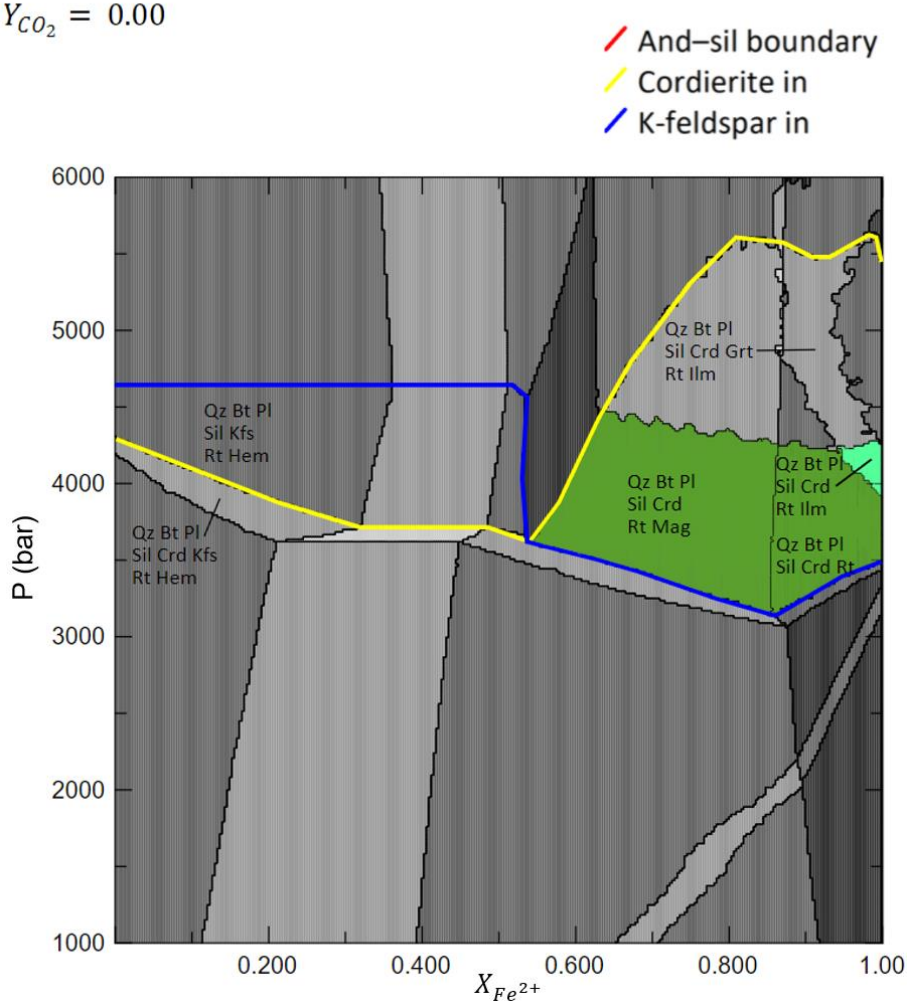

Figure 24g: Pseudosection plotting pressure against $X_{Fe^{2+}}$ with T = 675°C.

4.5.2 P–T estimates

A pseudosection of CC97-9 was modelled with its SEM-AM bulk rock composition. All remaining metapelites were modelled using their respective XRF analysis bulk rock composition. Fig. 25–32 show the obtained pseudosections with their respective stable field coloured in green. Table 6 gives an overview of all P–T estimates. In the middle of each stable field, the predicted composition of the solution models and the quantified mineral composition were obtained. The predicted feldspar compositions of the high-grade samples were plotted in the feldspar ternary diagram for comparison (Fig. 23). Oligoclase is predicted as plagioclase in sample CC95-11 and CC95-12, which matches with the measured values. For sample CC97-9, an andesine composition is predicted. The predicted mineral proportions were compared with the obtained mineral proportions from the SEM-AM (Table 7).

Despite their different mineral assemblages and bulk rock compositions, the sillimanite–K-feldspar samples show similar P–T estimates. However, for both samples muscovite is modelled to be unstable with the rest of the assemblage. Moreover, the indicated stable field lacks ilmenite in the pseudosection of sample CC95-11 (Fig. 25). According to the pseudosection, ilmenite enters the system when temperatures exceed 700°C, which is almost the same temperature at which cordierite enters the system (at 690°C at 4.0 kbar). In other words, ilmenite can only be stable when cordierite is stable, but cordierite was not found in sample CC95-11. Therefore, the indicated stable field in Fig. 25 is lacking ilmenite.

Perple_X modelling predicts rutile to be stable in both samples CC95-11 and CC95-12, although it was not observed in the latter. Based on the similar TiO_2 amount in CC95-11 and CC95-12 (0.98 and 1.13 respectively), it is however likely that rutile is also present in sample CC95-12.

The mineral assemblage of sample CC95-20 is predicted to be stable at a higher temperature and a significantly higher pressure (4.5–6.0 kbar) than the other high-grade samples. Despite originating from the sillimanite–muscovite zone, neither sillimanite nor muscovite was observed optically. At the modelled pressure, muscovite becomes unstable when exceeding 575°C. However, sillimanite is stable up to a temperature of 650°C.

Sample CC2-3A also lacks muscovite in the modelled assemblage. Muscovite becomes unstable when cordierite and andalusite stabilise. The biotite and chlorite zone samples show a fairly constrained temperature range, but they are poorly constrained in pressure (1.0–5.0 kbar). The chlorite zone also shows that biotite is modelled to be stable at any temperature.

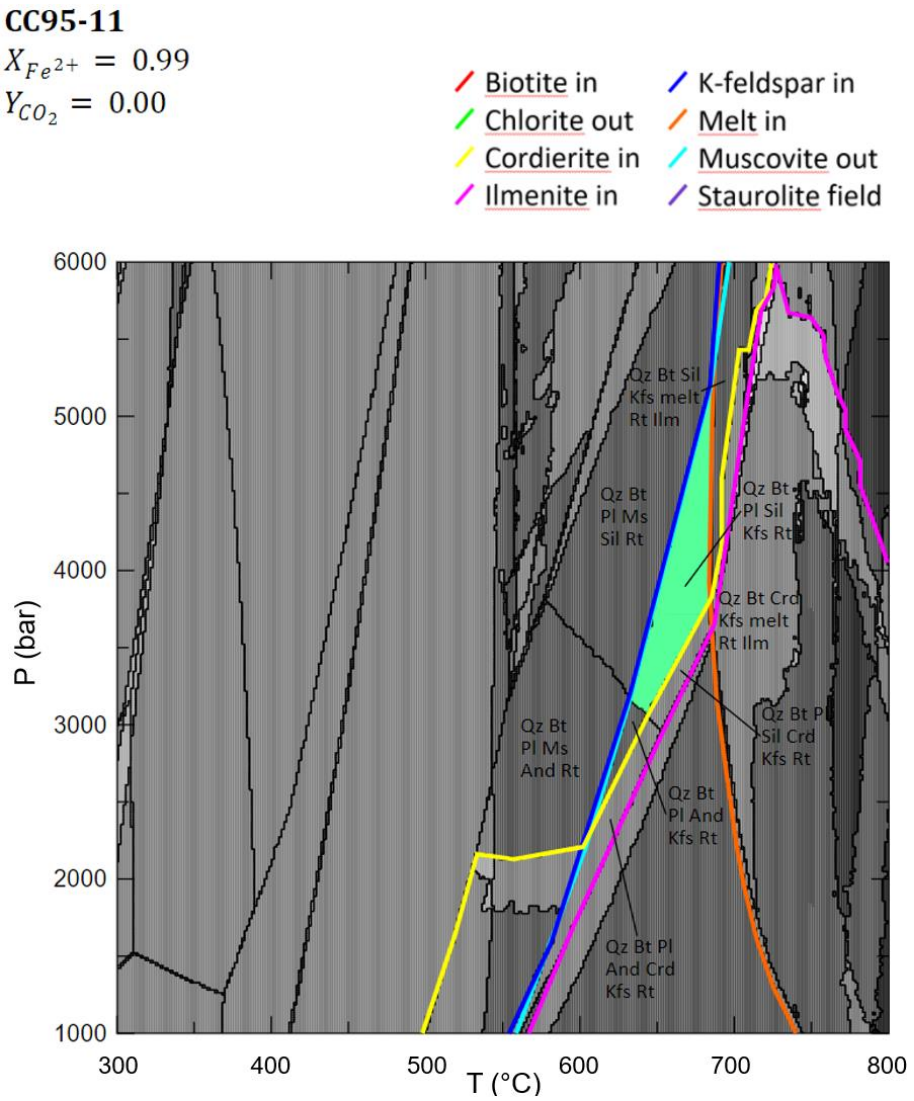

Figure 25: Pseudosection for CC95-11 of the sillimanite–K-feldspar subzone

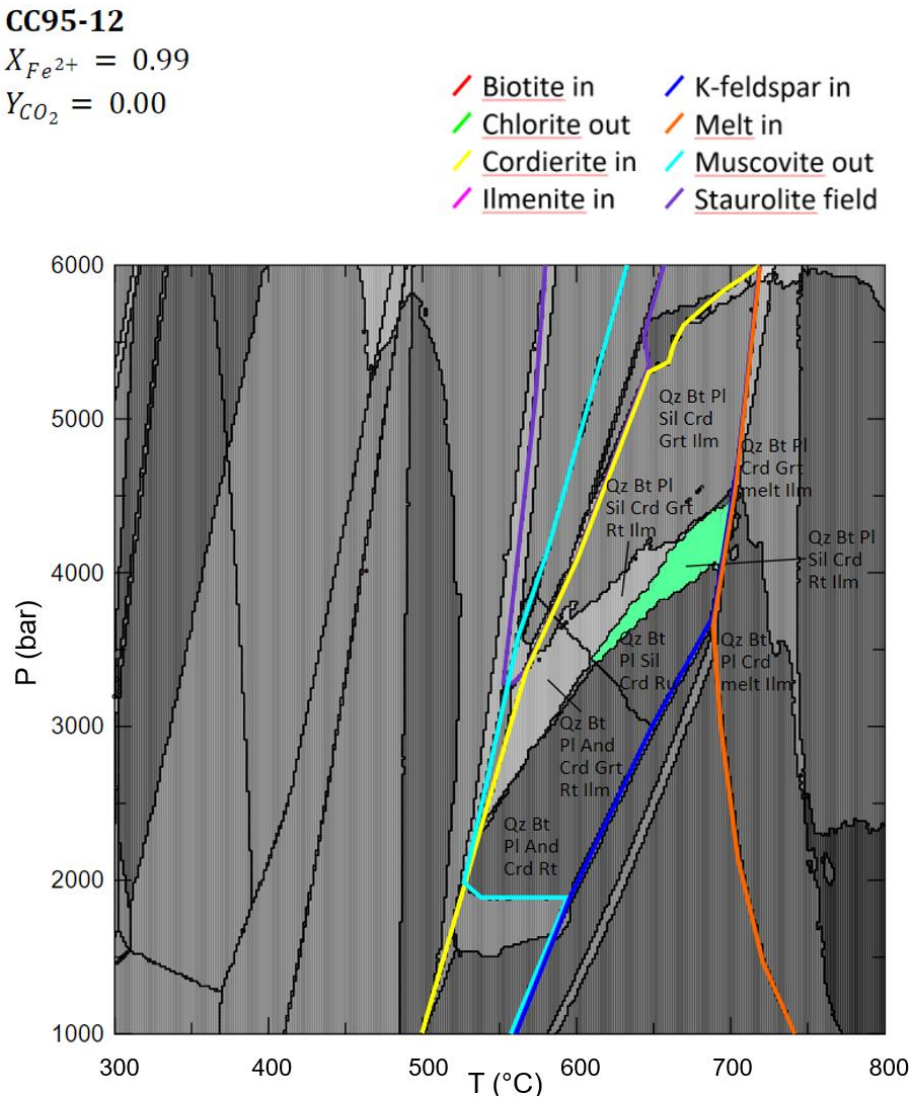

Figure 26: Pseudosection for CC95-12 of the sillimanite–K-feldspar subzone

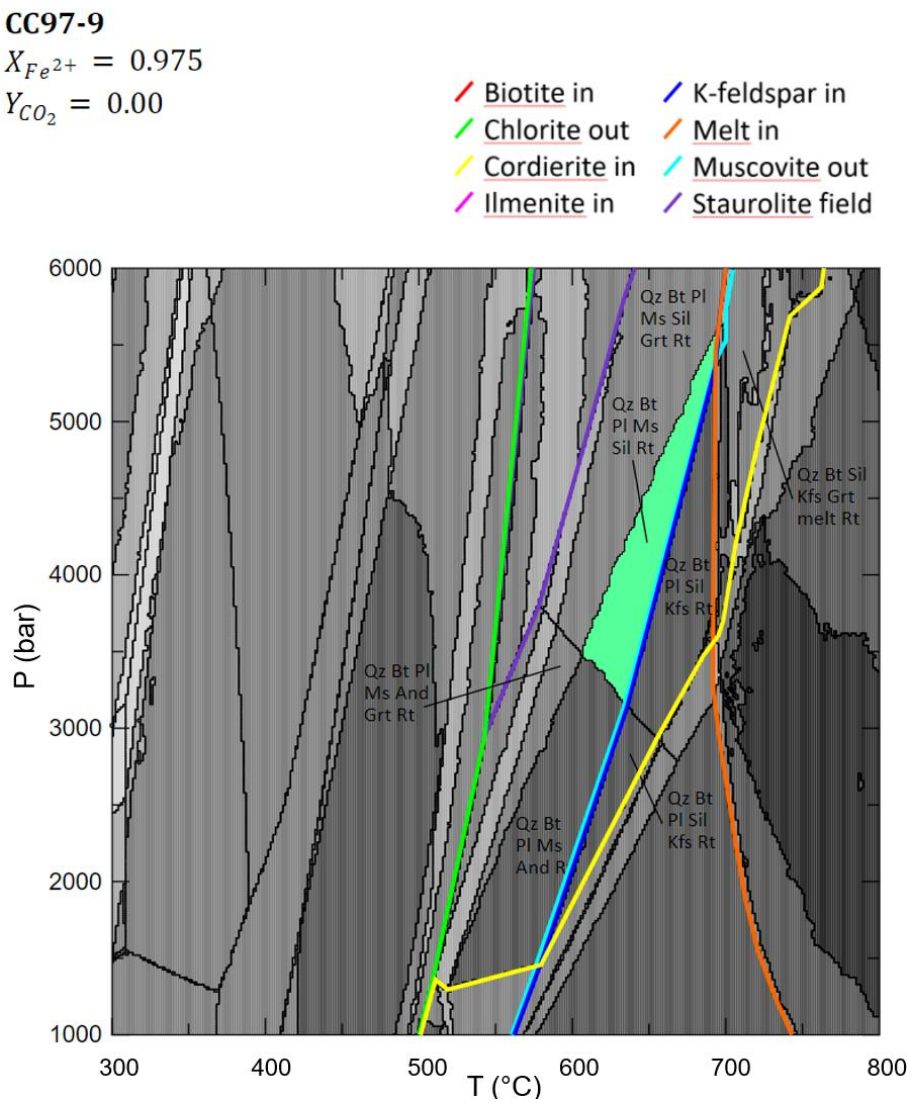

Figure 27: Pseudosection for CC97-9 of the sillimanite–muscovite zone / sillimanite–K-feldspar subzone

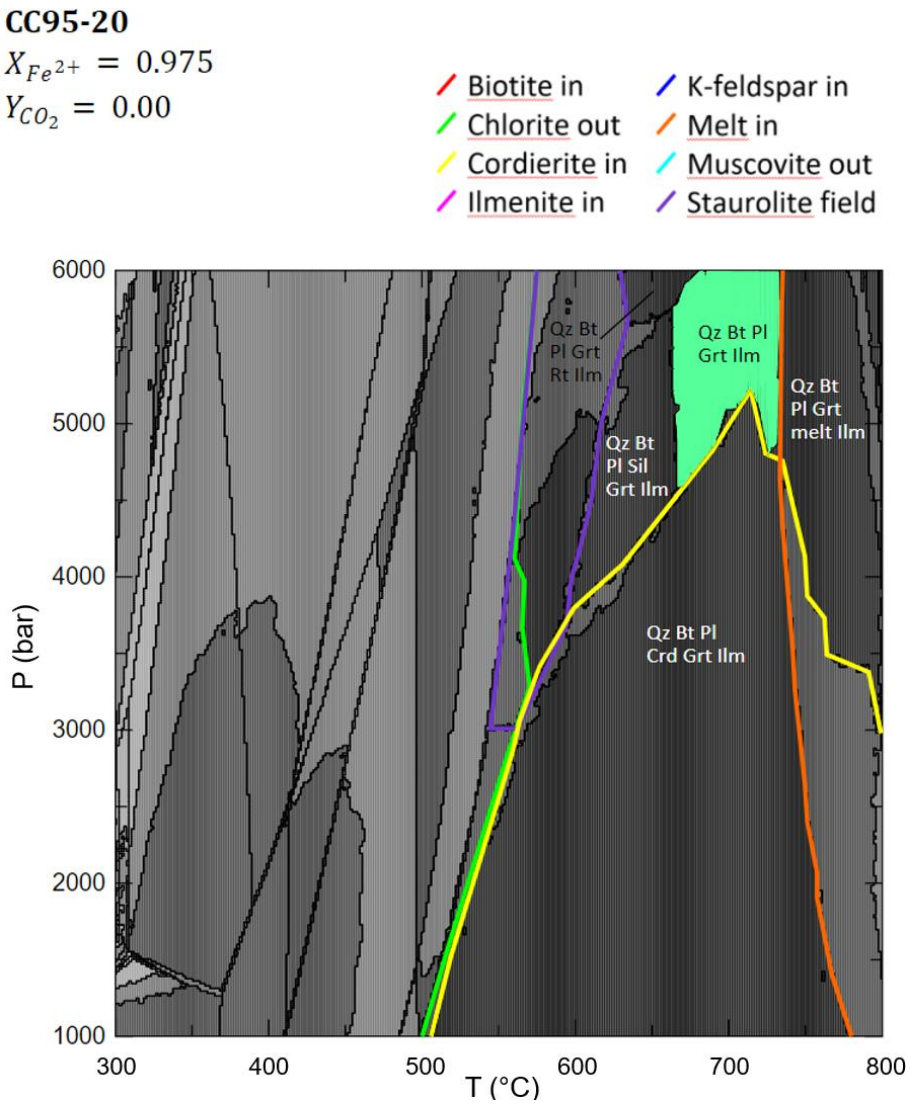

Figure 28: Pseudosection for CC95-20 of the sillimanite–muscovite zone

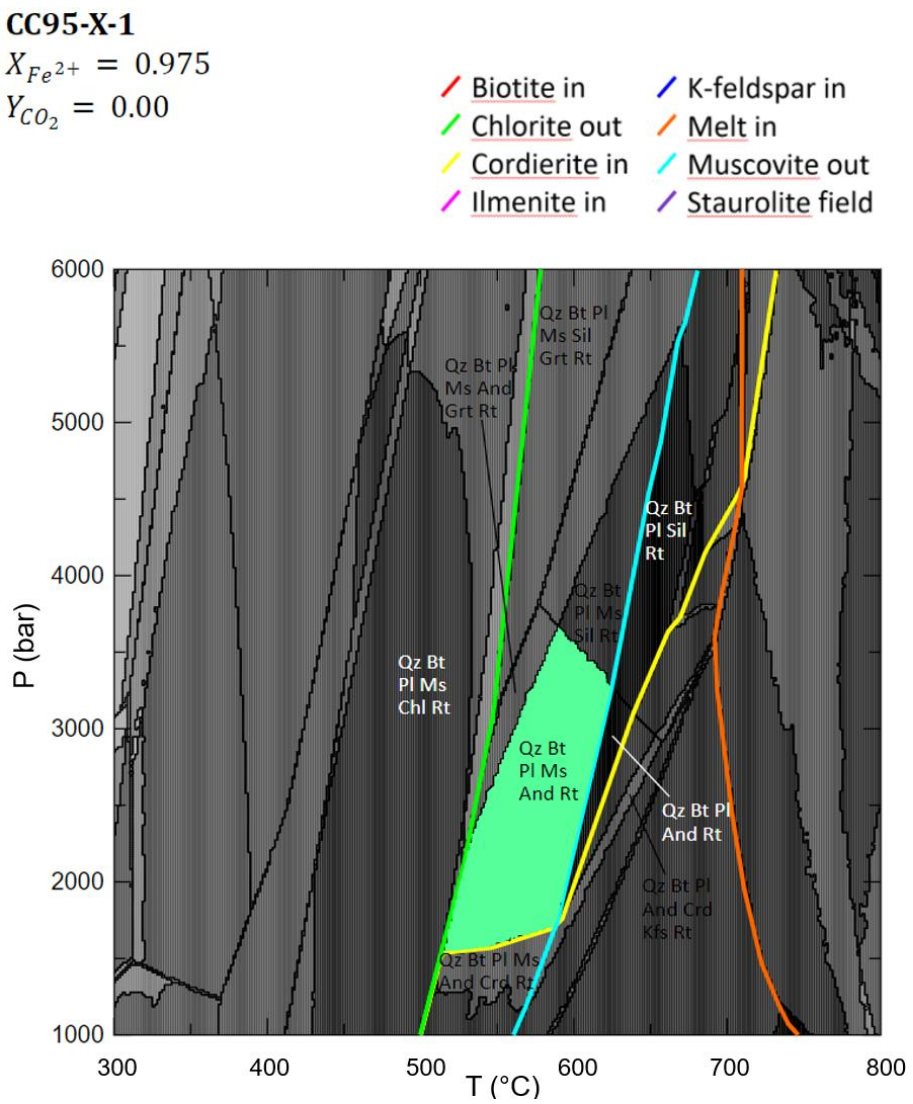

Figure 29: Pseudosection for CC95-X-1 of the andalusite–cordierite zone

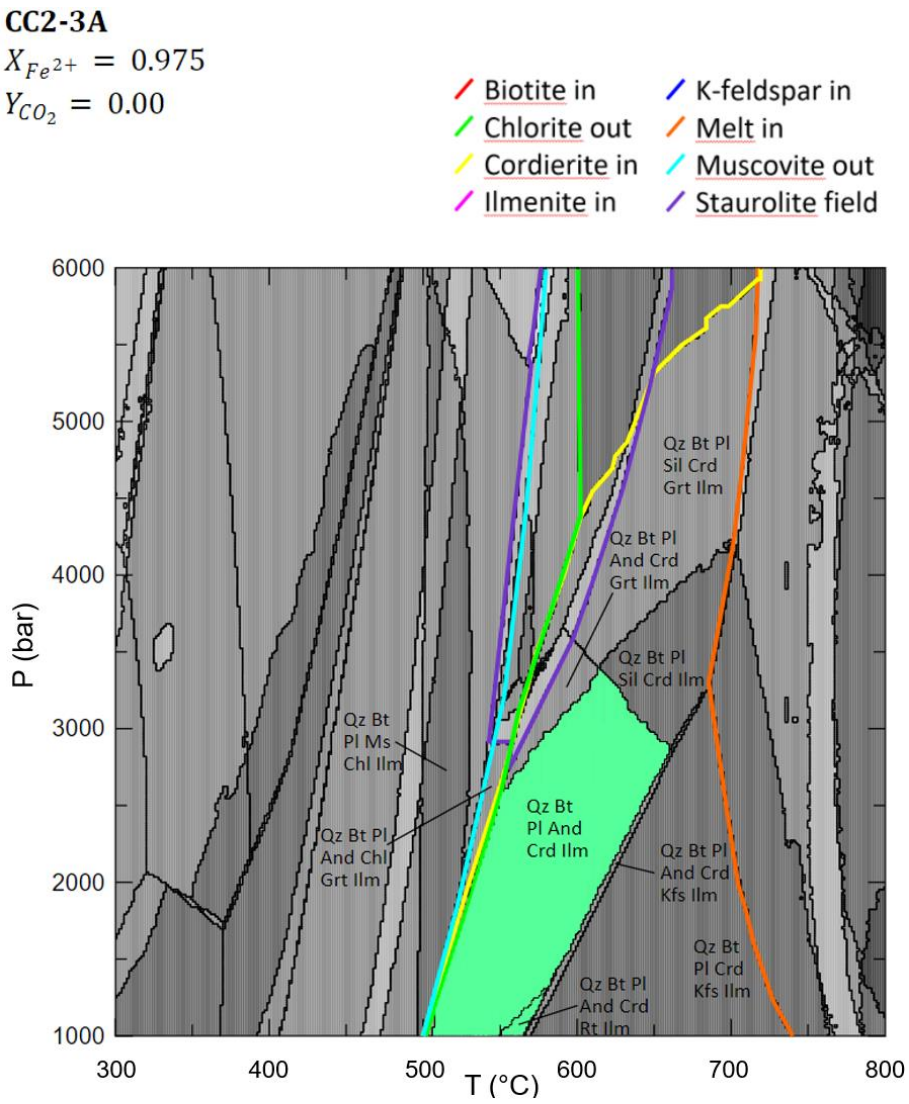

Figure 30: Pseudosection for CC2-3A of the andalusite–cordierite zone

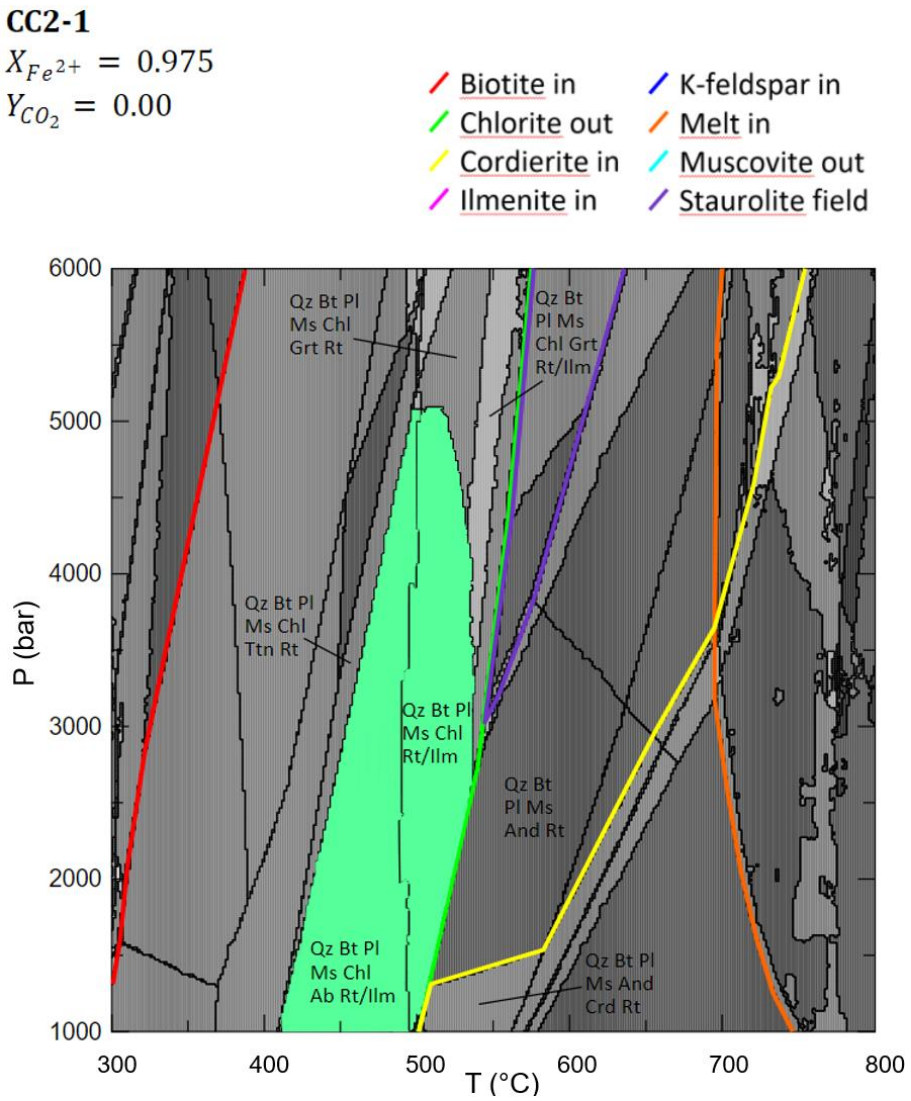

Figure 31: Pseudosection for CC2-1 of the biotite zone

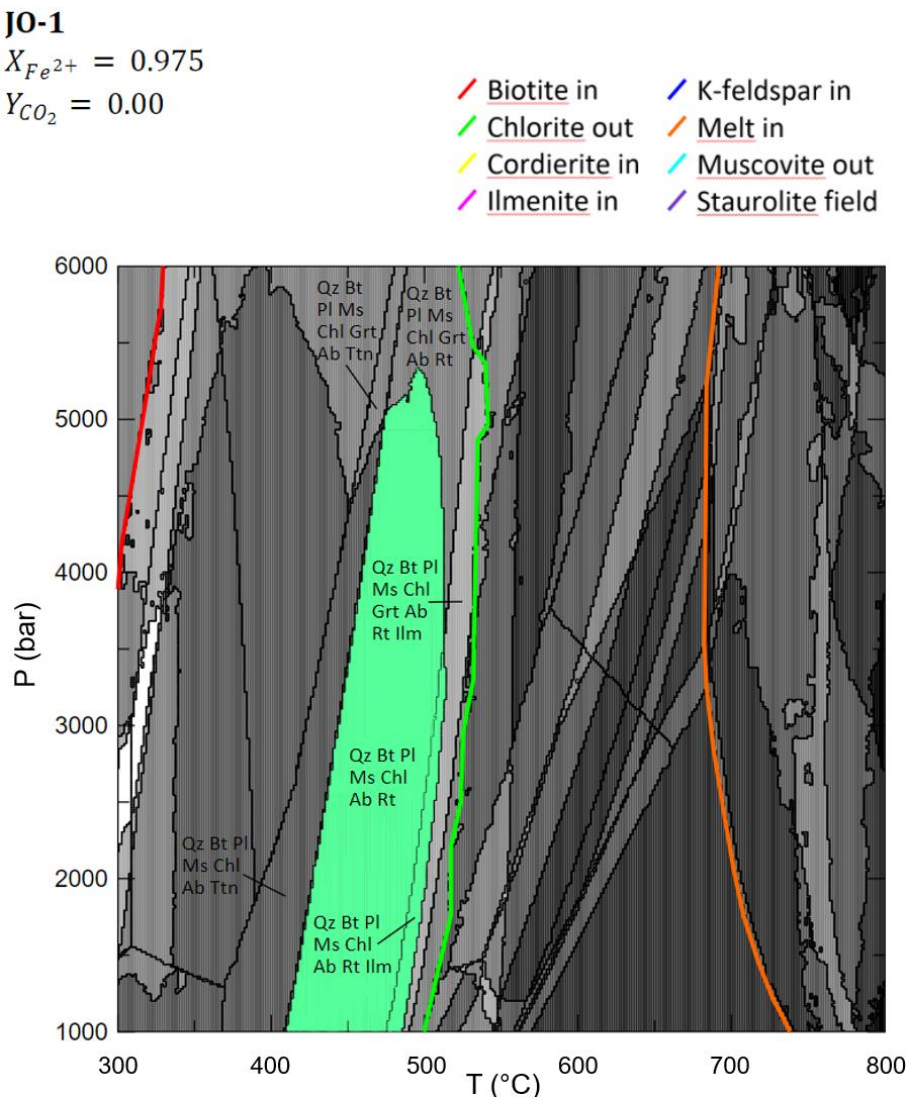

Figure 32: Pseudosection for JO-1 of the chlorite zone

Table 6: Overview of modelled P–T estimates per sample. Observed and modelled results do not correspond for minerals in red.

Sample	Metamorphic zone	Observed mineral paragenesis	Modelled mineral assemblage	P (bar)	T (°C)
CC95-11	sill–Kfs	Qz Bt Pl Ms Sil Kfs Ilm Rt	Qz Bt Pl Sil Kfs Rt	3000–5000	625–680
CC95-12	sill–Kfs	Qz Bt Pl Ms Sil Crd Ilm	Qz Bt Pl Sil Crd Rt Ilm	3500–4500	600–700
CC97-9	sill–Kfs / sill–ms	Qz Bt Pl Ms Sil Opq	Qz Bt Pl Ms Sil Rt	3250–5500	600–700
CC95-20	sill–ms	Qz Bt Fsp Grt Opq	Qz Bt Pl Grt Ilm	4500–6000	650–750
CC95-X-1	and–crd	Qz Bt Pl Ms And Opq	Qz Bt Pl Ms And Rt	1500–3750	510–625
CC2-3A	and–crd	Qz Bt Pl Ms And Crd Opq	Qz Bt Pl And Crd Ilm	1000–3500	500–650
CC2-1	biotite	Qz Bt Fsp Ms Chl Opq	Qz Bt Pl Ms Chl (Ab) Rt/Ilm	1000–5000	400–525
JO-1	chlorite	Qz (Bt) Pl Ms Chl Opq	Qz Bt Pl Ms Chl Ab Rt (Ilm)	1000–5250	400–500

Table 7: Mineral proportions per sample. Comparison between SEM-AM obtained composition and Perple_X modelled composition. Values are in wt%

CC97-9	**Qz**	**Bt**	**Pl**	**Ms**	**Sil [2]**	**Rt**	**Tur**	**Ap**
AM [1]	27.5	30.9	12.1	23.4	2.4	-	0.7	0.6
Perple_X	25.8	34.4	17.7	17.0	4.9	0.2	0	0
CC95-12	**Qz**	**Bt**	**Pl**	**Ms**	**Sil**	**Crd**	**Rt**	**Ilm**
AM	21.7	33.3	27.7	3.0	0.9	9.3	-	0.3
Perple_X	20.6	31.5	31.7	0	4.3	11.3	0.3	0.3
CC95-11	**Qz**	**Bt**	**Pl**	**Ms**	**Sil**	**Kfs**	**Rt**	**Ilm**
AM	41.3	15.6	27.4	3.0	2.2	8.7	-	0.2
Perple_X	38.2	17.9	30.1	0	6.0	7.15	0.6	0

[1] CC97-9 AM mineral composition from Van Melick (2021)
[2] AM Sil value also contains andalusite remnant

5. Discussion

5.1 SEM workflow

Comparing SEM-AM and XRF obtained bulk rock compositions shows that there are no major differences in the oxide proportions. The SEM-AM technique is based on a 2D surface which is used as a representative surface of the entire rock sample. This technique offers the possibility to analyse a specific part of the sample separately. For instance, in rock samples with strong compositional banding, the different bands can be analysed and interpreted individually. If the mineral assemblage and its spatial distribution is known, SEM-AM analysis can be useful for more precise analysis.

XRF analysis uses a 3D sample which is analysed as a whole. This analysis is more useful if the mineral assemblage is not entirely known or unknown. Under these circumstances, there is less chance to obtain wrong data with XRF analysis. Another advantage of this analysis is that XRF analysis has a higher throughput than SEM-AM: more samples can be processed and in a short time, meaning that data is acquired faster.

5.2 REE diagrams

The REE diagrams are all very similar and follow the same pattern for all four samples (Fig. 23). The relative enrichment in LREE compared to chondrite indicates that partial melting conditions were not reached in these rocks, as LREE would have entered the melt and left the system, which would cause a relative depletion of these elements compared to chondrite. The REE patterns indicate a small negative europium anomaly, even though plagioclase is present in all plotted samples. In general, rocks that contain plagioclase develop a strong positive europium anomaly, as Eu^{2+} is relatively compatible and tends to replace Ca^{2+} in plagioclase, while all other REE have approximately the same degree of incompatibility with respect to plagioclase (Philpotts & Ague, 2009). Other phases do not show a significant anomaly in europium. However, REE abundances mainly reflect the composition of the source-rocks. The fact that plagioclase is still quite abundant in all samples despite the lack of a positive Eu anomaly, indicates that plagioclase mainly has a metamorphic origin.

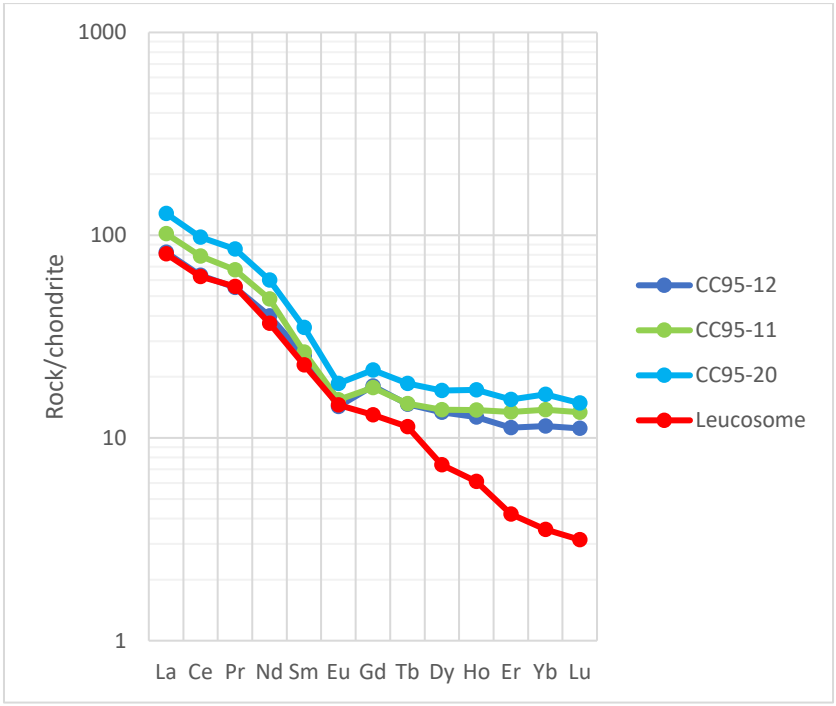

Figure 33: Chondrite normalised (Nakamura, 1974) REE diagram plots of high metamorphic grade samples compared with a plot of an average leucosome from Druguet et al. (2014).

The REE plots of the highest grade samples can also be compared with the REE plot of the average leucosome from Druguet et al. (2014) originating from the Tudela migmatitic complex (Fig. 33). The LREE of the high-grade samples follow the same pattern as the leucosome. The leucosome is relatively depleted in HREE compared to the samples of this study. As leucosomes contain the most felsic part of the original rocks, LREE tend to enter the leucosome whereas HREE tend to remain in the melanosome. This makes the leucosome extremely depleted in HREE compared to chondrite. The high-grade samples of this study contain similar LREE amounts, but are enriched in HREE compared with the leucosome, which is another indication that no partial melting took place in the high-grade samples.

5.3 Determining deformation temperature

The irregular and lobate grain boundaries observed in the quartzites samples, combined with the large grain sizes measured, would suggest that grain boundary migration occurred as recrystallisation mechanism. The smaller grain found along grain boundaries in both samples could be new grains formed from subgrains from subgrain rotation. The presence of these new grains suggests that they grew after the formation of the large irregular grains. If the small grains were older than the large grains, it is likely that they would have disappeared into the large grains as a result of grain boundary migration. Due to that, at least two phases of deformation took place in the quartzites, the first being dominated by grain boundary migrations, and the second by subgrain rotation.

Grain boundary migration is the dominant recrystallisation mechanism only during high temperature deformation. This implies that the deformation temperature was at least 500–600°C or more (Fossen, 2016). A diagram of Stipp et al. (2002a, 2002b) plots recrystallised grain size against temperature based on the different recrystallisation mechanisms. This gives a more precise indication of the deformation temperature in the quartzites. The grain sizes measured along the short axes of the large grains (752 and 680 µm for FR1 and FR3 respectively) indicate a minimum deformation temperature of approximately 565–570 ± 30°C for both samples (Fig. 34). As the diagram is limited to grain sizes up to 1000 µm, a maximum deformation temperature cannot be determined. However, based on the grain sizes of several thousands of microns along the long axes of the large grains, the maximum deformation temperature is likely to be higher than 570°C. Plotting the grain sizes of the small new grains gives deformation temperatures of ~530 ± 30°C and ~440 ± 30°C for FR1 and FR3 respectively during subgrain rotation.

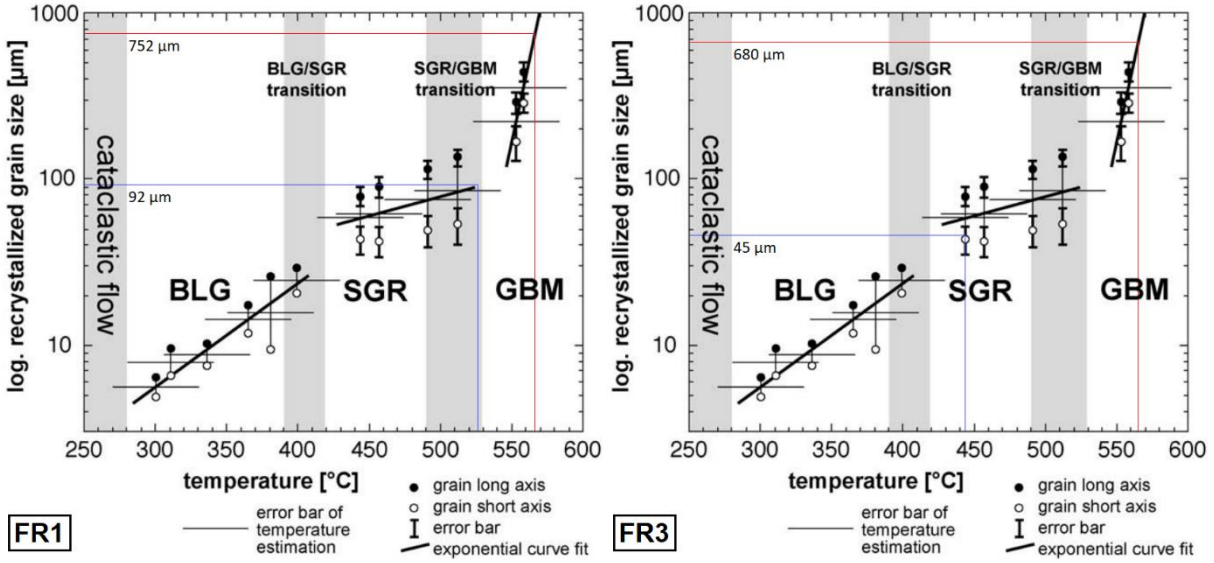

Figure 34: Diagram of recrystallized grain size versus temperature (Stipp et al., 2002a, 2002b) for FR1 (left) and FR3 (right) giving a minimum GBM deformation temperature of 565–700 ± 30°C (red lines). The blue lines indicate deformation temperatures of ~530 ± 30°C (FR1) and ~440 ± 30°C (FR3) for the small grains. BLG = bulging; SGR = subgrain rotation; GBM = grain boundary migration.

The temperature difference can be explained considering the location of the samples. Sample FR3 is located inside a shear zone, while FR1 is further away from one. Subgrain rotation could have taken place during shearing in D_3, which took place at greenschist facies conditions under retrograde conditions. As sample FR3 is located within a shear zone, the sample may have undergone deformation for a longer period of time and therefore under lower temperature conditions compared to FR1.

5.4 Constraining metamorphic conditions of the metamorphic zones

According to the Perple_X pseudosections diagrams, pressure and temperature increased from approximately 1.0–2.0 kbar and 450°C in the low-grade samples up to 4.0–5.0 kbar and almost 700°C in the highest-grade samples. Despite their different mineral assemblages, the stable fields of the semi-pelite and the pelite (CC95-11 and CC95-12 respectively) from the sillimanite–K-feldspar subzone both plot within a pressure and temperature range of 3.8–4.3 kbar and 650–680°C, reaching upper amphibolite facies. The difference in mineral assemblage can be explained by looking at their bulk rock compositions (Table 5). Semi-pelite CC95-11 contains a significantly larger amount of silica, but much less iron and magnesium compared with pelite CC95-12. This difference can be plotted in an AKF diagram (Fig. 35), originally introduced by Eskola (1920), in which $A = Al_2O_3$, $K = K_2O$ and $F = FeO + Fe_2O_3 + MgO$ assuming a silica saturated system. This ternary diagram shows the stable mineral assemblage Sil + Bt + Kfs for CC95-11 and Sil + Bt + Crd for CC95-12. The bulk rock compositions of both samples, based on mole proportions, plot in their respective triangle, meaning that the difference in bulk rock composition can be a reason why different mineral assemblages are stable at similar P–T conditions.

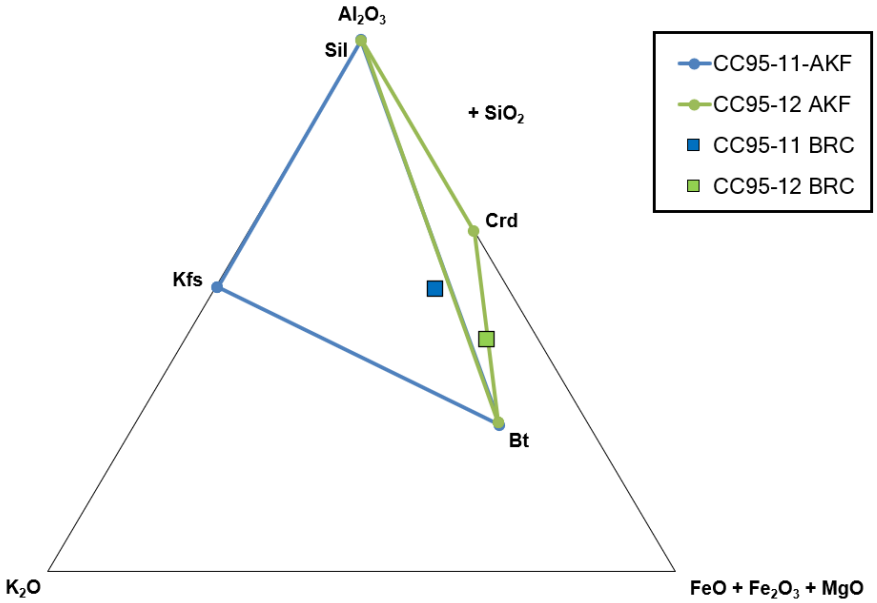

Figure 35: AKF diagram showing the stable mineral assemblages of CC95-11 and CC95-12 with their respective bulk rock composition. Diagram modelled with TernPlot (Marshall, 1996)

The two samples from the sillimanite–muscovite zone (CC97-9 and CC95-20) match less well with each other in terms of pressure and temperature estimates. The maximum modelled pressure of 6.0 kbar for sample CC95-20 is significantly higher compared to any of the other samples. A small area with a range of 4.9–5.5 kbar and 665–690°C overlaps with the P–T estimates of CC97-9. Even though sample CC95-20 originates from the sillimanite–muscovite zone, no sillimanite or muscovite was found using optical microscopy. If sillimanite was overlooked but is actually present in the sample, its predicted P–T conditions would shift towards 3.75–5.7 kbar and 600–660°C. This would better match with the P–T conditions of sample CC97-9 at 4.1–4.9 kbar and 625–655°C. This would remove CC95-20 as an outlier and plot it more on the increasing metamorphic gradient towards the sillimanite–K-feldspar subzone. The P–T estimates for the sillimanite zone of Reche & Martínez (Reche & Martínez, 1996) of 2.4–4.7

kbar and 560–670°C roughly correspond with the Perple_X based conditions. The Perple_X modelling results mainly correspond with the upper limit temperature estimate of 670°C of Reche & Martínez (1996), which was determined using thermobarometric calculations.

In the andalusite–cordierite zone, the two samples CC95-X and CC2-3A have overlapping P–T conditions from 1.5–3.2 kbar and 510–625°C, which represents lower to middle amphibolite facies. This temperature range corresponds with the estimates by Barnolas et al. (1996), who yielded a temperature of 600°C for the andalusite–cordierite zone, but their estimated pressure of 4.3 kbar is significantly higher. However, the estimate of Barnolas et al. (1996) was yielded in the northern part of the andalusite–cordierite zone, whereas the samples of this study come from the central part of the metamorphic zone. Given the fact that the metamorphic grade increases in northern direction, higher P–T conditions can be expected at the northern boundary of a metamorphic zone compared with its respective central part.

Samples from the biotite (CC2-1) and the chlorite (JO-1) zones show a temperature range of 400–525°C and 400–500°C respectively, which implies upper greenschist facies. As these ranges are overlapping each other, it is difficult to estimate the temperature at the transition from the chlorite zone to the biotite zone. Furthermore, both zones plot in a wide pressure range. As the metamorphic grade increases in both pressure and temperature from one zone to the next, it can be assumed that pressure in the chlorite and biotite zones was similar or lower than in the succeeding andalusite–cordierite zone. This would constrain the pressure range to 1.0–3.2 kbar. This is further constrained by the isograd where chlorite leaves the system and where andalusite and/or cordierite enter the system. Comparing Fig. 30 and 31 shows that the pressure in the biotite could have reached a maximum of 2.5 kbar, further constraining the pressure of the chlorite and biotite zones to 1.0–2.5 kbar. Table 8 gives an overview of all constrained P–T estimates per metamorphic zone.

The Perple_X pseudosection of JO-1 (chlorite zone) shows that biotite is stable at any temperature. In this study, biotite may be present in the sample, but the matrix is too fine grained to recognise biotite properly with optical microscopy. In the literature on the other hand, no biotite was reported to be present in the chlorite zone (Druguet, 2001; Guitard et al., 1995). This should be studied in more detail.

Table 8: Constrained P–T estimates per metamorphic zone based on Perple_X modelling.

Metamorphic zone	Perple_X constrained conditions		Literature conditions	
	P (kbar)	T (°C)	P (kbar)	T (°C)
sillimanite–K-feldspar	3.8–4.3	650–680		
sillimanite–muscovite	4.9–5.5	665–690	2.4–4.7	560–670
	4.1–4.9 [1]	625–655 [1]		
andalusite–cordierite	1.5–3.5	510–625	4.3	600
biotite	1.0–2.5	400–525		450
chlorite	1.0–2.5	400–500		

[1] If CC95-20 contains sillimanite

Determining a metamorphic field gradient of the entire area over a horizontal distance of 8.2 km from the chlorite zone (400–500°C) up to the migmatite zone (at least 680°C) would give a gradient range of only 22–34°C/km. However, the chlorite zone covers the largest area and temperature only starts increasing significantly from the andalusite–cordierite zone onwards. Over a distance of only 2.75 km, from the andalusite–cordierite zone till the migmatite zone, temperature increases from 510°C to 680°C. This results in a much higher metamorphic field gradient of at least 62°C/km. However, at the location of the sillimanite–K-feldspar samples where the highest temperature was modelled, it is unknown how close they were located to the migmatites. It is possible that the modelled temperature is not the maximum temperature of this zone, which would increase the metamorphic field gradient. This would agree with the REE diagrams, as they do not show any sign of partial melting of the sample.

The calculated metamorphic field gradient of 62°C/km is lower than the 80°C/km gradient reported by Druguet (2001) and also below the average metamorphic gradient for several massifs in the NE Pyrenees estimated at 75, 70 and 65°C by Barnolas et al. (1996), Zwart (1986) and Guitard et al. (1995), respectively. Calculating the gradient with the maximum temperature of only sample CC95-12 (700°C)

and of deviating sample CC95-20 (750°C) would give a metamorphic gradient of 69°C/km and 87°C/km respectively. The latter result is less reliable given the fact that this sample is located further away from the migmatite zone. In order to agree with the metamorphic field gradient of Druguet (2001), a temperature of at least 730°C is required as a maximum temperature of the sillimanite–K-feldspar subzone, on the transition to the migmatite zone. Such temperatures have not been reported in Cap de Creus, and based on this study, the metamorphic field gradient of Druguet (2001) seems unlikely.

A geothermal gradient for the sillimanite–K-feldspar subzone can be estimated by converting pressure to depth (d) according to $P = \rho \times g \times d$. For a pressure of 3.8–4.3, this would result in a depth of 14.3–16.2 km. A temperature range of 650–680°C would then give a geothermal gradient of 41.8–45.3°C/km.

5.5 Mineral reactions in the high-grade metamorphic zones

5.5.1 Sample CC95-11

Druguet (1997) stated that one of the K-feldspar forming mineral reactions in Cap de Creus is a dehydration reaction in which muscovite reacts with quartz to forms K-feldspar, sillimanite and H_2O. That reaction is as follows:

$$KAl_2AlSi_3O_{10}(OH)_2 + SiO_2 = KAlSi_3O_8 + Al_2SiO_5 + H_2O \quad (1)$$

This reaction would imply that sillimanite and K-feldspar occur in contact with each other in the sample. However, the large sillimanite nodules in sample CC95-11 are fully enclosed by a rim of muscovite and quartz. K-feldspar does not occur close to the sillimanite nodule (Fig. 36). The smaller nodules in the sample are closer to K-feldspar crystals, but these nodules also show a rim of muscovite and quartz, separating the sillimanite nodules from K-feldspar. Therefore reaction (1) suggested by Druguet (1997) could not have taken place to form the sillimanite nodules.

Another possibility could be that the sillimanite nodules are pseudomorphs that have replaced pre-existing andalusite. This should be studied in more detail in the future.

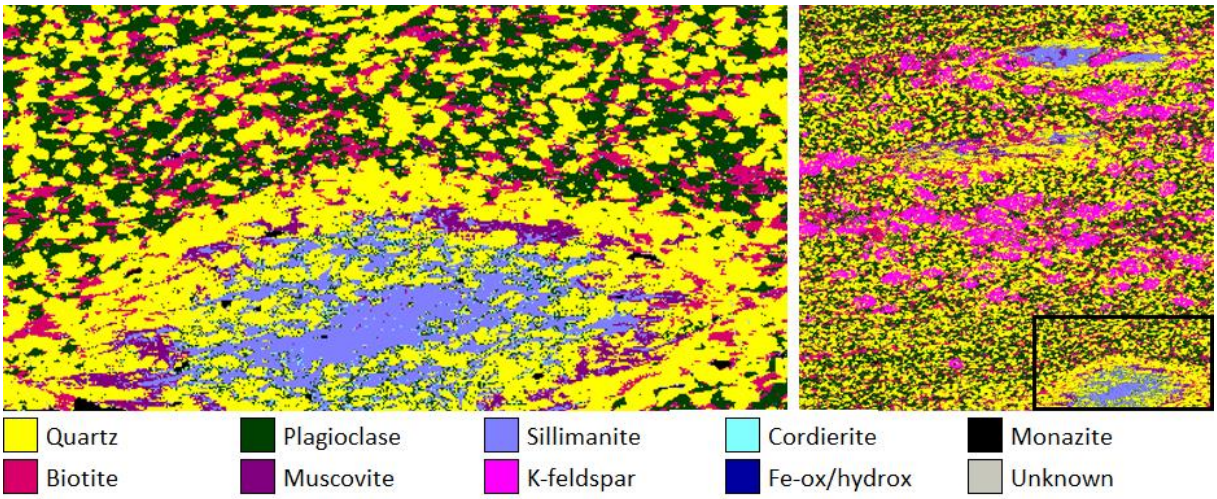

Figure 36: Zoomed SEM image of CC95-11 showing a large sillimanite nodule fully enclosed by muscovite and quartz. Note that there is no K-feldspar near the nodule. Black rectangle indicates location on the full SEM map.

The muscovite found among quartz, feldspar and biotite grains seems to be a second but stable phase of muscovite. Based on the euhedral shapes of these muscovite grains and the fact that they crosscut other minerals, this muscovite could have formed under retrograde metamorphic conditions. One possibility is that the prograde dehydration reaction (1) took place as a retrograde hydration reaction. The activation of shear zones during D_3 could have introduced water into the system again. Again

however, K-feldspar and sillimanite would have to react together to form muscovite, but these phases are not in contact with each other. Moreover, this retrograde reaction would also suggest that the newly grown muscovite is found with the K-feldspar and the sillimanite, which is not the case. Another possibility would be that a certain ionic exchange reaction takes place thanks to the influx of certain cations that allows muscovite to grow.

According to the Perple_X pseudosection diagram of this sample, a growth of retrograde muscovite would imply a decrease in temperature, as muscovite becomes stable below 650°C at a pressure of 4.0 kbar. However, this would then happen at the expense of K-feldspar, which is not stable anymore below that temperature. There is no clear evidence of K-feldspar being unstable in this sample.

5.5.2 Sample CC95-12

Sample CC95-12 is interesting because it bears two types of sillimanite that coexist with each other. Fibrolite, the main type of sillimanite in Cap de Creus, is reported to form as an alteration product of unstable andalusite (Druguet, 1997). This alteration is not clearly visible in this sample, as there is no sign of any unstable andalusite in contact with the fibrolite. The second type of sillimanite, prismatic sillimanite, is associated with another process. Druguet & Hutton (1998) mentioned prismatic sillimanite to be present in Cap de Creus and associated it with the relative timing of migmatite formation. She states that the more pelitic layers progressively become migmatites as the D_2 strain and transposition increase towards the north. Tight folds and a penetrative S_2 foliation develop and biotite wraps around cordierite porphyroblasts in a preferred orientation. New prismatic sillimanite then grows parallel to that fabric. Then, by moving northwards into the migmatite zone, quartz veins on the margins of the pelitic layers are replaced by quartzofeldspathic veins or migmatitic leucosomes consisting of quartz, plagioclase ± K-feldspar ± sillimanite ± almandine. These leucosomes are then surrounded by mafic selvages mainly consisting of biotite with or without sillimanite, cordierite and almandine (Druguet & Hutton, 1998). The SEM-AM false colour map (Fig. 20) indeed shows that cordierite is mainly surrounded by biotite and that prismatic sillimanite has grown against or within the cordierite. As the prismatic sillimanite sometimes overgrows the cordierite, it seems that it has grown as a new and later phase. If this sillimanite growth is related to the initiation of migmatite formation, this process is likely to have happened at high temperatures close to the solidus (~680–700°C). A possible mineral reaction that could have formed prismatic sillimanite is as follows:

$$2\,Ms + 3\,Crd = 2\,Bt + 8\,Sil + 7\,Qz \qquad (2)$$

The zoomed SEM image in Fig. 37 shows that these minerals are in contact with each other, and that sillimanite has overgrown other phases. This reaction (2) is reported by Pattison et al. (2002), in which H_2O is added as a reaction product if cordierite contains water.

Prismatic sillimanite is also reported in the Canigou massif in the northeastern Pyrenees. Prismatic sillimanite has grown there in a sillimanite metamorphic zone as a pseudomorph of andalusite. Moreover, prismatic sillimanite was also found at the boundary between the andalusite and sillimanite zone of the Canigou massif (Gibson & Bickle, 1994). In other massifs including Cap de Creus, fibrolite is the type of sillimanite that appears first.

Retrograde muscovite is also found in this sample, overgrowing mainly biotite grains. It is not known what kind of reaction formed this secondary muscovite. Reversing reaction (2) does not seem likely, as most retrograde muscovite is not in contact with cordierite, but purely with biotite. Given the location of this sample in the northeastern part of the study area, it is possible that new prismatic sillimanite grew at peak metamorphism during D_2. Migmatitic conditions were however not reached, and during D_3, muscovite grew under retrograde metamorphic conditions. According to the Perple_X pseudosection, this retrograde muscovite could only have formed once temperature dropped below 575°C, provided that pressure remained constant.

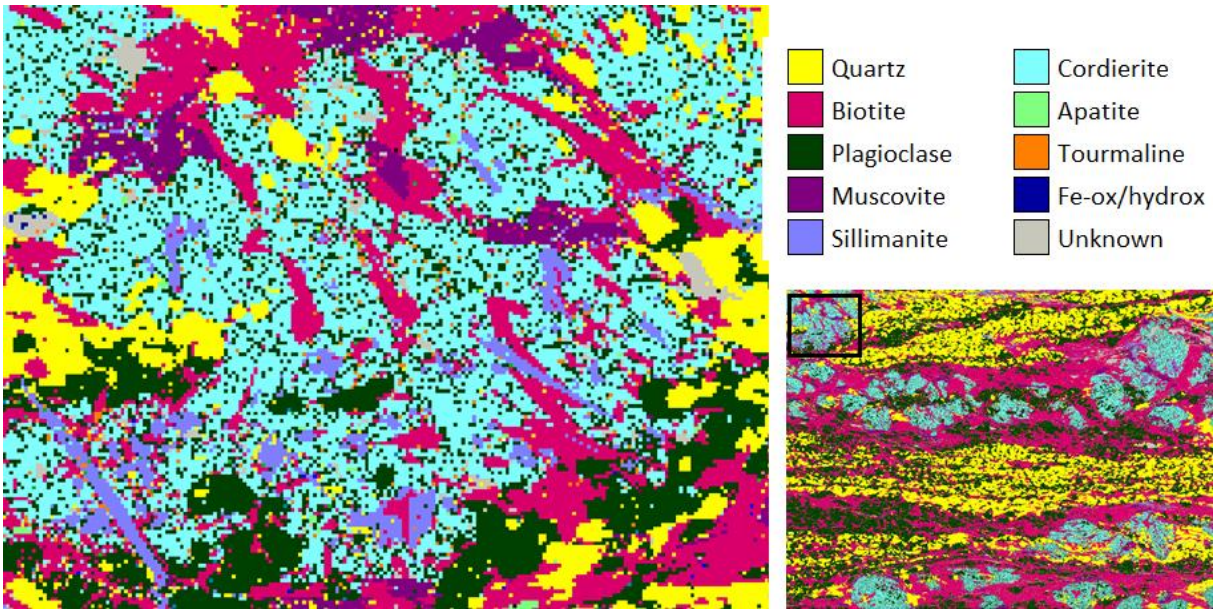

Figure 37: Zoomed SEM image of CC95-12 showing prismatic sillimanite in contact with cordierite and biotite. Black rectangle indicates location on the full SEM map.

5.5.3 Sample CC97-9

Sample CC97-9 is of particular interest as it contains fibrolitic sillimanite throughout the sample, but also contains an andalusite remnant. This sample has recorded the reaction from andalusite to sillimanite, without the andalusite being completely consumed. The andalusite remnant and the fibrolite are not spatially related with each other, as the remnant is completely surrounded by a muscovite aggregate, while the sillimanite mainly occurs among biotite. It is therefore unlikely that a polymorphic transformation from andalusite into sillimanite took place as a result of prograde metamorphism. Moreover, Carmichael (1969) proposed that aluminium is relatively immobile during metamorphic reactions, meaning that aluminium would not be transferred through the system. Applied on the metamorphic reaction from kyanite to sillimanite, he proposed that three ionic exchange reactions take place in which aluminium remains in position, while other components are transferred through the system by the pore fluid. The reactions can therefore take place in different locations: (3.1) at kyanite grains; (3.2) at biotite grains; and (3.3) where muscovite and albite are in contact:

$$3\,Ky + 3\,Qz + 2K^+ + 3H_2O \rightleftharpoons 2\,\mathrm{Ms} + 2\mathrm{H}^+ \tag{3.1}$$

$$Bt + Na^+ + 6H^+ \rightleftharpoons \mathrm{Ab} + \mathrm{K}^+ + 3(Mg,Fe)^{2+} + 4H_2O \tag{3.2}$$

$$2\,Ms + Ab + 3(Mg,Fe)^{2+} + H_2O \rightleftharpoons \mathrm{Bt} + 3\,\mathrm{Sil} + 3\,\mathrm{Qz} + \mathrm{K}^+ + Na^+ + 4H^+ \tag{3.3}$$

Summarised this would be a reaction from kyanite to sillimanite.

Allowing this principle on andalusite instead of kyanite for sample CC97-9 would give the following:

$$3\,And + 3\,Qz + 2K^+ + 3H_2O \rightleftharpoons 2\,\mathrm{Ms} + 2\mathrm{H}^+ \tag{4.1}$$

$$Bt + Na^+ + 6H^+ \rightleftharpoons \mathrm{Ab} + \mathrm{K}^+ + 3(Mg,Fe)^{2+} + 4H_2O \tag{4.2}$$

$$2\,Ms + Ab + 3(Mg,Fe)^{2+} + H_2O \rightleftharpoons \mathrm{Bt} + 3\,\mathrm{Sil} + 3\,\mathrm{Qz} + \mathrm{K}^+ + Na^+ + 4H^+ \tag{4.3}$$

Andalusite reacted with quartz and potassium cations to form muscovite. As the andalusite relic is fully enclosed by muscovite, the system could have locally run out of quartz which stopped the reaction, leaving the andalusite remnant behind. As can be seen in the SEM-AM false colour map (Fig. 21),

plagioclase is spatially associated with biotite throughout the system, meaning that the second (4.2) reaction could also have occurred. The third (4.3) reaction is also plausible, as muscovite, plagioclase, biotite and sillimanite all occur in close proximity.

If the first ionic exchange reaction (3.1; 4.1) can develop muscovite rims on both kyanite and andalusite, this reaction should theoretically also be able to develop muscovite rims on sillimanite, as sillimanite is just another polymorph. However, muscovite rims are not found on the sillimanite. A possible explanation for this could be that the first ionic exchange reaction took place and ended before P–T conditions entered the sillimanite stability field. This would imply that the first reaction took place under different circumstances, such as a lower temperature, a higher humidity or an influx of potassium (Green, 1963).

5.6 Combining metamorphism with deformation

Based on all observations and interpretations, a metamorphic history can be established. A metamorphic field gradient and several potential P–T paths were drawn in Fig. 38 and 39 respectively.

D_1 was the first phase of deformation that affected the metapelites in the Cap de Creus peninsula. This deformation phase created the $S_{0/1}$ bedding-parallel schistosity that is mainly visible in the lower grade zones due to the alignment of phyllosilicates.

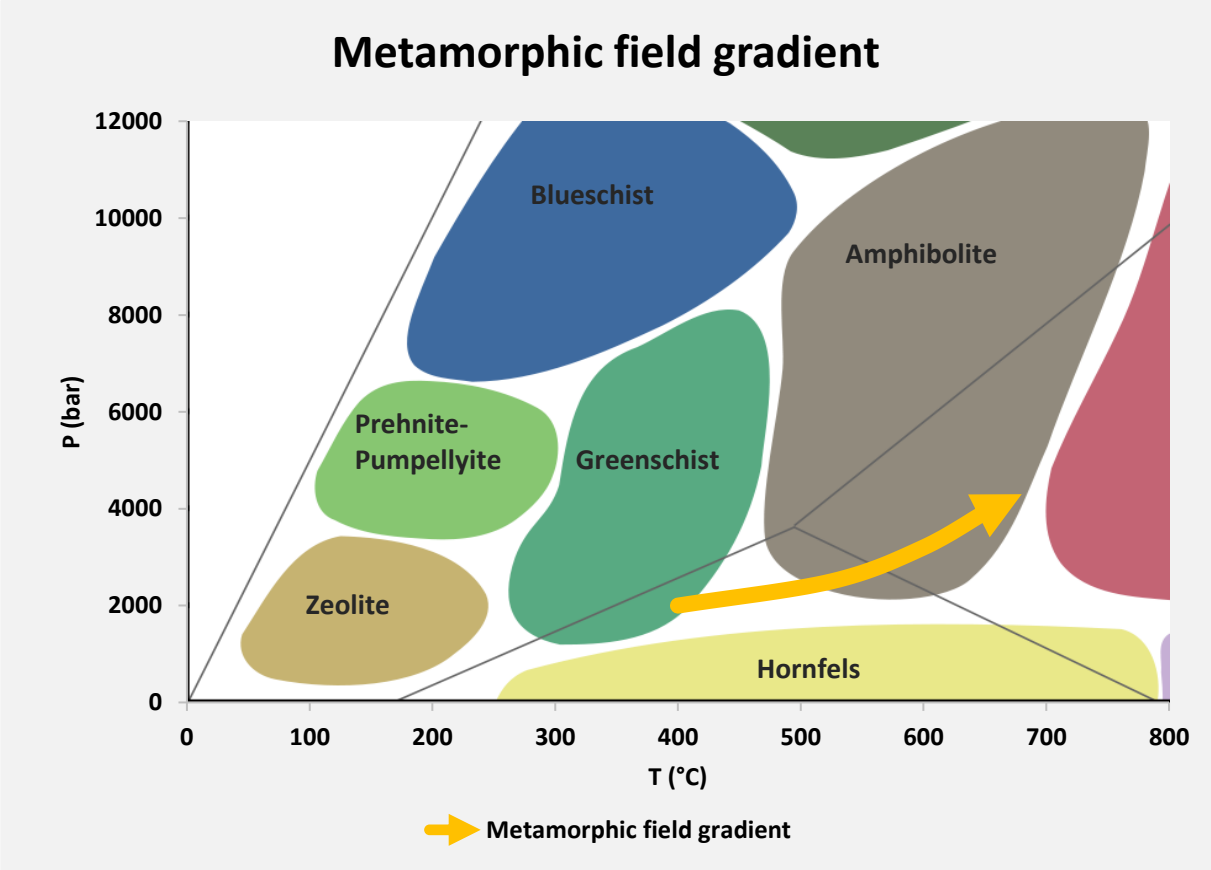

Figure 38: Metamorphic field gradient based on peak metamorphic conditions of each metamorphic zone.

The second deformation event (D_2) created crenulation cleavages, which is also visible in the lowest grade zones. The chlorite and biotite zone samples show these crenulations in the chlorite and quartz mixture. In the biotite zone, biotite started growing over the schistosity and this zone reached a maximum peak metamorphism of 2.5 kbar and 525°C (Fig. 38). In the early stages of D_2, cordierite and andalusite started growing in the andalusite–cordierite zone on top of the pre-existing matrix, forming

large porphyroblasts. In this zone, peak metamorphism was reached at a maximum of 3.2 kbar and 600–625°C (Fig. 38).

Andalusite also grew in the sillimanite–muscovite zone during early D_2, before reaching peak metamorphic conditions. This andalusite possibly started to react with quartz to form muscovite, according to the ionic exchange reaction (4.1). The reaction stopped when the system was locally depleted in quartz, leaving an andalusite remnant enclosed by a muscovite aggregate. Near peak metamorphic conditions, the second and third ionic exchange reactions (4.2; 4.3) took place to form fibrolite and new biotite. These reactions took place at a maximum pressure and temperature of 5.5 kbar and 690°C, although these pressure and temperature estimates are likely to be too high. More likely conditions would be maximums of approximately 4.0 kbar and 650°C, which would be more in line with the even higher-grade sillimanite–K-feldspar subzone.

In the sillimanite–K-feldspar subzone, temperature exceeded 655°C (Fig. 39), indicated by the presence of unstable muscovite. In the cordierite bearing pelites in this metamorphic subzone, unstable muscovite reacted with cordierite to form new biotite and prismatic sillimanite (2). As this zone does not appear as a proper metamorphic zone, but rather as patches within the sillimanite–muscovite zone, it is unclear how these patches reached higher pressures and temperatures. Prismatic sillimanite in Cap de Creus is associated with the relative timing of migmatite formation (Druguet & Hutton, 1998), so local granitoids could have increased temperature conditions locally. As partial melting did not occur in the samples of this study, the prismatic sillimanite forming reaction (2) could have happened at high temperatures just below the solidus (680–700°C). Peak metamorphic conditions were reached at the end of D_2 with a maximum of 4.3 kbar and 680°C (Fig. 38).

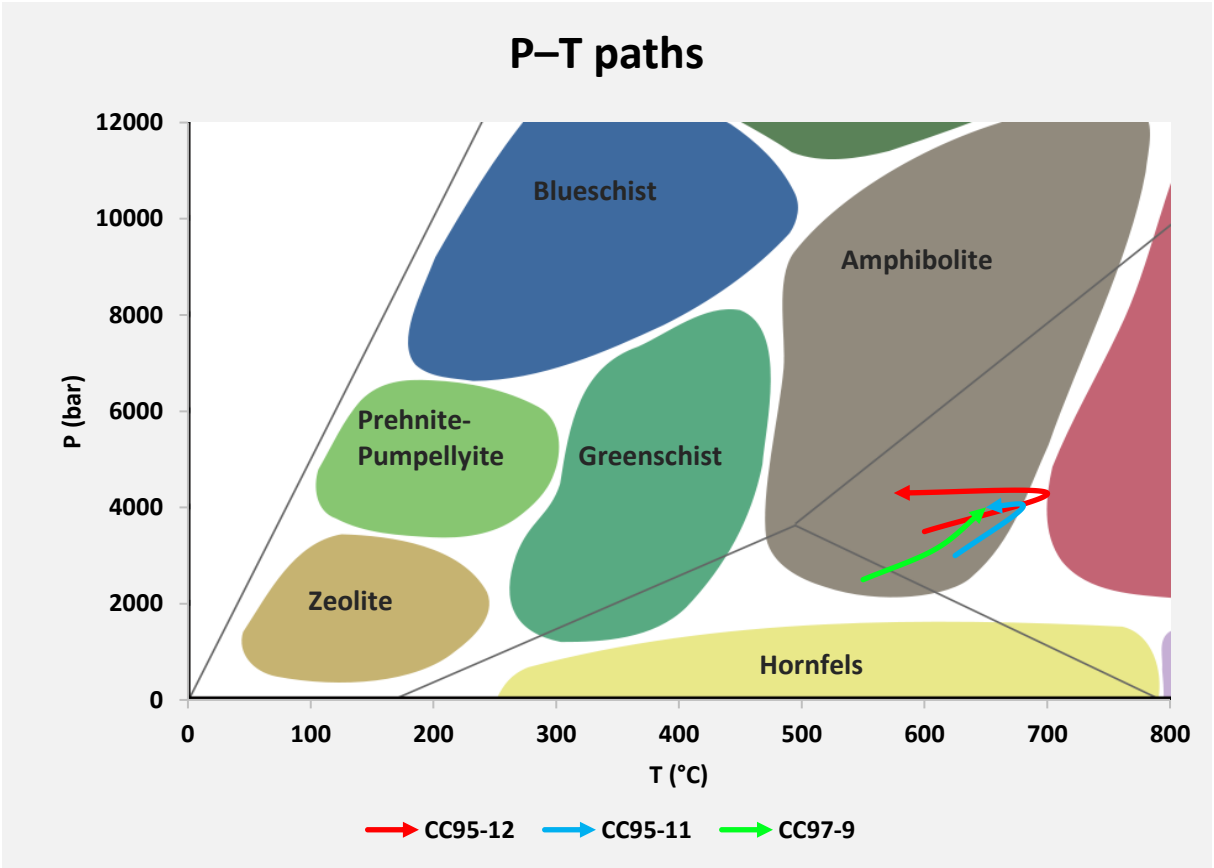

Figure 39: Potential P–T paths of the highest-grade samples. CC95-12 reached a maximum of 4.3 kbar and 700°C, before retrograding to at least 575°C. CC95-11 reached 4.0 kbar and 680°C before retrograding to at least 650°C. CC97-9 recorded prograde metamorphism from the andalusite stability field into the sillimanite stability field.

The quartzites underwent deformation temperatures of at least 565°C during D_2. Dominated by grain boundary migration, large irregular shaped quartz grains were able to form. However, based on the grain sizes of the quartzites and their locations with respect to the metamorphic zones, peak deformation temperatures in the quartzites were likely to be significantly higher.

After peak metamorphic conditions were reached, the system entered a phase of retrograde metamorphism. In the sillimanite–K-feldspar subzone, muscovite is the main retrograde metamorphic mineral. In semipelitic rocks, secondary muscovite could have grown when temperature dropped below 655°C at 4.0 kbar (Fig. 39). In pelitic rocks in this subzone, temperature must have dropped below at least 575°C at 4.0 kbar. As kyanite pseudomorphs of sillimanite and andalusite are sporadically found in the western domains of the peninsula (Druguet, 2001), temperature conditions may have decreased significantly faster than pressure conditions in order to pass through the kyanite stability field.

When the third and last deformation event (D_3) started, P–T conditions decreased towards greenschist facies conditions. This deformation event caused heterogeneous folding and shearing of the system. Shear zones mainly activated in the higher-grade metamorphic zones. Temperatures dropped to at least 440°C at which new quartz grain grew in the quartzites as a result of subgrain rotation.

5.7 Suggestions for future work

Metamorphism in the high-grade zones reached upper amphibolite facies conditions before retrograding to lower temperatures and potentially lower pressures. This agrees with most of the studied samples. However, sample CC95-20 does not fit with this theory. The estimated P–T conditions with thermodynamic modelling indicate a higher peak temperature and a significantly higher pressure. It can be suggested that, unlike the other high-grade samples, this sample did not experience retrograde metamorphism, if retrograde metamorphism was limited to take place in the shear zones. Yet this sample is thought to originate from a shear zone, based on its known location (Fig. 5). Mineralogical data is lacking for this sample, so it would be interesting to research this sample in more detail using SEM-EDS automated mineralogy.

The question whether the northernmost metamorphic zones are mainly affected by regional metamorphism or by the presence of intruding granitoid bodies, is difficult to answer. Increased temperature estimates do suggest that granitoid bodies could have had an effect on these samples, but trace element data does not provide any evidence that magmatic heat reached the metapelites. This means that actual contact metamorphism did not take place in the highest-grade samples, but the heat of the granitoid intrusions could have locally increased the temperature in the sillimanite–K-feldspar subzone. In order to get a better insight in the role of the intrusion on the metamorphism, more data is required on other, potentially newly acquired samples from the sillimanite–K-feldspar and the sillimanite–muscovite zone near the migmatitic complexes. It would also be interesting to apply the research conducted here to rock samples from the migmatite zone, which would allow for comparison with the highest-grade metamorphic zones containing metapelites.

6. Conclusion

The Cap de Creus peninsula was affected by several phases of deformation and metamorphism. Different metamorphic zones underwent different intensities of metamorphism starting at 1.0–2.5 kbar and 400–500°C in the chlorite zone up to 3.8–4.3 kbar and 650–680°C in the sillimanite–K-feldspar subzone. From the andalusite–cordierite zone to the sillimanite–K-feldspar subzone, a high thermal gradient of at least 62°C/km was established. This gradient can potentially be higher as the highest-grade samples did not reach migmatitic conditions.

Trace element (REE) diagrams of the highest-grade samples suggest that no partial melting took place. This indicates that the sillimanite zone samples were not affected by the intruding granitoid bodies. The negative anomaly in europium indicates that plagioclase is mainly a metamorphic mineral and did not occur or barely occurred in the source rock.

The quartzite samples that originate from the sillimanite zone, are dominated by grain boundary migration. Based on the grain size of large grains along their short axes, this recrystallisation method implies a deformation temperature of at least 565–570°C. However, temperature was likely to be higher based on the grain sizes along the long axes. The quartzites underwent deformation again during D_3, at temperatures of 530°C and 440°C dominated by subgrain rotation. This can be linked to the activation of the shear zones.

The second deformation event occurred together with prograde and peak metamorphism. These events comprise the main part of the metamorphic history. Andalusite and cordierite grew during the early phases of D_2. The andalusite that grew in the sillimanite zone, could have indirectly reacted into sillimanite via three ionic exchange reactions: andalusite + quartz to muscovite; biotite to plagioclase; and muscovite + plagioclase to sillimanite + biotite. The first ionic exchange reaction may have occurred before the other two without overlapping in time.

Muscovite becomes unstable in the sillimanite–K-feldspar subzone and in pelitic rocks it could have reacted with cordierite to form new biotite and prismatic sillimanite. As prismatic sillimanite is related to the relative timing of migmatite formation, this reaction potentially happened by a local increase in temperature as a result of intruding granitoid bodies at the end of D_2. Peak metamorphic conditions were reached at a maximum of 4.3 kbar and 680°C.

D_3 was paired with shearing and folding and retrograde metamorphism. Temperatures in the sillimanite–K-feldspar subzone dropped below at least 655°C so that a retrograde phase of muscovite could form. This could have possibly formed in expense of K-feldspar by reversing the dehydration reaction, but K-feldspar does not show a clear sign of instability. As shear zone activity took place at greenschist conditions, temperature is likely to have dropped below 500°C.

References

Alfonso, P. (1996). *Aproximación a la petrogénesis de las pegmatitas del Cap de Creus* [Unpublished thesis]. Universitat de Barcelona.

Barnolas, A., Chiron, J. C., & Guérangé, B. (1996). *Synthèse géologique et géophysique des Pyrénées*. Orléans : Bureau de recherches géologiques et minières (BRGM) Orléans / Instituto Tecnológico Geominero de España (ITGE) Madrid.

Beaumont, C., Muñoz, J. A., Hamilton, J., & Fullsack, P. (2000). Factors controlling the Alpine evolution of the central Pyrenees inferred from a comparison of observations and geodynamical models. *Journal of Geophysical Research*, *105*(B4), 8121–8145.

Carmichael, D. M. (1969). On the Mechanism of Prograde Metamorphic Reactions in Quartz-Bearing Pelitic Rocks. *Contributions to Mineralogy and Petrology*, *20*, 244–267.

Carreras, J. (2001). Zooming on Northern Cap de Creus shear zones. *Journal of Structural Geology*, *23*(9), 1457–1486. https://doi.org/10.1016/S0191-8141(01)00011-6

Carreras, J., & Capella, I. (1994). Tectonic levels in the Palaeozoic basement of the Pyrenees: a review and a new interpretation. *Journal of Structural Geology*, *16*(11), 1509–1524. https://doi.org/10.1016/0191-8141(94)90029-9

Carreras, J., & Casas, J. M. (1987). On folding and shear zone-development: a mesoscale structual study on the transition between two different tectonic styles. *Tectonophysics*, *135*, 87–98.

Carreras, J., Cosgrove, J. W., & Druguet, E. (2013). Strain partitioning in banded and/or anisotropic rocks: Implications for inferring tectonic regimes. *Journal of Structural Geology*, *50*, 7–21. https://doi.org/10.1016/j.jsg.2012.12.003

Carreras, J., & Losantos, M. (1982). Geological setting of the Roses granodiorite (E-Pyrenees, Spain). *Acta Geológica Hispánica*, *17*(4), 211–217.

Choukroune, P., & Mattauer, M. (1978). Tectonique des plaques et Pyrénées : sur le fonctionnement de la faille transformante nord-pyrénéenne ; comparaisons avec des modèles actuels. *Bulletin de La Société Géologique de France*, *7*(5), 689–700.

Choukroune, P., Roure, F., Pinet, B., & ECORS Pyrenees Team. (1990). Main results of the ECORS Pyrenees profile. *Tectonophysics*, *173*(1–4), 411–423.

Connolly, J. A. D. (1990). Multivariable phase diagrams: An algorithm based on generalized thermodynamics. In *American Journal of Science* (Vol. 290, Issue 6, pp. 666–718).

Connolly, J. A. D. (2005). Computation of phase equilibria by linear programming: A tool for geodynamic modeling and its application to subduction zone decarbonation. *Earth and Planetary Science Letters*, *236*(1–2), 524–541.

Connolly, J. A. D. (2009). The geodynamic equation of state: What and how. *Geochemistry, Geophysics, Geosystems*, *10*(10), 1–19.

Connolly, J. A. D., & Petrini, K. (2002). An automated strategy for calculation of phase diagram sections and retrieval of rock properties as a function of physical conditions. *Journal of Metamorphic Geology*, *20*(7), 697–708.

Damm, K.-W., Harmon, R. S., Heppner, P.-M., & Dornsiepen, U. (1992). Stable isotope constraints on the origin of the Cabo de Creus garnet–tourmaline pegmatites, Massif des Alberes, Eastern Pyrenees, Spain. *Geological Journal*, *27*, 75–86.

Druguet, E. (1992). *Petrología del complex migmatític de l'àrea de la Punta dels Furallons (Cap de Creus)* [Unpublished Tesi de Llicenciatura]. Universitat de Barcelona.

Druguet, E. (1997). *The structure of the NE Cap de Creus peninsula. Relationships with metamorphism and magmatism* [Unpublished thesis]. Universitat Autònoma de Barcelona.

Druguet, E. (2001). Development of high thermal gradients by coeval transpression and magmatism during the Variscan orogeny: Insights from the Cap de Creus (Eastern Pyrenees). *Tectonophysics*, *332*(1–2), 275–293.

Druguet, E., Carreras, J., & Mezger, J. E. (2018). Discussion on "Middle Jurassic shear zones at Cap de Creus (eastern Pyrenees, Spain): a record of pre-drift extension of the Piemonte–Ligurian Ocean?" Journal of the Geological Society, London, 174, 289–300. *Journal of the Geological Society*, *175*, 187–188.

Druguet, E., Castro, A., Chichorro, M., Pereira, M. F., & Fernández, C. (2014). Zircon geochronology

of intrusive rocks from Cap de Creus, Eastern Pyrenees. *Geological Magazine*, *151*(6), 1095–1114.

Druguet, E., Enrique, P., & Galán, G. (1995). Tipología de los granitoides y rocas asociadas del complejo migmatítico de la Punta dels Farallons (Cap de Creus, Pirineo Oriental). *Geogaceta*, *18*, 199–202.

Druguet, E., & Hutton, D. H. W. (1998). Syntectonic anatexis and magmatism in a mid-crustal transpressional shear zone: an example from the Hercynian rocks of the eastern Pyrenees. *Journal of Structural Geology*, *20*(7), 905–916.

Druguet, E., Passchier, C. W., Carreras, J., Victor, P., & Den Brok, S. (1997). Analysis of a complex high-strain zone at Cap de Creus, Spain. *Tectonophysics*, *280*(1–2), 31–45.

Eskola, P. (1920). The Mineral Facies of Rocks. *Norsk Geologisk Tidsskrift*, *6*, 143–194.

Forshaw, J. B., & Pattison, D. R. M. (2021). Ferrous/ferric (Fe^{2+}/Fe^{3+}) partitioning among silicates in metapelites. *Contributions to Mineralogy and Petrology*, *176*(63), 1–26.

Fossen, H. (2016). *Structural Geology* (2nd ed.). Cambridge University Press.

Fuhrman, M. L., & Lindsley, D. H. (1988). Ternary-feldspar modeling and thermometry. *American Mineralogist*, *73*, 201–215.

Gibson, R. L., & Bickle, M. J. (1994). Thermobarometric constraints on the conditions of metamorphism in the Canigou massif, Pyrenees: implications for Hercynian geothermal gradients. *Journal of the Geological Society*, *151*(6), 987–997.

Green, J. C. (1963). High-Level Metamorphism Of Pelitic Rocks In Northern New Hampshire. *American Mineralogist*, *48*(9–10), 991–1023.

Griffin, W. L., Powell, W. J., Pearson, N. J., & O'Reilly, S. Y. (2008). GLITTER: Data reduction software for Laser Ablation ICP-MS. In P. Sylvester (Ed.), *Laser Ablation–ICP–MS in the Earth Sciences: Current practices and outstanding issues* (pp. 308–311).

Guitard, G., Vielzeuf, D., & Martínez, F. (1995). Métamorphisme Hercynien. In A. Barnolas, J. C. Chiron, & B. Guérangé (Eds.), *Synthèse géologique et géophysique des Pyrénées* (Vol. 1, pp. 501–584). Bureau de recherches géologiques et minières (BRGM).

Holland, T. J. B., & Powell, R. (1991). A Compensated-Redlich-Kwong (CORK) equation for volumes and fugacities of CO_2 and H_2O in the range 1 bar to 50 kbar and 100-1600°C. *Contributions to Mineralogy and Petrology*, *109*(2), 265–273.

Holland, T. J. B., & Powell, R. (1998). An internally consistent thermodynamic data set for phases of petrological interest. *Journal of Metamorphic Geology*, *16*(3), 309–343.

Holland, T. J. B., & Powell, R. (2001). Calculation of phase relations involving haplogranitic melts using an internally consistent thermodynamic dataset. *Journal of Petrology*, *42*(4), 673–683.

Holland, T. J. B., & Powell, R. (2011). An improved and extended internally consistent thermodynamic dataset for phases of petrological interest, involving a new equation of state for solids. *Journal of Metamorphic Geology*, *29*(3), 333–383.

Le Pichon, X., & Sibuet, J.-C. (1971). Western extension of boundary between European and Iberian plates during the Pyrenean orogeny. *Earth and Planetary Science Letters*, *12*, 83–88.

Marshall, D. (1996). TernPlot: An Excel spreadsheet for ternary diagrams. *Computers and Geosciences*, *22*(6), 697–699.

Mezger, J. E., Passchier, C. W., & Régnier, J.-L. (2004). Metastable staurolite–cordierite assemblage of the Bossòst dome: Late Variscan decompression and polyphase metamorphism in the Axial Zone of the central Pyrenees. *Comptes Rendus Geoscience*, *336*(9), 827–837.

Muñoz, J. A. (1992). Evolution of a continental collision belt: ECORS-Pyrenees crustal balanced cross-section. *Thrust Tectonics*, 235–246.

Nakamura, N. (1974). Determination of REE, Ba, Fe, Mg, Na and K in carbonaceous and ordinary chondrites. *Geochimica et Cosmochimica Acta*, *38*(5), 757–775. https://doi.org/10.1016/0016-7037(74)90149-5

Pattison, D. R. M., Spear, F. S., Debuhr, C. L., Cheney, J. T., & Guidotti, C. V. (2002). Thermodynamic modelling of the reaction muscovite + cordierite = Al_2SiO_5 + biotite + quartz + H_2O: constraints from natural assemblages and implications for the metapelitic petrogenetic grid. *Journal of Metamorphic Geology*, *20*, 99–118.

Philpotts, A. R., & Ague, J. J. (2009). *Principles of Igneous and Metamorphic Petrology* (2nd ed.). Cambridge University Press.

Reche, J., & Martínez, F. J. (1996). GPT: An Excel spreadsheet for thermobarometric calculations in metapelitic rocks. *Computers & Geosciences*, *22*(7), 775–784.

Roure, F., Choukroune, P., Berástegui, X., Matheron, P., Bareyt, M., Séguret, M., Cámara, P., & Déramond, J. (1989). ECORS deep seismic data and balanced cross sections: geometric constraints on the evolution of the Pyrenees. *Tectonics*, *8*(1), 41–50.

Stipp, M., Stünitz, H., Heilbronner, R., & Schmid, S. M. (2002a). Dynamic recrystallization of quartz: correlation between natural and experimental conditions. In S. De Meer, M. R. Drury, J. H. P. De Bresser, & G. M. Pennock (Eds.), *Deformation Mechanisms, Rheology and Tectonics: Current Status and Future Perspectives* (Vol. 200, pp. 171–190). The Geological Society.

Stipp, M., Stünitz, H., Heilbronner, R., & Schmid, S. M. (2002b). The eastern Tonale fault zone: a "natural laboratory" for crystal plastic deformation of quartz over a temperature range from 250 to 700 °C. *Journal of Structural Geology*, *24*, 1861–1884.

Symmes, G. H., & Ferry, J. M. (1992). The effect of whole-rock MnO content on the stability of garnet in pelitic schists during metamorphism. *Journal of Metamorphic Geology*, *10*, 221–237.

Tikoff, B., Chatzaras, V., Newman, J., & Roberts, N. M. (2019). Big data in microstructure analysis: Building a universal orientation system for thin sections. *Journal of Structural Geology*, *125*(December 2017), 226–234.

Van Melick, J. H. (2021). *Metamorphic conditions of the Cap de Creus shear zones (NE Spain) - Insights from an integrated petrological, electron microscopy and numerical approach* [Unpublished thesis]. Utrecht University.

Vergés, J., Fernàndez, M., & Martínez, A. (2002). The Pyrenean orogen: pre-, syn-, and post-collisional evolution. *Journal of the Virtual Explorer*, *8*, 55–74.

Vergés, J., Millán, H., Roca, E., Muñoz, J. A., Marzo, M., Cirés, J., Den Bezemer, T., Zoetemeijer, R., & Cloetingh, S. (1995). Eastern Pyrenees and related foreland basins: pre-, syn- and post-collisional crustal-scale cross-sections. *Marine and Petroleum Geology*, *12*(8), 893–915.

Vielzeuf, D., Clemens, J. D., Pin, C., & Moinet, E. (1990). Granite, granulites, and crustal differentiation. *Granulites and Crustal Evolution*, 59–85.

Vissers, R. L. M., Van Hinsbergen, D. J. J., Ganerød, M., & Wilkinson, C. M. (2018). Reply to discussion on "Middle Jurassic shear zones at Cap de Creus (eastern Pyrenees, Spain): a record of pre-drift extension of the Piemonte–Ligurian Ocean?" Journal of the Geological Society, London, 174, 289–300. *Journal of the Geological Society*, *175*, 189–191.

Vissers, R. L. M., Van Hinsbergen, D. J. J., Wilkinson, C. M., & Ganerød, M. (2017). Middle Jurassic shear zones at Cap de Creus (eastern Pyrenees, Spain): A record of pre-drift extension of the Piemonte–Ligurian Ocean? *Journal of the Geological Society*, *174*(2), 289–300.

White, R. W., Powell, R., & Holland, T. J. B. (2001). Calculation of partial melting equilibria in the system Na_2O–CaO–K_2O–FeO–MgO–Al_2O_3–SiO_2–H_2O (NCKFMASH). *Journal of Metamorphic Geology*, *19*(2), 139–153.

White, R. W., Powell, R., Holland, T. J. B., Johnson, T. E., & Green, E. C. R. (2014a). New mineral activity-composition relations for thermodynamic calculations in metapelitic systems. *Journal of Metamorphic Geology*, *32*(3), 261–286.

White, R. W., Powell, R., Holland, T. J. B., & Worley, B. A. (2000). The effect of TiO_2 and Fe_2O_3 on metapelitic assemblages at greenschist and amphibolite facies conditions: Mineral equilibria calculations in the system K_2O-FeO-MgO-Al_2O_3-SiO_2-H_2O-TiO_2-Fe_2O_3. *Journal of Metamorphic Geology*, *18*(5), 497–511.

White, R. W., Powell, R., & Johnson, T. E. (2014b). The effect of Mn on mineral stability in metapelites revisited: new a-x relations for manganese-bearing minerals. *Journal of Metamorphic Geology*, *32*(8), 809–828.

Whitney, D. L., & Evans, B. W. (2010). Abbreviations for names of rock-forming minerals. *American Mineralogist*, *95*(1), 185–187.

Zwart, H. J. (1979). The geology of the Central Pyrenees. *Leidse Geologische Mededelingen*, *50*(1), 1–74.

Zwart, H. J. (1986). The Variscan geology of the Pyrenees. *Tectonophysics*, *129*(1–4), 9–27.